Part I: Structure of Central and Southern Mexico from Velocity and Attenuation Tomography; Part II: Physics of Small Repeating Earthquakes

Thesis by

Ting Chen

In Partial Fulfillment of the Requirements

for the Degree of

Doctor of Philosophy

California Institute of Technology

Pasadena, California

2012

(Defended February 23, 2012)

To my parents.

Acknowledgements

First and foremost, I would like to sincerely thank my advisors, Rob Clayton and Nadia Lapusta, for their continuous support and guidance throughout my graduate studies. Rob taught me how to approach the research from the most practical and efficient way. I deeply appreciate his patience, encouragement, and accessibility whenever I needed his help. Nadia is always willing to spend hours discussing my research. I enjoy her excellent way of explaining complicated physics. I am grateful for her inspiration and countless advice. I am so fortunate to have Rob and Nadia as my advisors, and I will always cherish what I have learned from them.

I would like to thank my academic advisor, Joann Stock, for the help with various academic issues. I am very grateful to my other thesis committee members, Pablo Ampuero and Jean-Philippe Avouac, for following my progress, reviewing this thesis, and providing valuable suggestions. I would also like to thank other faculty members at Caltech from whom I have taken classes. Special thanks go to visiting professors Albert Tarantola and Malcolm Sambridge for their great lectures on inverse theory. I also want to thank Jason and Zorka Saleeby for leading the wonderful Hawaii Pahoehoe field trip.

I own my gratitude to all the members in Rob's and Nadia's research groups. Yi Liu and Yoshi Kaneko helped me through the initial stages of my research on earthquake simulations with their experience and knowledge. I benefited greatly from discussions with YoungHee Kim and Hiro Noda.

I would like to acknowledge my colleagues, Kate Chen, Roland Bürgmann, and Robert Nadeau. It was a great collaboration experience, and I learned a lot from each of them.

I appreciate valuable discussions with Brandon Schmandt, Andreas Rietbrock, Xyoli Perez-Campos, Egill Hauksson, Hiroo Kanamori, Bill Ellsworth, Eugene Humphreys, and Donna Eberhart-Phillips.

Many thanks go to my past and current officemates for the help in every way. I am also grateful to other students and postdocs in the Seismo Lab.

My time at Caltech was made enjoyable by my friends. I thank Daoyuan Sun, Zhimei Yan, Min Chen, and Huiyu Li for the warm welcome and tremendous help when I first came to Caltech. I thank Xiangyan Tian, YoungHee Kim, Debby Smith, Lijun Liu, and Yihe Huang for the accompany. I thank Adrienne Roeder for being a great mentor.

I am thankful to Viola Carter, Dian Buchness, Rosemary Miller, Maria Koeper, and Donna Mireles for all the help they provided. I would also like to thank the great IT support in the GPS Division, especially Mike Black, Naveed Near-Ansari, and Scott Dungan.

Finally, I am forever grateful to my parents. Their unconditional love and unyielding support carried me through this whole journey. I thank my cousin, Feng Liang. She has been my role model and a source of help all the time. My deepest appreciation goes to my husband, Fan Guo, for his constant support, incredible patience, and understanding. Fan has become my best friend over the years, and I thank him for making my life colorful.

Abstract

Part I

The 3D V_p, $V_\mathrm{p}/V_\mathrm{s}$, P- and S-wave attenuation structure of the Cocos subduction zone in Mexico is imaged using earthquakes recorded by two temporary seismic arrays and local stations. Direct P-wave arrivals on vertical components and direct S-wave arrivals on transverse components from local earthquakes are used for velocity imaging. Relative delay times for P and PKP phases from teleseismic events are also used to obtain a deeper velocity structure beneath the southern seismic array. Using a spectral-decay method, we calculate a path attenuation operator t^* for each P and S waveform from local events, and then invert for 3D spatial variations in attenuation (Q_p^{-1} and Q_s^{-1}). Inversion results reveal low-attenuation and high-velocity Cocos slab. The slab dip angle increases from almost flat in central Mexico near Mexico City to about 30° in southern Mexico near the Isthmus of Tehuantepec. High attenuation and low velocity in the crust beneath the Trans-Mexico Volcanic Belt correlate with low resistivity, and are probably related to dehydration and melting process. The most pronounced high-attenuation, low-V_p and high-$V_\mathrm{p}/V_\mathrm{s}$ anomaly is found in the crust beneath the Veracruz Basin. A high-velocity structure dipping southward from the Gulf of Mexico near the Isthmus of Tehuantepec coincides with a discontinuity from a receiver functions study, and provides an evidence for the collision between the Yucatán Block and Mexico in the Miocene.

Part II

Small repeating earthquakes present a rare predictable opportunity for detailed field observations because of their short recurrence times and known locations. An intriguing observation about repeating earthquakes is their scaling of recurrence time with seismic moment that is significantly different from the scaling based on a simple conceptual model of circular ruptures with stress drop independent of seismic moment and no aseismic slip. Here we show that a model of repeating earthquakes based on laboratory-derived rate and state friction laws reproduces the observed scaling. In the model, a small fault patch governed by steady-state velocity-weakening friction is surrounded by a much larger velocity-strengthening region. Long-term slip behavior of the fault is simulated using a methodology that fully accounts for both aseismic slip and inertial effects of occasional seismic events. For a fixed set of friction parameters, the observed scaling is reproduced by varying the size of the velocity-weakening patch. We further investigate the behavior of small repeating earthquakes in related models under different scenarios, including several forms of the state evolution equations in rate- and state-dependent friction laws, rectangular velocity-weakening patch geometries, quasi-dynamic vs. fully dynamic representation of inertial effects, and 2D vs. 3D simulations. We find that the simulated scalings between the recurrence time and seismic moment for these different scenarios are similar while differences do exist. We propose a theoretical model for the scaling between the recurrence time and seismic moment of small repeating earthquakes. For patch radii smaller than or comparable to the full nucleation size, the scaling is explained by the increase of seismic to aseismic slip ratio with magnitude. For patch radii larger than the full nucleation size, the scaling is explained by the model in which the recurrence time is determined by the earthquake nucleation time, which is in turn determined by the time for aseismic slip to penetrate the distance of the full nucleation size into the patch. The obtained theoretical insight is used to find the combinations of fault properties that allow the model to fit the observed scaling and range of the seismic moment and recurrence time.

Contents

List of Figures

List of Tables

Chapter 1

Introduction

This thesis focuses on two subjects. The first one is the structure of the Mexican subduction zone, presented in chapters 2 and 3. The second one is the physics of small repeating earthquakes, presented in chapters 4 and 5. Both studies are motivated by my interest in understanding the dynamic behavior of the Earth.

1.1 Structure of Central and Southern Mexico from Velocity and Attenuation Tomography

Detailed information on the structure of the subduction zone is crucial to understanding plate tectonics, continental evolution, and melt generation. Seismic imaging studies in different subduction zones have greatly enhanced our knowledge of the subduction factory (e.g., *Stachnik et al.*, 2004; *Eberhart-Phillips et al.*, 2005; *Schurr et al.*, 2006; *Matsubara et al.*, 2008; *Rychert et al.*, 2008; *Syracuse et al.*, 2008). Both velocity and attenuation have been shown to be useful in characterizing different structures. Because velocity and attenuation have different sensitivity to density, temperature, water, and partial melt content

(*Lawrence and Wysession*, 2006, and references therein), these two images complement each other in identifying the origin of the anomaly. It is also useful to obtain the images using both P and S waves, because, for example, $V_\mathrm{p}/V_\mathrm{s}$ is a good indicator of overpressured fluids.

In Mexico, the Cocos slab subducts beneath the North American plate along the Middle American Trench (figure 1.1). The seismicity indicates that the slab geometry varies greatly along the trench (*Pardo and Suárez*, 1995). It is steep in the north, flat in the central segment, and then back to steep in the south, despite the monotonic change of plate age and subduction rate. In the northern and central segments, the Trans-Mexican Volcanic Belt (TMVB) is not parallel to the trench. In the southern segment, the continuous volcanic arc is missing, and instead, the isolated Los Tuxtlas Volcanic Field (LTVF) is found near the Gulf of Mexico coast. Understanding what causes the anomalous features in Mexico requires better images of the structure.

Two seismic experiments were recently carried out in Mexico (figure 1.1). One is the Middle American Subduction Experiment (MASE), which consists of 100 broadband seismic stations deployed from the Pacific coast to near the Gulf of Mexico in central Mexico. The MASE stations operated from 2005 to 2007. The other seismic experiment was deployed in southern Mexico crossing the states of Veracruz and Oaxaca (VEOX), and consists of 47 broadband seismic stations. The VEOX stations operated from 2007 to 2009. These two seismic arrays provide excellent data for a detailed study of the tectonic structure in this region.

In chapter 2, we use local earthquakes recorded by the MASE stations to obtain a

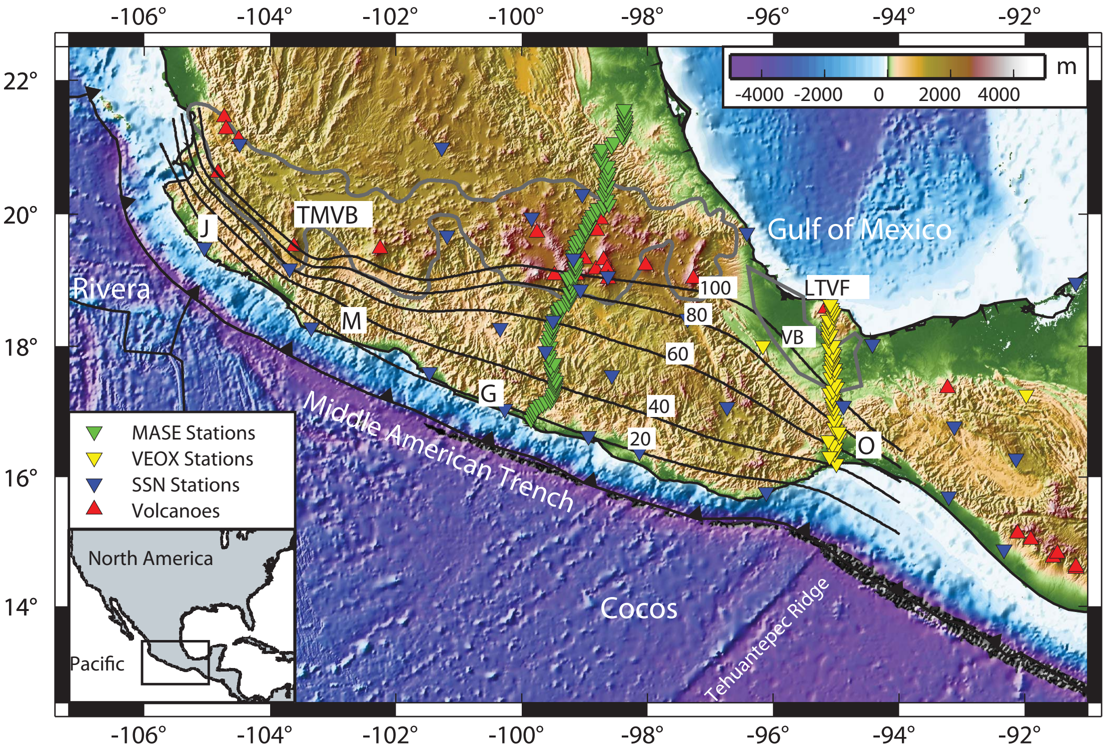

Figure 1.1. Map of the study region. Stations are marked by inverted triangles, and volcanoes are marked by red upright triangles. The Trans-Mexican Volcanic Belt (TMVB) and Veracruz Basin (VB) are outlined in light gray. LTVF denotes the Los Tuxtlas Volcanic Field. J (Jalisco), M (Michoacán), G (Guerrero), and O (Oaxaca) indicate four segments in this region. Slab iso-depth contours from *Pardo and Suárez* (1995) are shown by black lines.

2D P-wave attenuation structure. Using a spectral-decay method, we get a frequency-independent attenuation operator t^* value for each seismogram, and then invert for spatial variations in P-wave quality factor Q_p in the cross section perpendicular to the trench. The inversion results show low attenuation in the subducting slab, and relatively high attenuation in the mantle wedge and the crust below the TMVB. The high-attenuation region in the crust correlates with the low-resistivity zone from an MT study (*Jödicke et al.*, 2006) (figure 1.2c), and could be caused by fluids and partial melts from dehydration and magmatic processes.

The P-wave attenuation structure obtained in chapter 2, together with receiver functions (*Pérez-Campos et al.*, 2008; *Kim et al.*, 2010), teleseismic velocity (*Husker and Davis*, 2009) (figure 1.3) and surface wave studies (*Iglesias et al.*, 2010) along the same line provide a detailed 2D image of the subduction system from the coast to the back arc.

In chapter 3, we extend the study to a 3D image by incorporating data from the MASE, VEOX and some local permanent stations. The 3D V_p, $V_\mathrm{p}/V_\mathrm{s}$, P- and S-wave attenuation structure has been obtained. Direct P-wave arrivals on vertical components and direct S-wave arrivals on transverse components from local earthquakes are used for 3D V_p and $V_\mathrm{p}/V_\mathrm{s}$ imaging. Path attenuation operators t^* for P and S waveforms from local events are inverted for variations in attenuation (Q_p^{-1} and Q_s^{-1}). We also use relative delay times for P and PKP phases from teleseismic events to get deeper velocity structure. Since local permanent stations are sparse, and a teleseismic velocity study has already been done along the MASE array (*Husker and Davis*, 2009) (figure 1.3), we only obtain a 2D teleseismic P-wave velocity image beneath the VEOX array in this study.

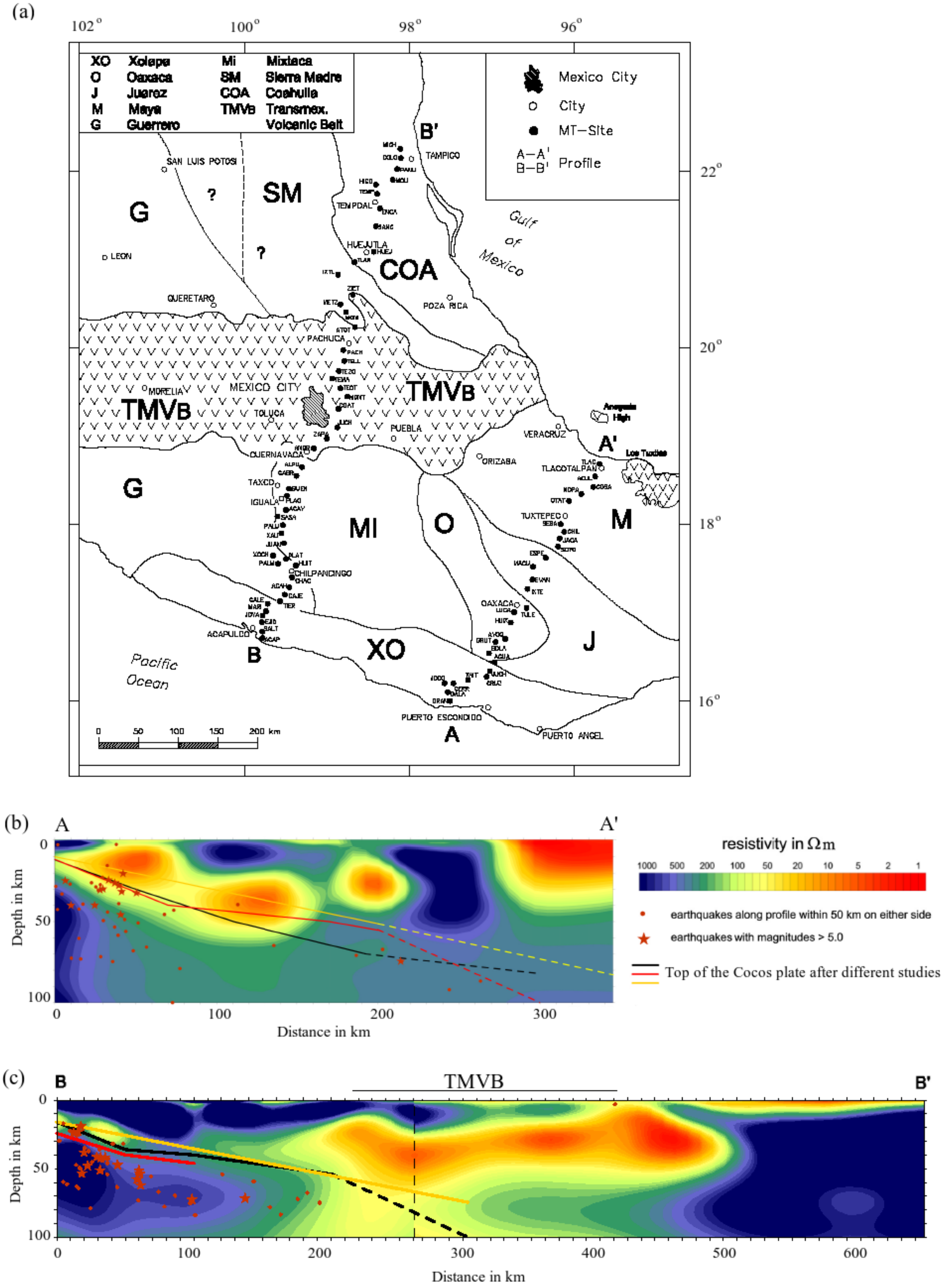

Figure 1.2. The MT study results from *Jödicke et al.* (2006). (a) Map of the MT survey lines. (b) The MT results along the line AA′. (c) The MT results along the line BB′.

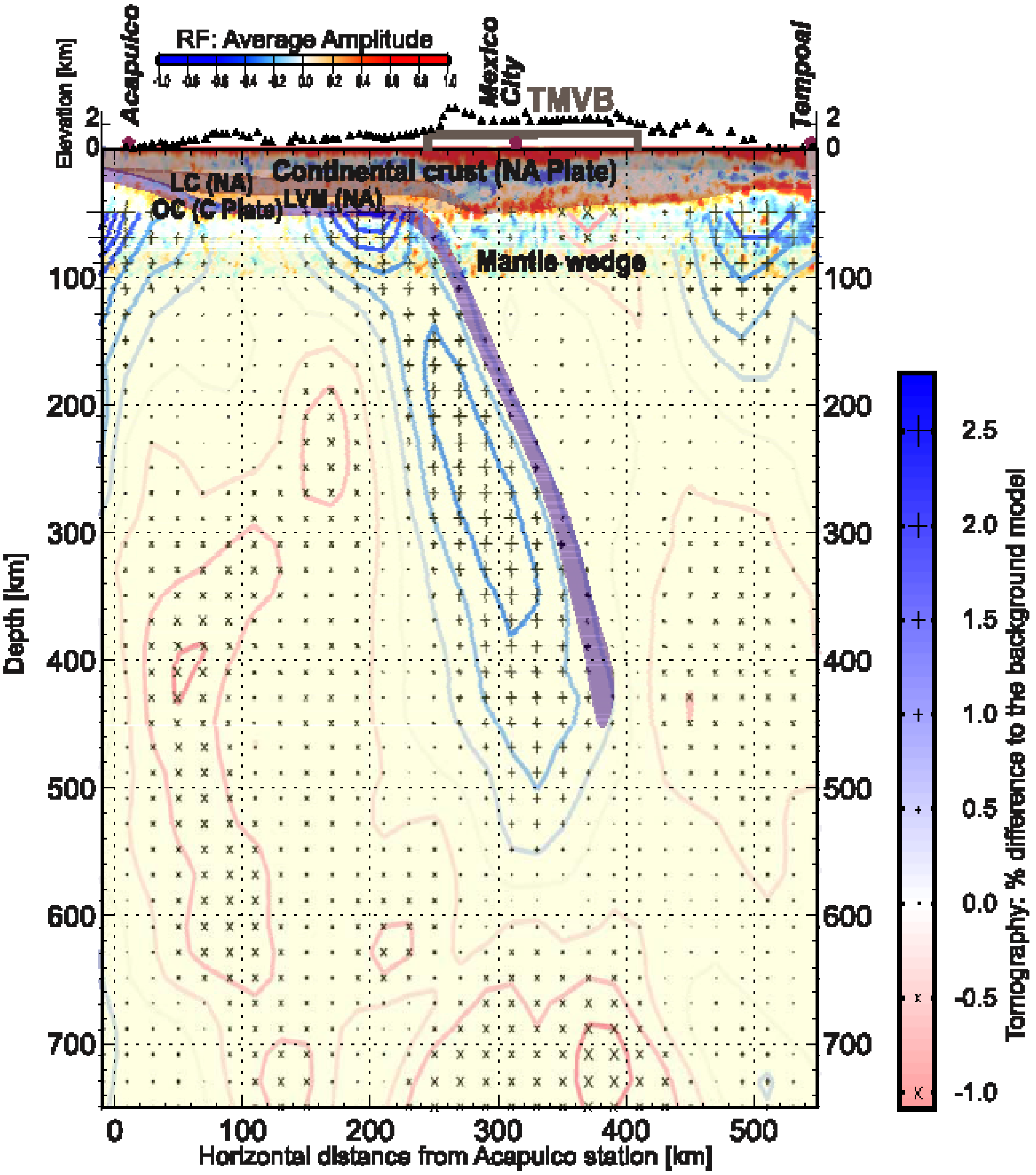

Figure 1.3. Receiver functions results and teleseismic P-wave velocity along the MASE line from *Pérez-Campos et al.* (2008). NA: North America; C: Cocos; LC: lower crust; LVM: low velocity mantle; OC: oceanic crust.

The Cocos slab is clearly shown in our image as low attenuation and high velocity. The slab is almost flat in central Mexico, and has a dip angle of about 30° in southern Mexico. High attenuation and low velocity are found in the crust beneath the TMVB. The most pronounced high-attenuation, low-V_p and high-$V_\mathrm{p}/V_\mathrm{s}$ anomaly lies in the crust beneath the Veracruz Basin. An unexpected high-velocity structure is found dipping southward into the mantle from the Gulf of Mexico, and truncates the Cocos slab at about 150 km near the Isthmus of Tehuantepec. This high-velocity structure coincides with a discontinuity from a receiver functions study (*Kim et al.*, 2011), and may be related to the oceanic plate subducted before the collision between the Yucatán Block and Mexico in the Miocene (*Kim et al.*, 2011). The unusual geometry of the slab likely changes the convective flow in the mantle wedge, and affects the volcanism in this region.

1.2 Physics of Small Repeating Earthquakes

Repeating earthquakes are seismic events that repeatedly occur in the same location with similar seismic signals. Small repeating earthquakes have been found on a number of faults (*Ellsworth and Dietz*, 1990; *Vidale et al.*, 1994; *Nadeau and Johnson*, 1998; *Bürgmann et al.*, 2000; *Igarashi et al.*, 2003; *Peng and Ben-Zion*, 2005; *Chen et al.*, 2007). Since their recurrence times are short and their locations are known, small repeating earthquakes present a rare opportunity for detailed field observations. They are used to study fault creeping velocities, earthquake nucleation, postseismic slip, stress drops, and other aspects of tectonophysics, earthquake mechanics, and seismology (e.g., *Ellsworth and Dietz*, 1990; *Vidale et al.*, 1994; *Marone et al.*, 1995; *Nadeau and Johnson*, 1998; *Schaff et al.*, 1998;

Nadeau and McEvilly, 1999; *Bürgmann et al.*, 2000; *Igarashi et al.*, 2003; *Nadeau et al.*, 2004; *Schaff and Beroza*, 2004; *Matsubara et al.*, 2005; *Peng and Ben-Zion*, 2005; *Allmann and Shearer*, 2007; *Chen et al.*, 2007; *Dreger et al.*, 2007). With abundant seismic data for small repeating earthquakes, it is important to construct a dynamic model that can explain various aspects of related observations.

One of the intriguing observations about small repeating earthquakes is the scaling of their recurrence time T with the seismic moment M_0 as $T \propto M_0^{0.17}$. This scaling was first pointed out by *Nadeau and Johnson* (1998) for repeating earthquakes in Parkfield along the San Andreas Fault (figure 1.4), and then confirmed in other regions (*Chen et al.*, 2007). A simple conceptual model of these events as circular ruptures with stress drop independent of the seismic moment and no aseismic slip, however, results in $T \propto M_0^{1/3}$ (*Nadeau and Johnson*, 1998; *Beeler et al.*, 2001).

In chapter 4, we show that a model of repeating earthquakes based on laboratory-derived rate and state friction laws reproduces the observed scaling. In the model, a small velocity-weakening patch is surrounded by much larger velocity-strengthening region. The aging form of the state evolution equation is used. The whole fault is subject to long-term tectonic loading. Long-term slip behavior of the fault is simulated using a methodology that fully accounts for both aseismic slip and inertial effects of occasional seismic events (*Liu and Lapusta*, 2008). The model results in repeating earthquakes with typical stress drops and sizes comparable with observations. For a fixed set of friction parameters, the observed scaling is reproduced by varying the size of the velocity-weakening patch. In simulations, a significant part of slip on the velocity-weakening patches is accumulated

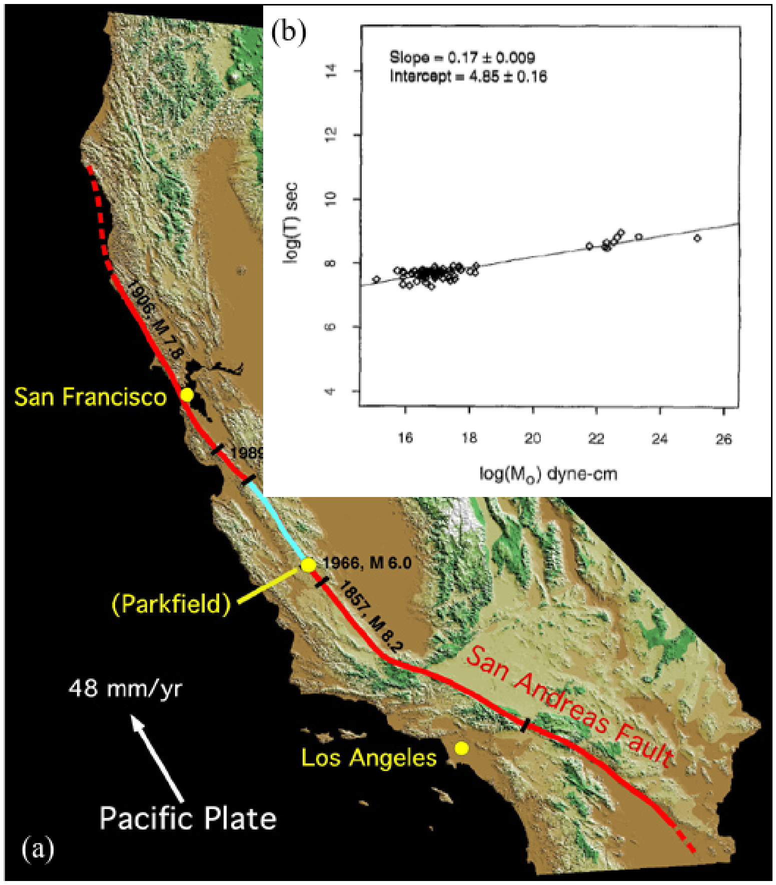

Figure 1.4. (a) Location of Parkfield along the San Andreas Fault. (b) Observations of the scaling between the recurrence time T and seismic moment M_0 for small repeating earthquakes in Parkfield from *Nadeau and Johnson* (1998).

aseismically, even though the patches also produce seismic events. The proposed model supplies a laboratory-based framework for interpreting the wealth of observations about repeating earthquakes, provides indirect evidence that rate and state friction acts on natural faults, and has important implications for possible scenarios of slip partitioning into seismic and aseismic parts.

Why the model in chapter 4 is able to match the observed scaling between the recurrence time and seismic moment, and what elements in the model are most important, merit further study. In chapter 5, we investigate the behavior of small repeating earthquakes in models related to the one used in chapter 4 under different scenarios. The scenarios we studied include several forms of the state evolution equations in rate- and state-dependent friction laws, rectangular velocity-weakening patch geometries, quasi-dynamic vs. fully dynamic representation of inertial effects, and 2D vs. 3D simulations. We find that the simulated scalings between the recurrence time and seismic moment for these different scenarios are similar while differences do exist. We propose a theoretical model for the scaling between the recurrence time and seismic moment of small repeating earthquakes. For patch radii smaller than or comparable to the full nucleation size, aseismic slip creeps all the way into the center of the patch, and the scaling is explained by the increase of seismic to aseismic slip ratio with magnitude. For patch radii larger than the full nucleation size, the scaling is explained by the model in which the recurrence time is determined by the time for aseismic slip to penetrate the distance of the full nucleation size into the patch. The obtained theoretical insight is used to find the combinations of fault properties that allow the model to fit the observed scaling and range of the seismic moment and recurrence time.

Part I: Structure of Central and Southern Mexico from Velocity and Attenuation Tomography

Chapter 2

Two-Dimensional Seismic Attenuation Structure in Central Mexico

This chapter was originally published by Ting Chen and Robert W. Clayton (2009) in *Journal of Geophysical Research, 114*, B07304, doi:10.1029/2008JB005964.

2.1 Introduction

Intrinsic attenuation is energy loss or absorption as seismic waves pass through the rocks. One of the major mechanisms of intrinsic attenuation is the frictional loss in dry rocks due to relative movement at grain boundaries, which is strongly dependent on pressure and temperature (*Jackson et al.*, 1992). Another one is viscous damping when there is fluid present (*Mavko*, 1980). In recent years, detailed images of the attenuation structure have been obtained in different subduction zones such as Tonga-Fiji (*Roth et al.*, 1999), Japan (*Tsumura et al.*, 2000), central Andes (*Schurr et al.*, 2003), Alaska (*Stachnik et al.*, 2004), New Zealand (*Eberhart-Phillips et al.*, 2008), Costa Rica and Nicaragua (*Rychert et al.*, 2008). These studies generally show that the subducting slab is characterized by low attenuation, while high attenuation is found in the mantle wedge and/or the crust beneath the volcanic arc. Detailed attenuation images in the mantle wedge and the crust above, however, vary from place to place. In some places such as Alaska, Costa Rica and Nicaragua (*Stachnik et al.*, 2004; *Rychert et al.*, 2008), the high attenuation is concentrated in zones within the mantle wedge. These obtained attenuation images help to determine the relative viscosity (*Karato*, 2003), and provide constraints on the mantle wedge temperature (*Stachnik et al.*, 2004) and subduction dynamics including slab dehydration and melt transport (*Schurr et al.*, 2003).

The seismic attenuation in the central Mexican subduction zone has been studied by several authors (e.g., *Castro et al.*, 1990; *Ordaz and Singh*, 1992; *Garcia et al.*, 2004; *Singh et al.*, 2006, 2007). However, because seismicity in this region is sparse, especially for intermediate earthquakes, most of these studies are confined to the crust. *Castro et al.* (1990) estimated the average crustal attenuation for shear waves propagating along the Pacific coast. *Ordaz and Singh* (1992) determined the average Q_s in the crust including both coastal and inland paths. *Garcia et al.* (2004) analyzed some intermediate-depth inslab earthquakes, and reported an average Q_s similar to that of *Ordaz and Singh* (1992). *Singh et al.* (2007) studied the Q of Lg waves and found that Q in the central Mexican Volcanic Belt is lower than that in the forearc. Due to the lack of seismic stations in the backarc, the attenuation of the mantle wedge in this region was only recently studied by *Singh et al.* (2006). They analyzed shear waves from 16 earthquakes recorded at a station near the Gulf of Mexico and found that waves passing through the mantle wedge attenuate more than those mostly traveling through the continental lithosphere. They suggested that this difference is due to the low Q of the mantle wedge compared with the continental lithosphere, and estimated an upper bound of $120f^{0.75}$ for shear-wave Q in the mantle wedge.

A detailed image of the attenuation structure in central Mexico requires a much larger data set. The recent Middle American Subduction Experiment (MASE), which was a temporary deployment of 100 broadband stations in central Mexico from 2005 to 2007, provides us such an opportunity to obtain a 2D attenuation structure in this region.

2.2 Tectonic Setting

In the Mexican subduction zone, the Rivera and Cocos Plates are subducting beneath the North American Plate along the Middle American Trench with convergence rate increasing from 3.9 cm/a at 106.5° W to 7.2 cm/a at 94°W (*DeMets et al.*, 1994). The age of the oceanic crust at the trench also increases from about 10 Ma in the west to 23 Ma in the east (*Pardo and Suárez*, 1995). Despite the generally monotonic increase in subduction rate and plate age toward the southeast, the slab dip angle shows unexpected lateral variations. *Pardo and Suárez* (1995) studied the lateral variations in the dip of the subducted oceanic plates by locating hypocenters of earthquakes and found that a shallow subhorizontal slab in central Mexico is bounded by steeper slab geometry in both northern and southern Mexico. Based on the seismicity, focal mechanisms, and slab geometry, the Mexican subduction zone can be divided into four segments (*Pardo and Suárez*, 1995) (figure 2.1): (1) the Jalisco segment, where the Rivera plate subducts at a steep angle ($\sim$$50^\circ$); (2) the Michoacán segment, where the dip angle of the Cocos slab decreases gradually ($\sim$$50^\circ$–$0^\circ$); (3) the Guerrero-Oaxaca segment, where the slab is almost flat for about 250 km ($\sim$$0^\circ$); (4) the southern Oaxaca and Chiapas segment, where the dip angle of the Cocos slab increases gradually ($\sim$$0^\circ$–$30^\circ$). Receiver functions and seismic velocity tomography studies from recent MASE experiment in the Guerrero region imaged the slab in detail in a cross section perpendicular to the Middle American Trench and through Mexico City (*Pérez-Campos et al.*, 2008). The results show that the Cocos slab is horizontal beneath the North American plate for about 250 km, and then plunges into the mantle just before the volcanic belt with a dip angle of about 75°. The slab is truncated at a depth of 500 km (*Husker and Davis*, 2009).

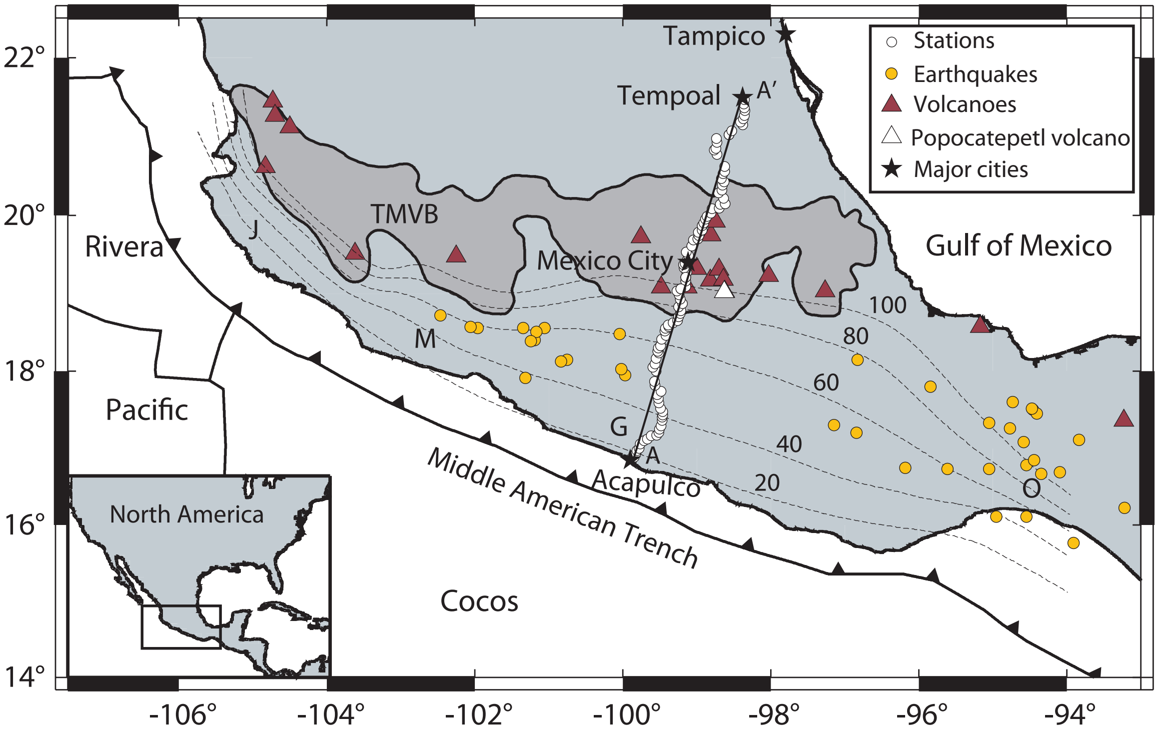

Figure 2.1. The stations and events used in this study. White circles and yellow circles indicate the MASE array and epicenters of events used in this study respectively. Red triangles denote volcanoes, and the white triangle shows Popocatépetl volcano. The dark gray shaded area indicates the Trans-Mexican Volcanic Belt (TMVB). Slab isodepth contours from *Pardo and Suárez* (1995) are shown in dashed lines. J (Jalisco), M (Michoacán), G (Guerrero-Oaxaca) and O (southern Oaxaca) indicate four segments. Major cities along the MASE array are shown as stars for reference. The line AA′ represents the cross section projection for 2D attenuation tomography.

Another interesting tectonic feature in central Mexico is the location of the Trans-Mexican Volcanic Belt (TMVB). Unlike the usual trench-parallel geometry in other subduction zones, the TMVB lies across central Mexico with an angle about 16° oblique to the Middle American Trench. It is about 300 km away from the trench near Mexico City. The TMVB consists of nearly 8000 volcanic structures, and extends about 1000 km long while varying in width between 80 and 230 km (*Gómez-Tuena and Ferrari*, 2007). A variety of volcanic structures have been formed since the middle to late Miocene, including large strato-volcanoes, monogenetic cones, shield volcanoes, calderas, lava flows and domes (*Macías*, 2007). Popocatépetl, one of the largest strato-volcanoes in Mexico, is located just 65 km southeast of Mexico City, and has been active since 1994 after 67 years of quiescence (*Macías*, 2007). Although some alkaline volcanism exists, the dominant volcanic sequences in the TMVB are calc-alkaline, and the volcanic belt is thought to be related to the subduction of the Rivera and Cocos plates (*Pardo and Suárez*, 1995).

2.3 Data

The MASE survey line is perpendicular to the Middle American Trench, and runs across Mexico from Acapulco on the Pacific coast, through Mexico City, and to Tempoal near the Gulf of Mexico (figure 2.1). It was in place from 2005 to 2007. The array consisted of 100 three-component broadband sensors (Guralp CMG-3T) spaced approximately 5 km apart. The data were recorded continuously at 100 samples per second.

In this study, we analyzed seismograms from 37 regional earthquakes recorded by the MASE array. These events are within the magnitude range of 4.5 to 6.1, and the depths vary from 50 to 184 km (figure 2.1). The locations of the events are determined by the Servicio Sismológico Nacional (SSN) of Mexico, which consists of 36 broadband stations and about 10 short-period stations through Mexico. The SEISAN program (*Haskov and Ottemöller*, 1999) is used by the SSN for location determination.

2.4 Estimation of Path Attenuation

The attenuation of seismic waves can be estimated from the amplitude spectra. The Fourier velocity spectral amplitude of a body wave from event j, recorded at a hard rock site station i, can be written as (e.g., *Anderson and Hough*, 1984)

$$A_{ij}(f) = CS_j(f)I_i(f)\text{exp}(-\pi f t^*_{ij}), \tag{2.1}$$

where $S(f)$ is the source spectrum, $I(f)$ is the instrument response, and C is the frequency-independent amplitude term associated with geometric spreading, radiation pattern, and other static effects. The exponential term describes the attenuation effect. The whole path attenuation operator t^* can be expressed as $t^* = \tau/Q$, with τ being the total travel time and Q being the average quality factor along the ray path.

Assuming a Brune-type source (*Brune*, 1970), the source velocity spectrum of event j can be written as

$$S_j(f) = \frac{fM_{0j}}{1 + (f/f_c)^2}, \tag{2.2}$$

where M_{0j} is the seismic moment, and f_c is the corner frequency. Since only data in the flat portion of the pass band (0.01–30 Hz) of the recording system were used in this study,

$I(f)$ in equation (2.1) can be neglected, leading to

$$A_{ij}(f) = \frac{C'f}{1+(f/f_c)^2}\exp(-\pi f t^*_{ij}), \tag{2.3}$$

where C' is a combination of C from equation (2.1) and frequency-independent terms from $S(f)$ and $I(f)$.

The iterative approach of *Eberhart-Phillips and Chadwick* (2002) was applied to determine frequency-independent t^*_{ij} for each ray path, together with C' for each ray and a common corner frequency f_c for each event. The corner frequency f_c is determined using a grid search over the frequency range 1–20 Hz using all available velocity spectra for each event. Then for each spectrum, up to 10 iterations of the loop in which C' and t^*_{ij} are updated sequentially, are carried out starting with an initial estimate of t^*_{ij}. In the analysis of P waves, we used the high-sample-rate vertical-component waveforms. The velocity amplitude spectra were calculated from a 2.56 s time window beginning at the P wave using a multitaper algorithm (*Park et al.*, 1987). Corresponding noise spectra were also calculated from a 2.56 s time window before the P wave. To ensure a high quality estimate of t^*, we only used the data with a signal-to-noise ratio greater than 2 in a frequency bandwidth wider than 5 Hz. The lower limit of the frequency band is 1 Hz, and the upper limit varies from 6 to 30 Hz depending on the noise. Examples of waveforms and fits to the spectra are shown in figure 2.2.

Based on spectral analysis, we found that the waves passing through the arc and backarc have different attenuation features than the waves passing through the forearc. Figure 2.3 shows an example of this attenuation contrast for two paths. Path A and path B are from the

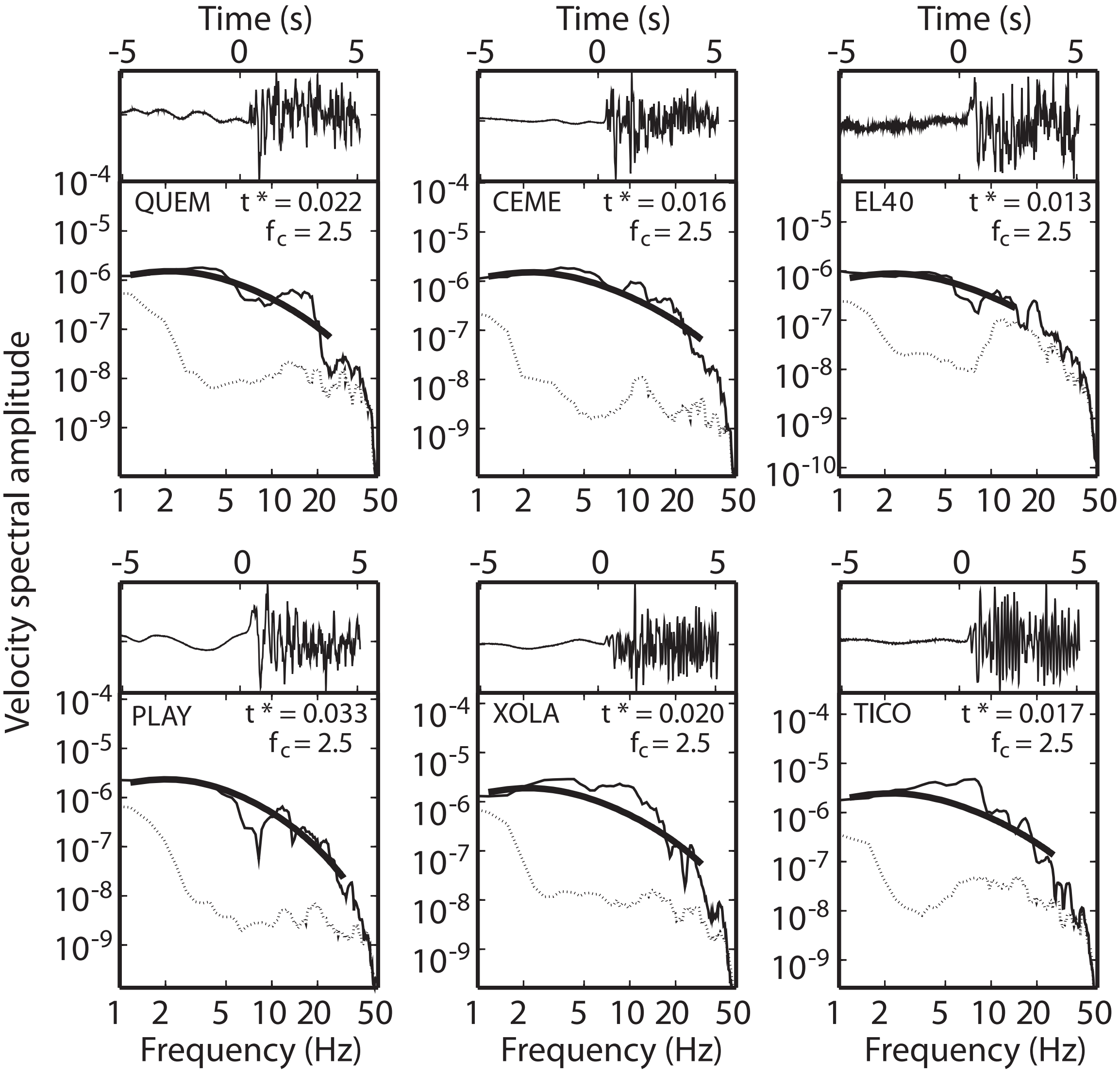

Figure 2.2. Examples of waveforms and fits to the spectra of one earthquake (lat = $17.1°$, lon = $-93.8°$, depth = 184 km, 06/22/2005). For each station, the velocity spectra are shown below the velocity waveform. The plotted velocity waveform is normalized by its peak amplitude. Signal and noise spectra are calculated from 2.56 s windows after and before P arrivals, and are shown as solid and dotted lines respectively. Heavy lines indicate the fits to the signal spectra over the frequency range with signal-to-noise ratio greater than 2. The station name and estimated values of t^*, f_c are shown for each station.

same event, and are chosen to have the same path length to eliminate the spectral difference due to geometric spreading. Path A goes through the forearc, while path B goes through the arc and backarc. We calculated the spectra of the P waves traveling along the two paths and found that the spectrum of the wave going along path B decays more rapidly with frequency than that of the wave going along path A, which indicates higher attenuation along path B than path A. The overall lower absolute spectral amplitude of wave B than that of wave A is partly due to the higher average attenuation along path B, and partly due to other effects such as source radiation pattern, scattering and local site effects. In figure 2.4, we show the attenuation variation of waves from the same event and received at stations along the MASE array by plotting the value of the path-averaged attenuation parameter $1000t^*/\tau$ for each ray, where τ is the travel time. It is clear that the waves passing through the arc and backarc systematically attenuate more than the waves passing through the forearc. This behavior exists for almost every event that is well recorded along the whole array and indicates that the arc and backarc are characterized by high attenuation. To determine the exact locations of the attenuating regions, we applied a tomographic inversion.

2.5 Tomographic Inversion

2.5.1 Method

We invert the t^* measurements for 2D variations in $1/Q$. The study region is divided into blocks and each block is assumed to have constant $1/Q$. The observed t^* for the ith ray

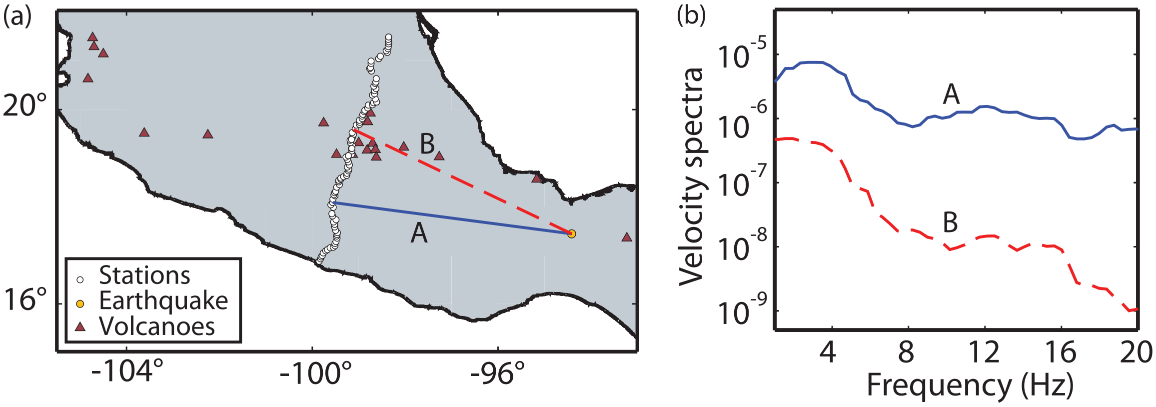

Figure 2.3. Example of attenuation contrast for two waves from the same event (lat = $17.5°$, lon = $-94.4°$, depth = 179 km, 05/08/2006), and recorded at the stations along the MASE array. (a) Path A and path B have about the same length. Path A goes through the forearc, and path B goes through the arc and backarc. (b) The velocity spectra of P waves along path A and path B. The spectral amplitude of the wave along path B decays more rapidly with frequency than that of the wave along path A, indicating that the average attenuation along path B is higher than that of path A.

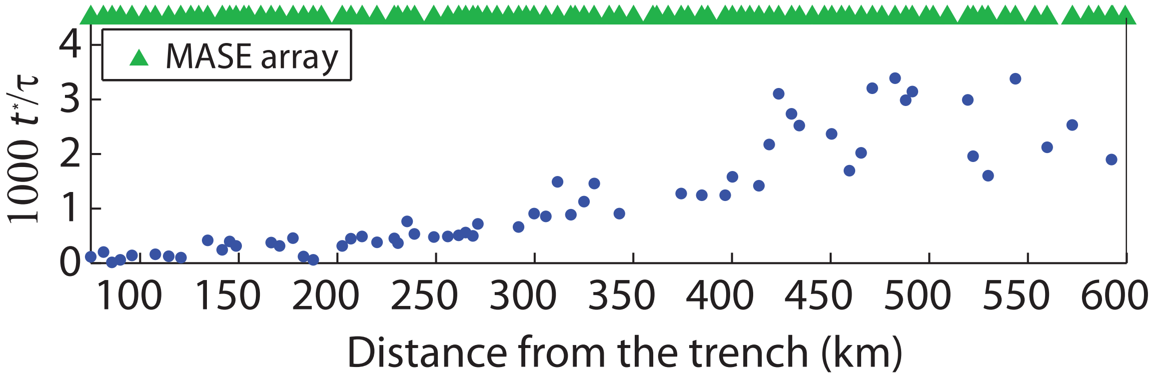

Figure 2.4. Path-averaged attenuation for rays from one event to each station along the MASE array. The event shown here is the same as that in figure 2.3. The Path-averaged attenuation parameter $1000t^*/\tau$ is plotted versus the position of each station where the wave is recorded.

path is

$$t_i^* = \sum_j \tau_{ij}(Q^{-1})_j, \tag{2.4}$$

where t_{ij} is the travel time in block j for the ith path, Q_j is the quality factor for block j. Since τ_{ij} can be considered to be independent of $(Q^{-1})_j$, there exists a linear relationship between t_i^* and $(Q^{-1})_j$. The inversion problem can be written in matrix form as

$$[\tau]_{NM}[Q^{-1}]_M = [t^*]_N, \tag{2.5}$$

where M is the number of blocks and N is the number of t^* measurements. In this study, a total of 1588 measurements of t^* were used.

We assume the attenuation structure has no variation along the strike of the Middle American Trench, and invert for 2D attenuation structure in the cross section perpendicular to the trench, and along the MASE array (shown as line AA′ in figure 2.1). Based on the ray coverage, we first divided the cross section into blocks with 50 km horizontal spacing and 20 km vertical spacing. We then modified some blocks with hit counts less than 8 by combining them with their neighboring blocks to make larger 100 km $\times$ 20 km blocks, thus increasing the robustness at the edge. Different model parameterizations were tested, and show overall similar feature of the inversion results. To compute t_{ij}, we traced rays in IASP91 velocity model (*Kennett and Engdahl*, 1991) with Moho at 40 km depth, as indicated by receiver functions (*Pérez-Campos et al.*, 2008) (figure 2.5).

A damped least squares method that minimizes a combination of data misfit and model

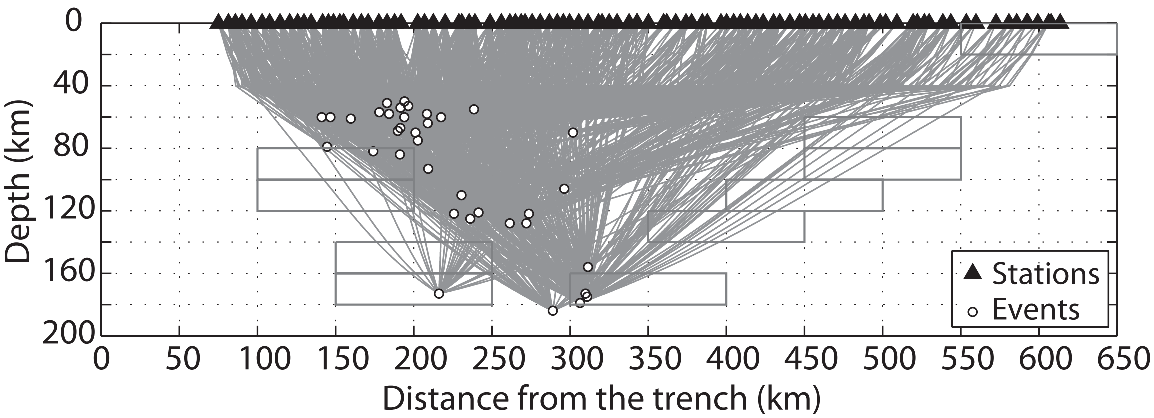

Figure 2.5. Raypaths and grid used for tomographic inversion. This cross section is perpendicular to the trench, and along the MASE array as indicated by line AA′ in figure 2.1. Stations are shown as triangles. Events (white circles) are projected onto this cross section. Rays are traced in IASP91 velocity model with Moho at 40 km depth (*Pérez-Campos et al.*, 2008). Block sizes are mostly 50 km × 20 km, with larger blocks (100 km × 20 km) at the edges to increase the robustness. The larger blocks are highlighted by solid lines.

norm was used to solve this problem:

$$[Q^{-1}]_M = ([\tau]^T_{MN}[\tau]_{NM} + \mu I)^{-1}[\tau]^T_{MN}[t^*]_N. \tag{2.6}$$

The damping factor $\mu = 5$ was selected based on the L-curve criterion (*Aster et al.*, 2005).

2.5.2 Inversion Results

A high-attenuation result in the mantle wedge (figure 2.6) is consistent with the study of *Singh et al.* (2006). The high attenuation, however, does not prevail in the whole mantle wedge, but is localized in a zone about 80 to 120 km beneath the TMVB, and about 400 to 500 km from the trench. It is about 50 km away from the top of the slab . The high-attenuation zone in the mantle wedge has Q_p less than 200, with the lowest Q_p value being 130. Because the Q determined in this study is for P waves, and is frequency independent, it

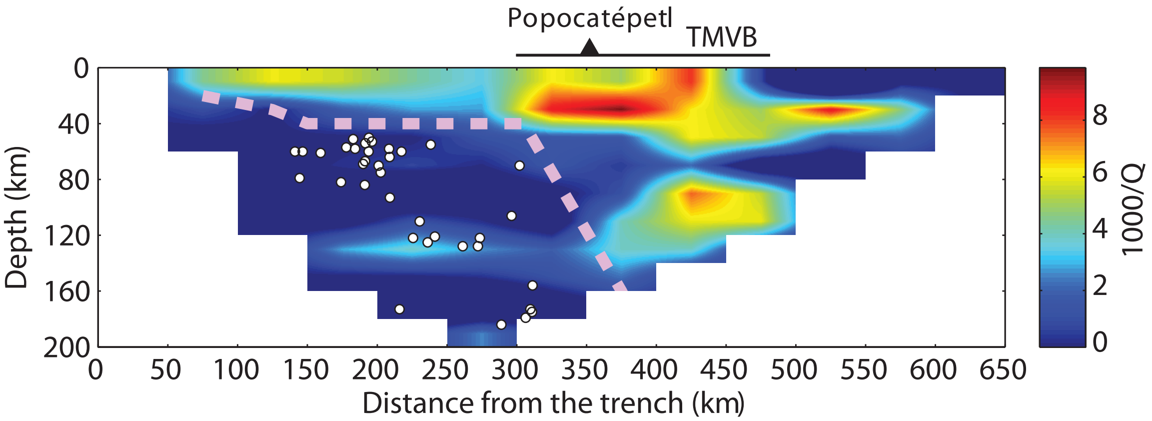

Figure 2.6. Results for 2D tomographic inversion in $1000/Q$. The TMVB is shown on top as a line for reference, together with Popocatépetl volcano (triangle). Dashed line indicates the top of the slab along the MASE array, based on receiver functions and velocity tomography studies (*Pérez-Campos et al.*, 2008). Earthquakes used in the local 2D inversion are shown as white dots.

can not be compared with the upper bound of the frequency-dependent shear-wave Q in the mantle wedge estimated by *Singh et al.* (2006) in a straightforward way. However, taking $Q_p/Q_s = 1.5$–2.25, and assuming that frequency-independent Q measurements mostly reflect Q at the upper end of the frequency band (*Roth et al.*, 1999; *Stachnik et al.*, 2004), the Q for the high-attenuation zone in the mantle wedge from our study is significantly lower than the estimate of the upper bound of the attenuation $Q_s = 120f^{0.75}$ ($0.1 \leq f \leq 10$ Hz) by *Singh et al.* (2006). Their value is similar to what we find for the corner of the mantle wedge.

Another P-wave high-attenuation zone is imaged in the crust beneath and to the north of the TMVB, which is consistent with studies of Lg-wave attenuation in the same area (*Singh et al.*, 2007). The high attenuation mostly concentrates in the lower crust, about 300 to 600 km from the trench. Two prominent subzones with $Q_p \sim 120$ exist in the high-attenuation region in the lower crust. One is beneath the TMVB close to the trench, and the other is to the north of the TMVB. The volcano Popocatépetl lies roughly on the maximum ($Q_p \sim 110$) of the high-attenuation zone. High attenuation is also found to be diffused in the upper crust in the forearc and arc, especially at a location about 400 km to 450 km from the trench. Low attenuation ($Q_p > 1000$) is imaged in a broad area from the coast to the front of the TMVB, and deeper than 40 km.

2.5.3 Resolution

The resolution of the inversion was evaluated by the model resolution matrix. Diagonal elements of the resolution matrix measure how much information is recovered in each block (figure 2.7). Due to the closely-spaced stations, most of the model is well resolved, especially the forearc region deeper than 40 km (resolution $>$ 0.95). The resolution in the crust is a little lower, because of the limited crossing ray paths, and also because rays travel less through the crust blocks compared with mantle blocks since most events are far away from the stations. The edges of the model are relatively less well resolved, due to the low ray coverage. It should be noted that since we used relatively large blocks, and combined blocks with hit counts less than 8 to increase the robustness at the edges, even the least well resolved block has resolution as high as 0.7. This means the whole model is generally well resolved.

We also performed numerical tests to examine the robustness for regions of interest in the inversion. In each test, we trace the ray paths through an input $1000/Q$ model to generate synthetic t^* data, and add some normally distributed noise with a standard deviation of 0.02 to the data. Then we invert these t^* values for $1000/Q$ in the same way

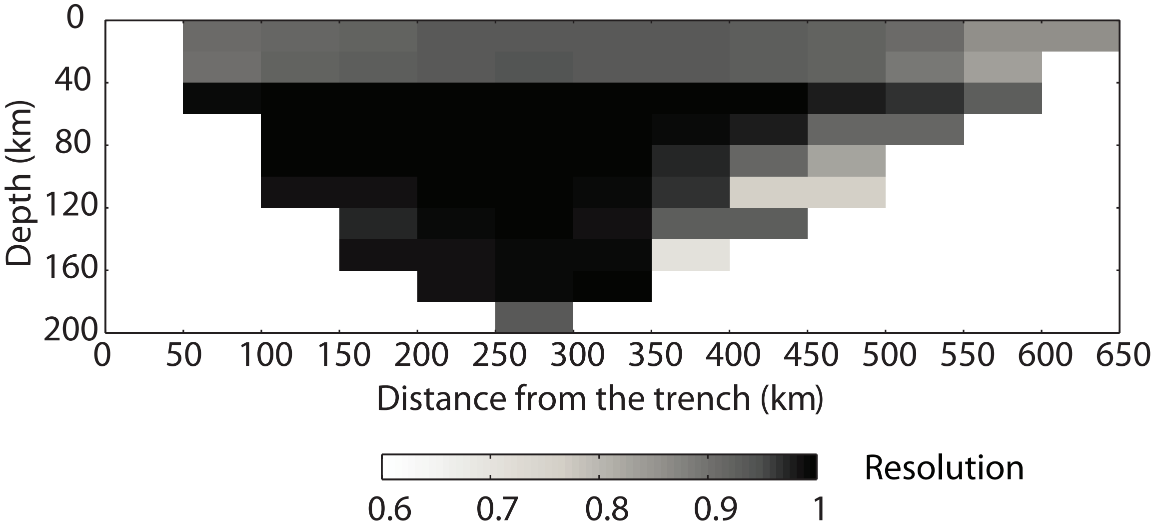

Figure 2.7. Diagonal elements of the model resolution matrix. The resolution is higher than 0.7 for all the blocks with nonzero hit counts.

as we did for real data. In the first test, the input $1000/Q$ model has a high-attenuation anomaly in the lower crust in the arc and backarc (figure 2.8a). The values of $1000/Q$ for the anomaly and background are 10 and 1 respectively, both being comparable to the inversion results. The anomaly is shown to be generally recovered, with some smearing into the upper crust (figure 2.8b). In the second test, the high-attenuation anomaly lies in the mantle wedge between the depths of 80 and 120 km, and 400 to 500 km away from the trench (figure 2.8c). The test shows that the anomaly can be generally recovered, although there is also some smearing into nearby blocks (figure 2.8d).

2.6 Interpretation and Discussion

The high-attenuation region in the mantle wedge roughly corresponds to a low-velocity region known from teleseismic wave studies (*Husker and Davis*, 2009). Several factors including temperature, hydration, and melt can account for both high attenuation and low

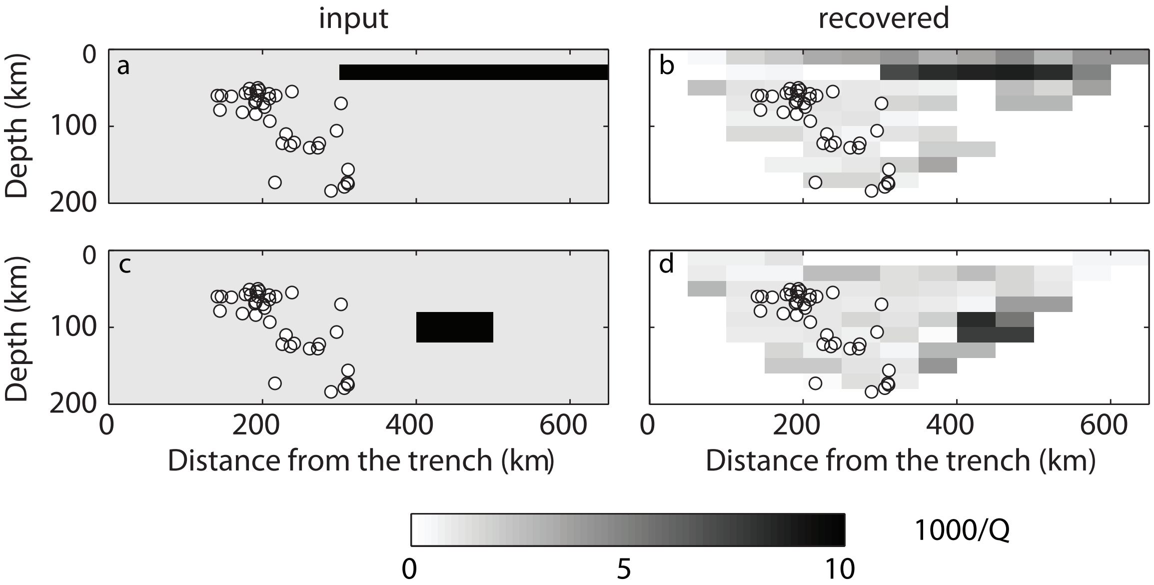

Figure 2.8. Numerical resolution tests. (**left**) Input models with anomalies in part of the lower crust (a) and the mantle wedge (c). (**right**) Models recovered by inverting the synthetic data with noise. The anomalies are generally well recovered. White dots indicate events used in this study.

velocity (*Karato*, 2003, and references therein). Considering the subduction zone setting and the active volcanism above the mantle wedge, high temperature could be a large factor for the imaged high-attenuation zone in the mantle wedge. However, fluids and melts may also play important roles. The small amount of sediment fill in the Middle American Trench suggests that a dominant part of the oceanic sediments are subducted (*Manea et al.*, 2003). Evidence of the existence of fluids and volatiles in the mantle wedge are also found by geochemical studies (*Blatter and Carmichael*, 1998; *Carmichael*, 2002). As oceanic lithosphere subducts into the mantle, it encounters higher temperature and pressure, and when it reaches certain depths, the water from oceanic crust and sediments is released into the overlying mantle wedge, lowering the melting temperature of peridotite (*Peacock*, 2003). The temperature at the top of the slab, however, is usually still not high enough for melting due to the cooling of the slab itself, so the fluids continue to migrate in the mantle wedge. As the temperature rises and finally exceeds the wet solidus of peridotite, partial melts will occur, and they will be away from the top of the slab (*Hebert et al.*, 2009). Our inversion results are consistent with this process, with the focused high-attenuation zone in the mantle wedge probably indicating a region with partial melts. Because our study is for P waves, the imaged high-attenuation zone probably only shows where most partial melts are produced, while the whole partial melt zone could be broader, which is expected to be shown in shear-wave attenuation as in studies in Nicaragua (*Rychert et al.*, 2008). The high-attenuation zone in the mantle wedge lies beneath the northern part of the TMVB instead of the southern part where the volcanoes are currently more active, suggesting more complex melt transport rather than a simple vertical path. Relatively low attenuation in the corner of the mantle wedge has also been observed in other subduction zones such as Alaska, New Zealand, Nicaragua (*Stachnik et al.*, 2004; *Eberhart-Phillips et al.*, 2008; *Rychert et al.*, 2008). This feature could be related to the relatively low temperature in the corner of the mantle wedge, which is also dry and isolated from the viscous flow in the mantle wedge (*Kincaid and Sacks*, 1997; *Manea et al.*, 2005).

The high-attenuation zone in the lower crust beneath and to the north of the TMVB correlates well with a low-resistivity zone known from MT studies along almost the same line as the MASE array (*Jödicke et al.*, 2006) (figure 2.9a). The contrast of attenuation in the lower crust between the forearc and other parts is also consistent with shear wave velocity results along the same cross section from a surface wave study (*Iglesias et al.*, 2010) (figure 2.9b). The high attenuation, low resistivity and low velocity of the lower crust zone beneath and to the north of the TMVB suggest that it might be caused by fluids and partial melts. The flattening of the slab is thought to have occurred in the Early to Middle Miocene, when the NNW-trending Sierra Madre Occidental transitioned to the EW-trending TMVB (*Ferrari et al.*, 1999). During the Late Miocene, an eastward-migrating pulse of mafic volcanism took place in central Mexico, mostly to the north of the TMVB. At 7.5–6.5 Ma, this mafic pulse reached northern Veracruz state where the northern end of the MASE array passes (*Ferrari*, 2004). The imaged high-attenuation zone in the crust to the north of the TMVB is probably related to partial melts and metamorphic fluids produced in magmatic events such as the mafic pulse at 7.5–6.5 Ma. The mafic pulse is proposed to have resulted from eastward-propagating slab detachment (*Ferrari*, 2004). This slab tear hypothesis is also supported by the current slab image (*Pérez-Campos et al.*, 2008), which suggests that the slab in the Guerrero region broke at a depth of 80 km, and underwent rollback after that (*Pérez-Campos et al.*, 2008), causing trench-ward migration of the volcanic front (*Ferrari et al.*, 1999). The imaged high-attenuation zone in the crust beneath the TMVB is probably caused by the partial melts related to volcanism for the past $\sim$20 Ma. It could also be related to fluids stored in the lower crust, which were released from the oceanic crust and sediment when the slab was flat or shallow below the TMVB during the flattening and rollback periods. The relatively high attenuation in the upper crust could be partly due to the smearing from the lower crust attenuation as shown in figure 2.8b, and partly due to the presence of fluids or partial melts.

The broad low-attenuation area in the forearc below 40 km is likely due to the cold slab. It is artificially broadened because it actually represents a 2D projection of the slab's 3D geometry. The 3D variation of the slab geometry can also been seen from the widely

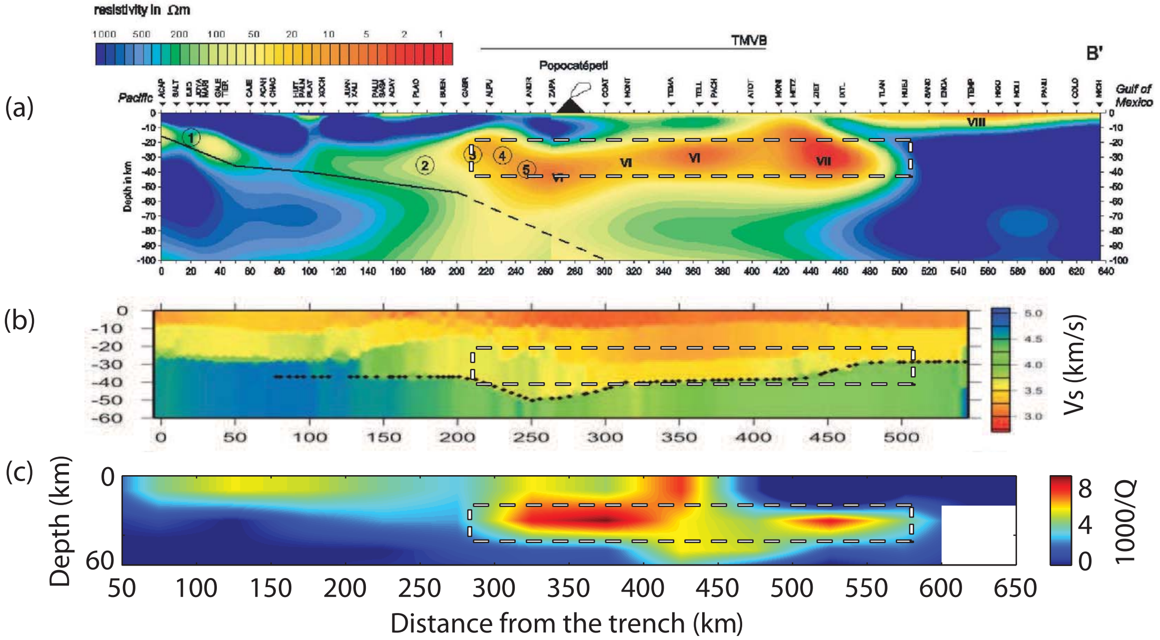

Figure 2.9. Comparison of different studies. (a) Resistivity results from an MT study along almost the same line as the MASE array (adapted from *Jödicke et al.*, 2006). (b) Shear wave velocity along the MASE array from a surface wave study (adapted from *Iglesias et al.*, 2010). (c) Attenuation inversion results from this study (only shallow part of the model is shown). The three plots are lined up and at the same 1:1 scale. The high-attenuation region in the crust correlates with low-resistivity and low-V_s region (highlighted by dashed boxes).

distributed location of the events used (figure 2.6).

In this study, inversion was done in a 2D cross section assuming that the attenuation structure has no variation along the strike of the trench due to the limitations of event-station pairs. However, the slab geometry in this region actually shows noticeable variation as we discussed in section 2.2. This should be kept in mind when interpreting the inversion results. Since the events used in this study are mostly far away from the MASE line, especially the deep ones, the attenuation image in the mantle wedge does not necessarily represent the structure directly beneath the MASE line but is biased to the east because of the location of the deeper events. The 2D attenuation image obtained in this study represents the attenuation structure in this region only in an average sense. Variations of attenuation along the strike of the trench are expected due to variations of tectonic structures. For example, during the data processing, we found that the waves traveling through the area west of the MASE line generally seem to attenuate more than waves traveling through the east area of the MASE line, indicating more attenuating crust or uppermost mantle in the western part of the MASE line. However, this may also be due to a bias in average source depth or distance. These effects could not be ruled out with the station geometry of the MASE experiment.

Our attenuation inversion results resemble studies in other subduction zones in the sense that the slab is characterized by low attenuation. However, there are a number of differences in attenuation models for other parts of the subduction system. In the southern part of northern Honshu (*Tsumura et al.*, 2000), Alaska (*Stachnik et al.*, 2004), Nicaragua and Costa Rica (*Rychert et al.*, 2008), the high-attenuation region mostly lies in the mantle wedge. In contrast, the attenuation model for northern part of northern Honshu (*Tsumura et al.*, 2000) shows a high-attenuation region in the crust beneath the volcanic belt. There are also other subduction zones such as central Andes (*Schurr et al.*, 2003) and New Zealand (*Eberhart-Phillips et al.*, 2008), where comparable high-attenuation zones exist both in the mantle wedge and the crust above. The attenuation model for central Mexico seems to belong to the third category. The attenuation structure of the mantle wedge in our model resembles the P-wave attenuation in Nicaragua (*Rychert et al.*, 2008) the most, with the center of the focused high-attenuation zone away from the top of the slab.

2.7 Conclusions

We have studied the P-wave attenuation structure in central Mexico using the spectral decay method, and obtained a 2D detailed image of attenuation in this region. The results show a generally low attenuation in the slab. High attenuation is found in both the mantle wedge and the crust. The high-attenuation region in the mantle wedge lies beneath the northern part of the TMVB between the depths of 80 and 120 km, with the lowest Q_p equal to 130. The high attenuation is in a compact region away from the top of the subducting slab and probably indicates where the most partial melts are produced during the subduction process. The high attenuation in the upper plate concentrates mostly in the lower crust. The high-attenuation zone to the north of the TMVB is likely to be related to extinct volcanoes. The high-attenuation zone in the crust beneath the TMVB is probably due to volcanism-related partial melts and fluids produced through dehydration process when the slab was undergoing flattening and rollback.

Chapter 3

Three-Dimensional Velocity and Attenuation Structure in Central and Southern Mexico

This chapter has been submitted by Ting Chen and Robert W. Clayton to *Journal of Geophysical Research*

3.1 Introduction

In the Mexican subduction zone, the Rivera and Cocos Plates subduct beneath the North American Plate along the Middle America Trench (figure 3.1). Although the subduction rate and plate age of the subducting plates both monotonically increase toward the southeast, the seismicity studies (*Pardo and Suárez*, 1995) suggest that the slab transitions from normal subduction in the north (Jalisco, Michoacán) to shallow subduction in the central segment (Guerrero), and then back to normal subduction in the south (Oaxaca). However, since the seismicity in central Mexico is sparse, the detailed structure of the slab and how the slab transitions from shallow to normal subduction is not well known.

The volcano distribution in this subduction zone also shows anomalous features. Volcanoes progressively shift from northern to central Mexico, and are about 300 km away

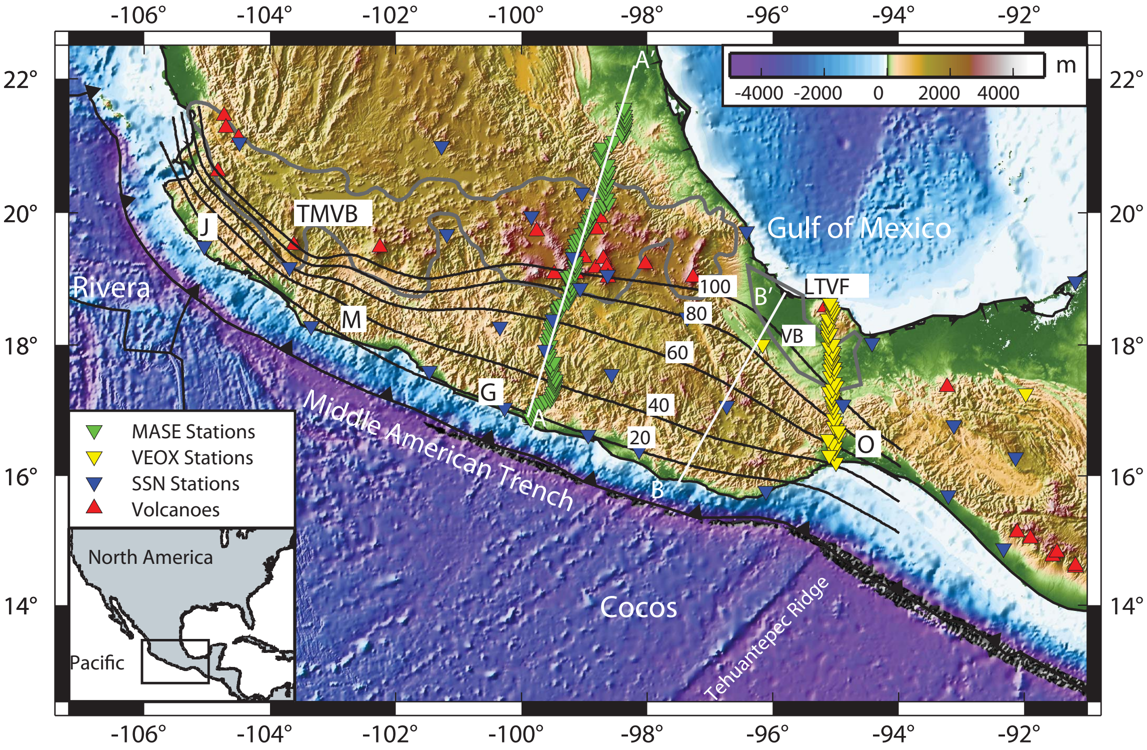

Figure 3.1. Map of the study region. Stations are marked by inverted triangles, and volcanoes are marked by red upright triangles. The Trans-Mexican Volcanic Belt (TMVB) and Veracruz Basin (VB) are outlined in light gray. White lines AA' and BB' are two MT surveys in *Jödicke et al.* (2006). LTVF denotes the Los Tuxtlas Volcanic Field. J (Jalisco), M (Michoacán), G (Guerrero), and O (Oaxaca) indicate four segments in this region. Slab iso-depth contours from *Pardo and Suárez* (1995) are shown by black lines.

from the trench near Mexico City, forming the Trans-Mexican Volcanic Belt (TMVB) with about a 16° angle to the trench. In southern Mexico, the continuous volcanic arc is missing where the Cocos slab is about 100 km deep, which is the typical depth for melt generation in subduction zones (*Wada and Wang*, 2009). Instead, the isolated Los Tuxtlas Volcanic Field (LTVF) is found near the Gulf of Mexico coast, which is about 150 - 200 km above the Cocos slab based on the extrapolation of seismicity (*Pardo and Suárez*, 1995). The TMVB is generally considered to be related to the subduction of the oceanic plate, with the volcano distribution following the geometry of the slab. The mechanisms of the origin of the LTVF, however, are unclear (e.g., *Nelson et al.*, 1995; *Ferrari et al.*, 2005; *Verma*, 2006).

A knowledge of the velocity structure in Mexico is important to an understanding of the tectonic evolution of the subduction system. Studies on the velocity of the crust and upper mantle in this region have been done using active sources and earthquakes (e.g., *Meyer et al.*, 1961; *Valdes et al.*, 1986; *Gomberg and Masters*, 1988; *Gomberg et al.*, 1988; *Campillo et al.*, 1996; *Shapiro et al.*, 1997). Most of these studies concentrate on small areas or only develop 1D models. A detailed 3D velocity model is needed to better understand the tectonic features.

Large coastal earthquakes pose a great threat to heavily populated Mexico City. Understanding what level of ground motions to expect in Mexico City from an earthquake is essential to effective hazard mitigation. Many attenuation studies have thus been conducted (e.g., *Castro et al.*, 1990; *Ordaz and Singh*, 1992; *Yamamoto et al.*, 1997; *Garcia et al.*, 2004; *Singh et al.*, 2006, 2007), but due to limited data, most of the studies are restricted to certain regions, and the results are path-averaged values. Attenuation tomography has also been done in this region (*Ottemöller et al.*, 2002), but it is of low spatial resolution, and only for the Lg waves. More detailed attenuation tomography resolving both the crust and the upper mantle is necessary to understand the subduction process. Attenuation complements the velocity studies, and helps to constrain the origin of anomalies.

Recently, a seismic array has been deployed in the Guerrero segment from Acapulco to the Gulf of Mexico. Receiver function studies (*Pérez-Campos et al.*, 2008; *Kim et al.*, 2010) along this array confirm the shallow subduction in central Mexico, and show that the Cocos slab is subhorizontal for about 250 km from the trench. Teleseismic velocity study images the deeper structure of the Cocos slab, and shows that the slab descends steeply (75°) into the mantle to a depth of 500 km beneath the TMVB (*Husker and Davis*, 2009). Surface waves reveal low velocity in the back arc, particularly in the lower crust beneath the TMVB (*Iglesias et al.*, 2010). The 2D attenuation images show relatively high attenuation in the mantle wedge and the lower crust beneath the TMVB (chapter 2). These studies along the same line provide a detailed 2D image of the subduction system from the coast to the back arc.

In this study, we seek to extend this image by constructing a 3D image of the subduction system in central and southern Mexico using a second array to the southeast and the permanent local stations.

3.2 Data

From 2005 to 2007, the Middle American Subduction Experiment (MASE) was conducted in central Mexico with a seismic line running perpendicular to the trench in the Guerrero region (figure 3.1). A total of 100 three-component broadband sensors were spaced about 5 km apart. From 2007 to 2009, 47 seismometers were deployed in southern Mexico crossing Veracruz and Oaxaca (VEOX). These two experiments, together with 46 stations of the National Seismological Service of Mexico (SSN), provide excellent data for detailed 3D velocity and attenuation imaging.

In this study, we analyzed 895 local events with magnitude between 3.5 and 5. Most of the events are deeper than 50 km. Crustal events are included only if the distance is less than 150 km to avoid the contamination of direct arrivals by other phases. The events are located by SSN using a 1D local velocity model (V. H. E. Castro and A. Iglesias, personal communication). The accuracy of the SSN catalogue is confirmed by a relocation study (*Alberto*, 2010). We also used 200 teleseismic events recorded by the VEOX array to perform a teleseismic velocity study.

For local events, arrival times are picked on the vertical component for the direct P wave and transverse component for the direct S wave. The algorithm based on the STA/LTA ratio is adopted to automate the picking process. The picked arrival times are then manually checked. For teleseismic events, the relative delay times are determined by cross correlation for the P phase with the distance between 30° and 90° and the PKPdf phase when the distance is larger than 155°.

3.3 Methods

3.3.1 Determining Attenuation Operator

The whole path attenuation can be described by the attenuation operator $t^* = \tau/Q$, where τ is the travel time, and Q is the average quality factor along the path. The amplitude of the velocity spectrum of a body wave from event j, and recorded at station i, can be written as (*Anderson and Hough*, 1984)

$$A_{ij}(f) = CS_j(f)I_i(f)\mathrm{exp}(-\pi f t^*_{ij}), \tag{3.1}$$

where $I(f)$ is the instrument response, C is the frequency-independent amplitude term related to geometric spreading, radiation pattern, and other static effects. The exponential term represents the attenuation effect. Assuming a Brune-type source (*Brune*, 1970), the source term $S(f)$ can be expressed as

$$S_j(f) = \frac{fM_{0j}}{1 + (f/f_c)^2}, \tag{3.2}$$

where M_{0j} is the seismic moment, and f_c is the corner frequency. After removing instrument response, the spectral amplitude has the following form:

$$A_{ij}(f) = \frac{C'f}{1 + (f/f_c)^2}\mathrm{exp}(-\pi f t^*_{ij}), \tag{3.3}$$

with C' being a combined constant.

We adopt the iterative approach of *Eberhart-Phillips and Chadwick* (2002) by first determining a common corner frequency f_c for each event using all the records from the event, and then obtaining frequency-independent t^*_{ij} and C' for each seismogram spectrum. We use the vertical component for the analysis of the P wave and transverse component for the analysis of the S wave. A 2.56 s time window starting from the onset of the arrival is used to calculate the signal spectrum, and a 2.56 s time window before the signal is used to calculate the noise spectrum. To ensure the high quality of t^* values used for the inversion, we apply the following selection criteria. For P waves, the signal-to-noise spectral ratio has to be larger than 2 over a 10 Hz frequency band from 2 to 40 Hz. For S waves, we lower the signal-to-noise ratio threshold to 1.5. For each event, there should be at least five t^* values. Unrealistic t^* values that correspond to Q larger than 3000 are also excluded. Examples of waveforms and spectral fits are shown in figure 3.2.

3.3.2 Tomographic Inversion

Arrival times for local P and S waves are inverted for 3D V_p and $V_\mathrm{p}/V_\mathrm{s}$ structure using the package SIMUL2000 (*Thurber*, 1993; *Eberhart-Phillips*, 1993; *Thurber and Eberhart-Phillips*, 1999). We parameterize the model by 3D grid with interval spacing of 150 km along the trench, 20 km perpendicular to the trench, and 20 km in the depth direction (figure 3.3). The initial model has P-wave velocity similar to the IASP91 model (*Kennett and Engdahl*, 1991), but with the Moho depth at 40 km based on receiver function studies in this region (*Kim et al.*, 2010, 2011). The initial $V_\mathrm{p}/V_\mathrm{s}$ ratio is uniform, and has the value of 1.73. Ray tracing is done in two steps: the approximate ray tracing and the

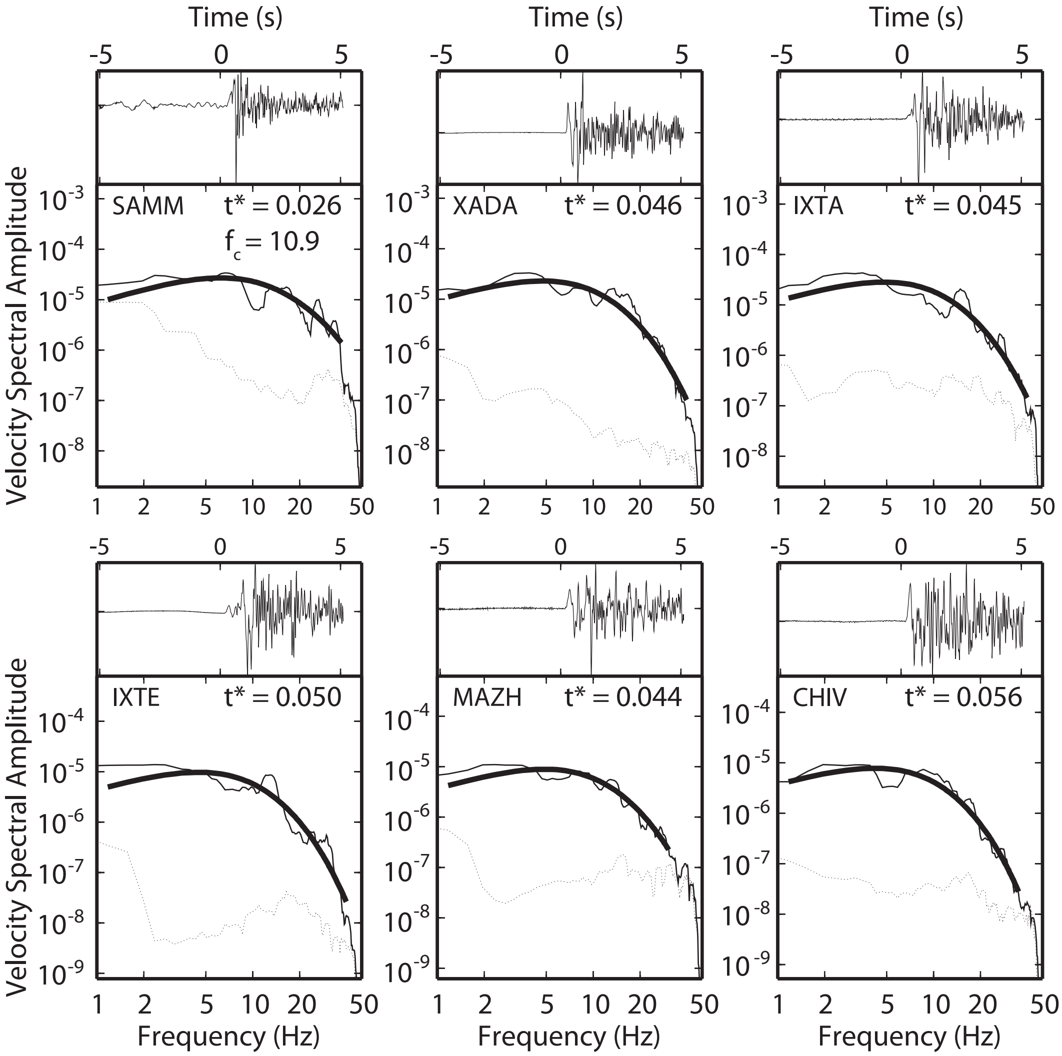

Figure 3.2. Examples of waveforms and t^* fits for one earthquake. For each station, the signal (solid line) and noise (dotted line) spectra are shown below the velocity waveform. The plotted velocity waveform is normalized by its peak amplitude. The fit to the spectrum is shown as a thick line over the range with adequate signal-to-noise ratio. A common corner frequency f_c for the event and different t^* for each record are estimated.

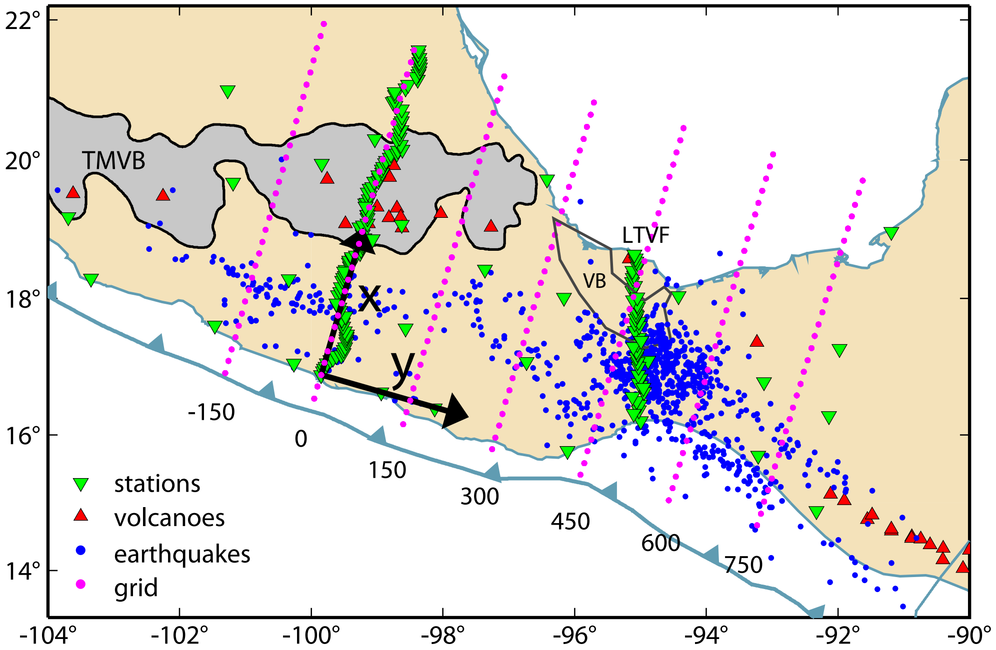

Figure 3.3. Grid, earthquakes, and stations used for velocity and attenuation inversion. The grid is spaced 150 km along the trench (y-axis), 20 km perpendicular to the trench (x-axis), and 20 km in the depth direction. Numbers denote the y coordinates of the grid in kilometer. TMVB: Trans-Mexican Volcanic Belt; VB: Veracruz Basin; LTVF: Los Tuxtlas Volcanic Field.

pseudobending (*Um and Thurber*, 1987). This ray tracing procedure has been shown to be effective and accurate for 3D velocity models, especially when modified to improve the performance for long ray paths (*Schurr et al.*, 2006). Earthquakes are relocated during the velocity inversion. The solution is the result of an iterative, damped least-squares inversion. The damping parameter is chosen based on the trade-off curve of data variance and model variance (*Eberhart-Phillips*, 1986).

The attenuation parameters t_p^* and t_s^* are used to invert for 3D P-wave and S-wave attenuation structure in a manner similar to the inversion for velocity. Travel times are computed with rays traced in the 3D velocity model obtained in this study. The same grid as with the velocity inversion is used. The initial attenuation model has a constant Q equal to 800. We solve $1/Q$ for each grid node in an iterative procedure.

We found that the noise levels on teleseismic records limit their usefulness in determining local attenuation structure. A 2D teleseismic velocity structure has already been obtained along the MASE array (*Husker and Davis*, 2009), and the local SSN stations are sparse between the MASE and VEOX arrays, so in this work we only invert for a 2D velocity structure along the VEOX array with the teleseimic study. Relative delay times for P and PKPdf phases are used to invert for the teleseismic P-wave velocity perturbation in a manner similar to the inversion for local velocity.

3.4 Resolution

We perform checkerboard tests to evaluate the resolution of the tomographic inversion. The input model consists of blocks of dimensions 80 km (x) $\times$ 600 km (y) $\times$ 80 km (z) with alternating positive and negative anomalies (figure 3.4, 3.5). Synthetic arrival times or attenuation operators with noise added are computed based on the input model, and then inverted in the same manner as the real data.

For V_p and Q_p, the crust is well resolved along the MASE ($y = 0$ km) and VEOX ($y = 450$ km) lines. The anomalies in the mantle near the VEOX line are also well recovered. The mantle near the MASE line is not resolved due to the absence of intermediate earthquakes in central Mexico. $V_\mathrm{p}/V_\mathrm{s}$ and Q_s generally have relatively lower resolution than V_p and Q_p, especially in the arc and back arc near the MASE line ($y = 0$ km). The streaks in the recovered models are related to dominant ray directions.

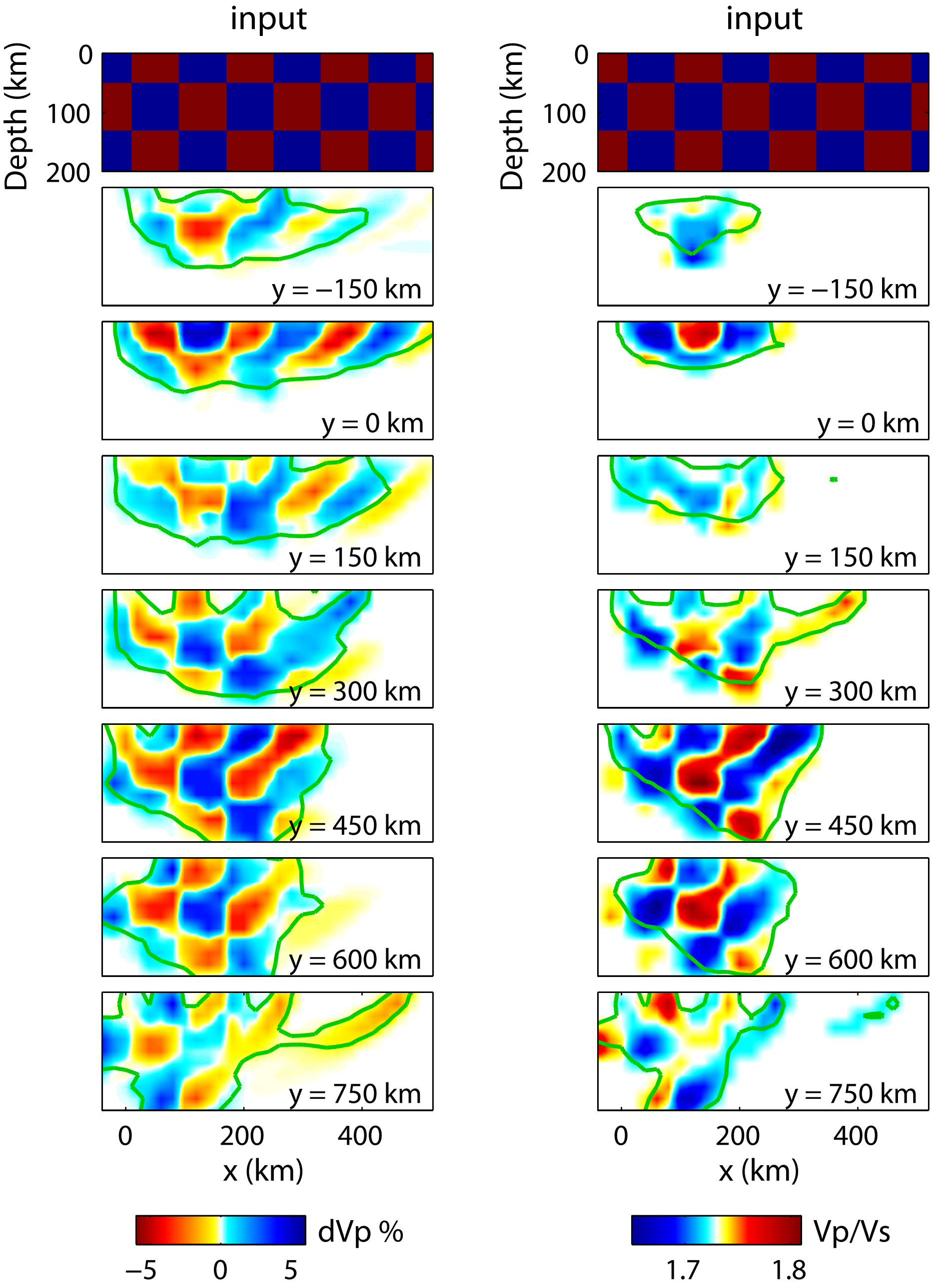

Figure 3.4. Checkerboard test for 3D P-velocity perturbation (left panel) and $V_{\mathrm{p}}/V_{\mathrm{s}}$ (right panel) inversion. The top panels show the input models for slices at $y = -150$, 0, and 150 km. The input models for slices at $y = 300$, 450, 600, and 750 km have opposite values of that shown in the top panels. The following panels are the recovered results for different slices along the x-axis. Green lines indicate the contour of the derivative weighted sum of 1000, and reasonably approximate the well-resolved region.

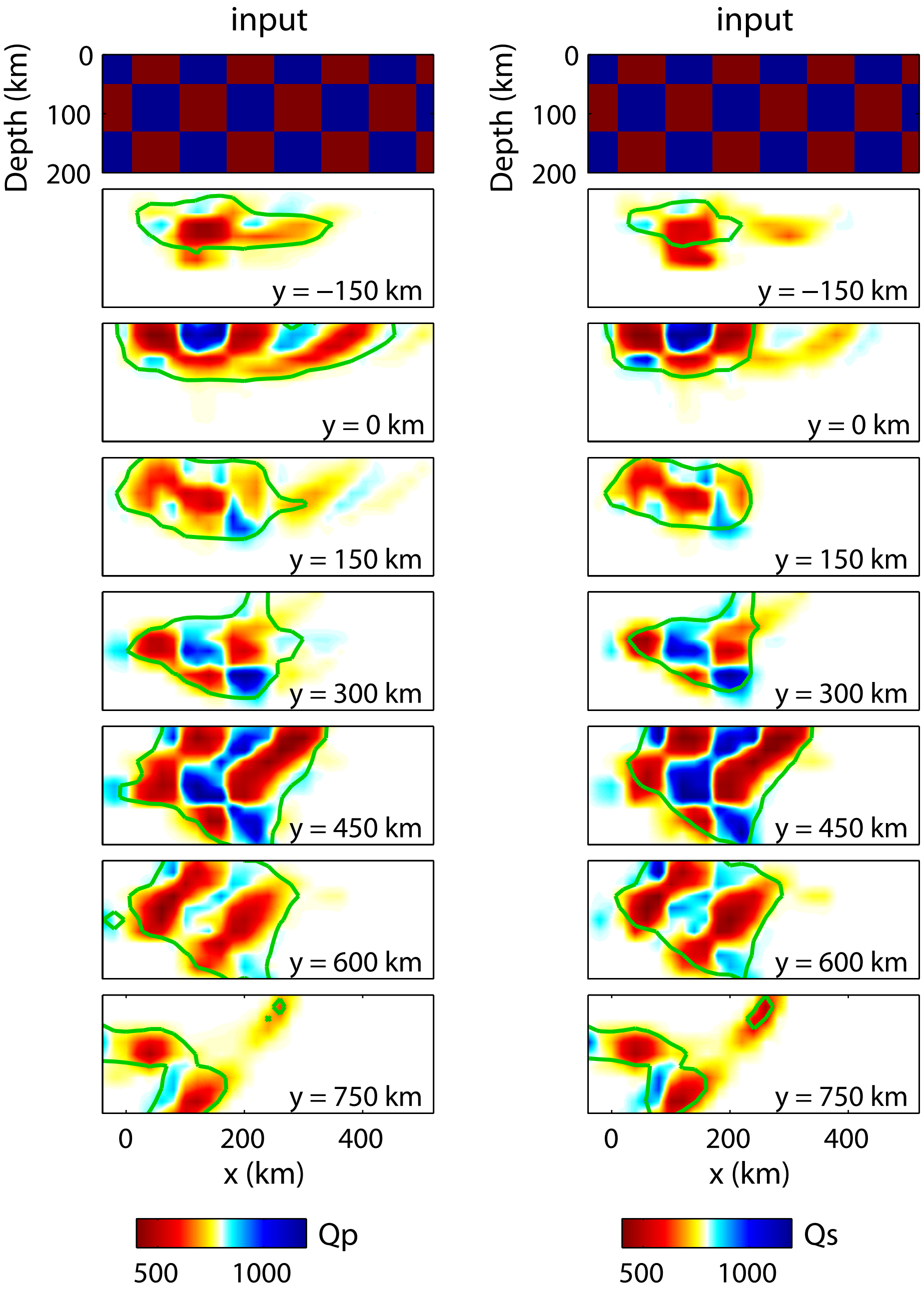

Figure 3.5. Checkerboard test for P-wave attenuation (left panel) and S-wave attenuation (right panel) inversion. The top panels show the input models for slices at $y = -150$, 0, and 150 km. The input models for slices at $y = 300$, 450, 600, and 750 km have opposite values of that shown in the top panels. The following panels are the recovered results for different slices along the x-axis. Green lines indicate the contour of the derivative weighted sum of 1000, and reasonably approximate the well-resolved region.

The quality of solution can also be evaluated using the derivative weighted sum (DWS). The DWS measures the ray density in the neighborhood of each node. Tests have shown that DWS tracks well with diagonal elements of the resolution matrix, and high DWS values correspond to high resolution and low smearing (e.g., *Hauksson*, 2000; *Rietbrock*, 2001). In figures 3.4 and 3.5, the contours of DWS values of 1000 coincide with well recovered regions from checkerboard tests. For the following plots of tomographic results, we use a DWS contour of 1000 to indicate the well resolved regions.

3.5 Results

3.5.1 Local Velocity and Attenuation

P-wave velocity results show considerable variation across the studied region (figure 3.6). High-V_p structure is imaged dipping northeast from the Pacific coast. Another prominent high-V_p structure is near the Gulf of Mexico coast on the VEOX line ($y = 450$ km), which is beneath the LTVF. Relatively low V_p values are observed in some part of the crust and the mantle wedge. The lowest-velocity anomaly lies in the crust at about $x = 220$ km near the VEOX line ($y = 450$ km), which is beneath the Veracruz Basin (VB). The lowest $V_\mathrm{p}/V_\mathrm{s}$ is found dipping southwest from the Gulf of Mexico at $y = 450$ km, and the highest $V_\mathrm{p}/V_\mathrm{s}$ is in the crust beneath the Veracruz Basin (figure 3.7).

P-wave attenuation results reveal a prominent low-attenuation ($Q \approx$ 1000–2000) structure dipping northeast from the Pacific coast (figure 3.8). The dip angle of this low-attenuation structure increases from about 0° in central Mexico ($y = 150$ km) to about 30°

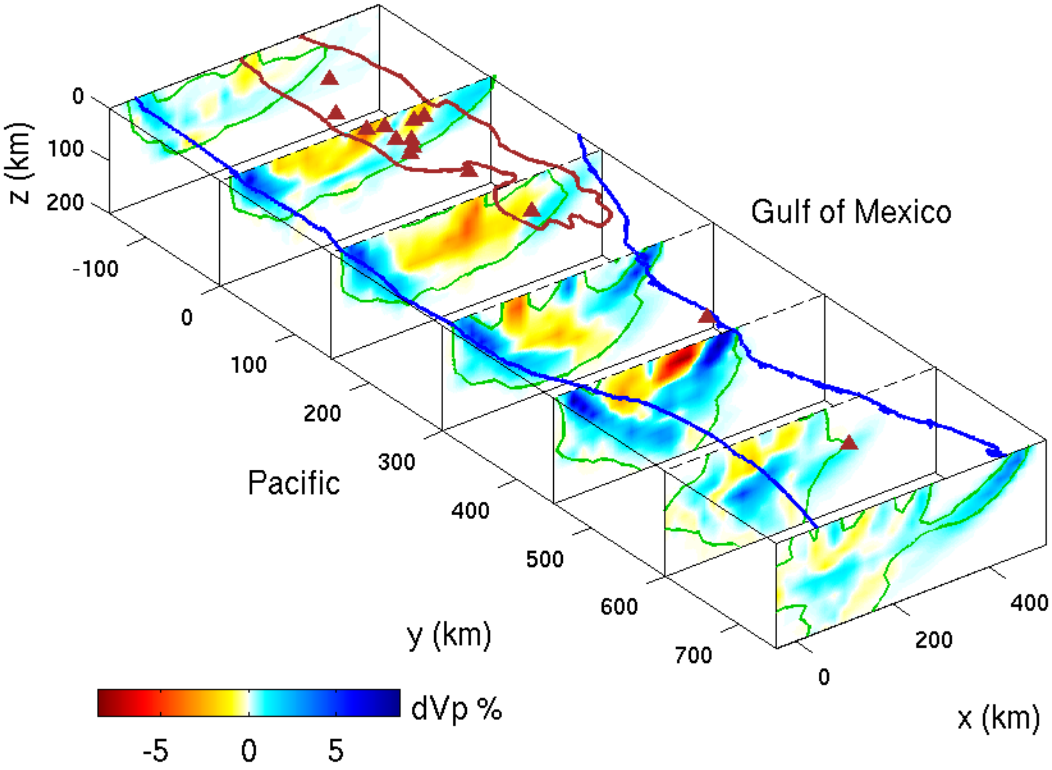

Figure 3.6. P-wave velocity perturbation results. Volcanoes are marked by red triangles. The TMVB and the coast are shown by red and blue lines respectively. Green lines are contours of the derivative weighted sum of 1000, and indicate the area with good resolution.

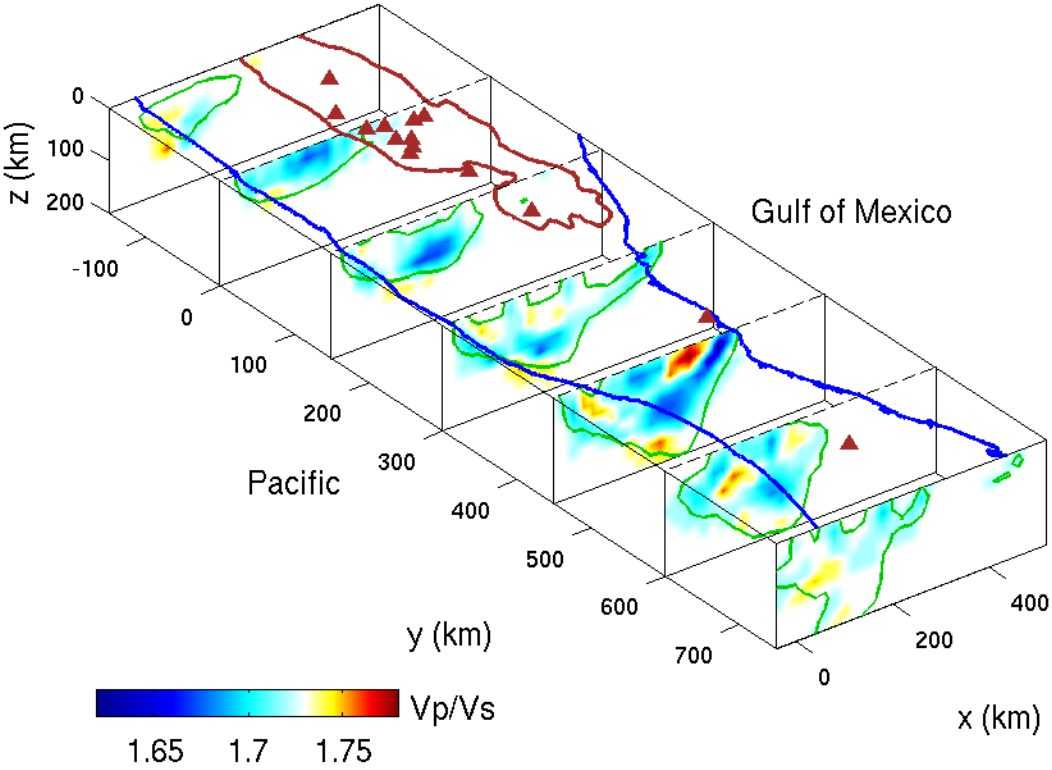

Figure 3.7. The $V_\mathrm{p}/V_\mathrm{s}$ results. Symbols are the same as in figure 3.6.

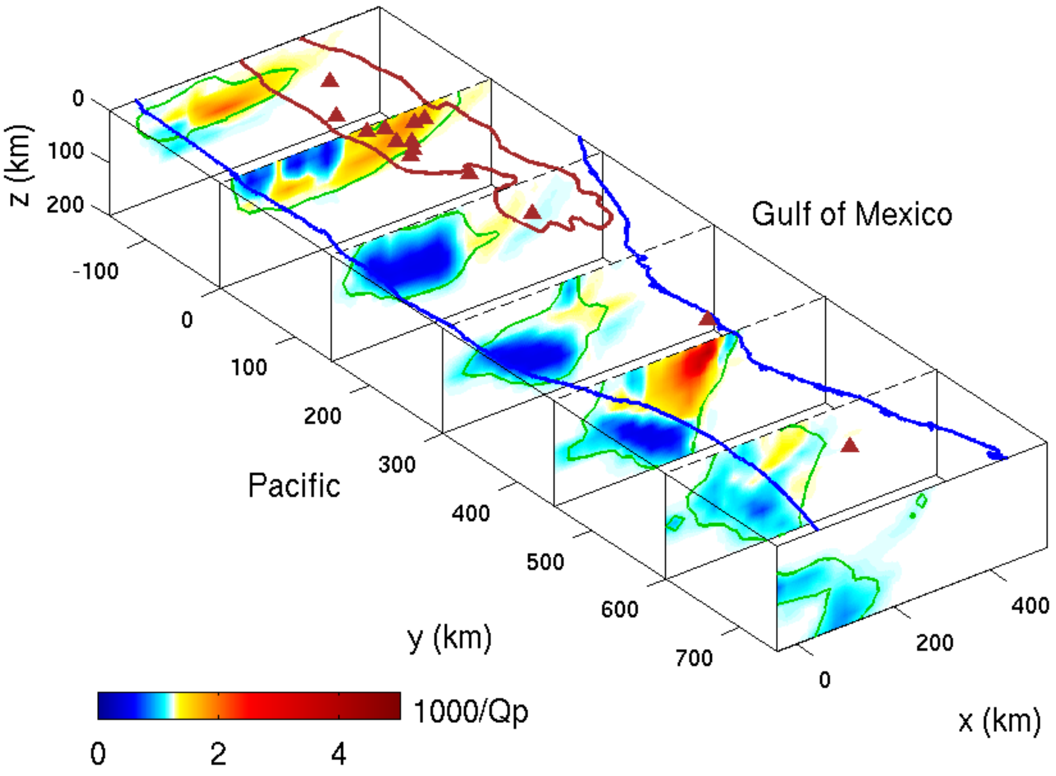

Figure 3.8. P-wave attenuation results. Symbols are the same as in figure 3.6.

near the Isthmus of Tehuantepec ($y = 450$ km). The dip angle appears to be even larger further to the south, but the resolution is limited. Low attenuation is also observed beneath the LTVF. The highest attenuation is imaged beneath the Veracruz Basin. A relatively high-attenuation anomaly is also found in the crust beneath the TMVB. S-wave attenuation results show similar features as the P-wave attenuation, but with stronger anomalies (figure 3.9). The low-Q_{p} anomaly in the crust beneath the TMVB does not appear in S-wave attenuation results due to the lack of resolution.

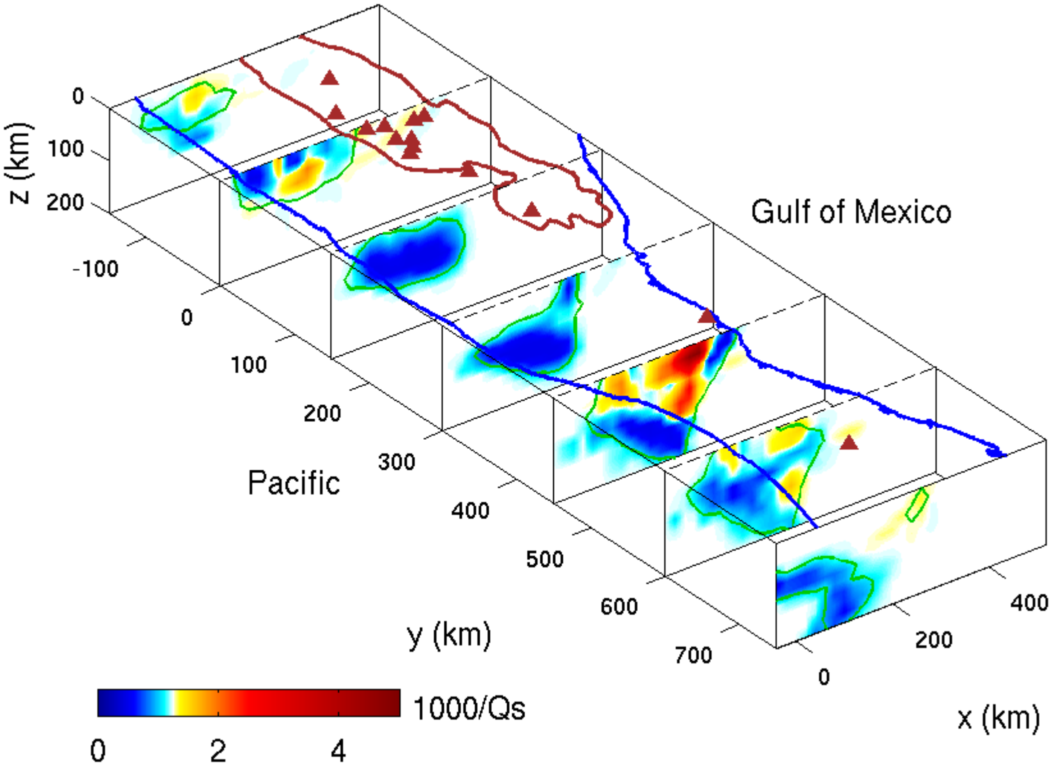

Figure 3.9. S-wave attenuation results. Symbols are the same as in figure 3.6.

3.5.2 Teleseismic Velocity

The teleseismic image along the VEOX array shows two dipping high-velocity structures (figure 3.10). One is dipping northward from the Pacific, and the other unexpected one is dipping southward from the Gulf of Mexico. The high-velocity structure dipping from the Pacific follows the earthquakes with a little larger dip angle. The high-velocity structure dipping from the Gulf of Mexico correlates with the discontinuity found by the receiver function study (*Kim et al.*, 2011). The stronger velocity anomaly also correlates with the stronger receiver function signals. The dip angle of the unexpected high-velocity structure is larger than the dip angle of the discontinuity shown by the receiver functions, but with the correction discussed in appendix 3.8, coincides with it. The high-velocity structure dipping from the Pacific is truncated by the high-velocity structure dipping from the Gulf of Mexico at the depth of about 150 km, and the truncation happens where the relocated events show a kink (*Alberto*, 2010). In the crust, low velocity is found beneath the Veracruz Basin, and high velocity is located beneath the forearc and the LTVF.

Resolution tests show that velocity anomalies dipping from either side can be resolved with a little smearing into the crust and the deeper mantle (figure 3.11g, h). The recovered dip angle, however, differs slightly from the input. The bias in the inverted dip angle is not due to the specific data coverage in this study, but generally due to the limited range of incidence angles for teleseismic study (appendix 3.8). The high-velocity structure dipping from the Gulf of Mexico is not just a smearing effect of the crustal anomalies to depth (figure 3.11f). The crustal variations in velocity can be resolved with our station spacing (figure 3.11e).

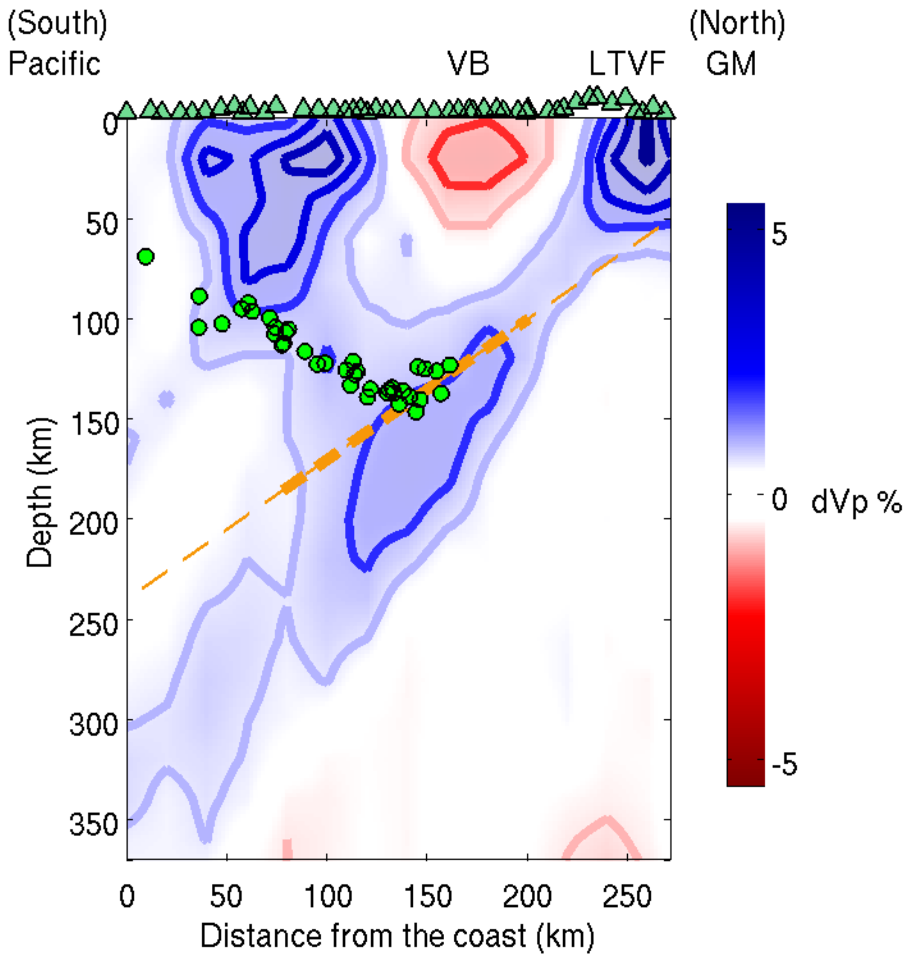

Figure 3.10. Teleseismic P-wave velocity perturbation inversion results along the VEOX array. Green dots denote the relocated events in this area (*Alberto*, 2010). Dashed line shows the discontinuity found by the receiver function study (*Kim et al.*, 2011); the most prominent part of the receiver function signals is highlighted by the thicker line. The green triangles are the VEOX stations. VB: Veracruz Basin; LTVF: Los Tuxtlas Volcanic Field; GM: Gulf of Mexico.

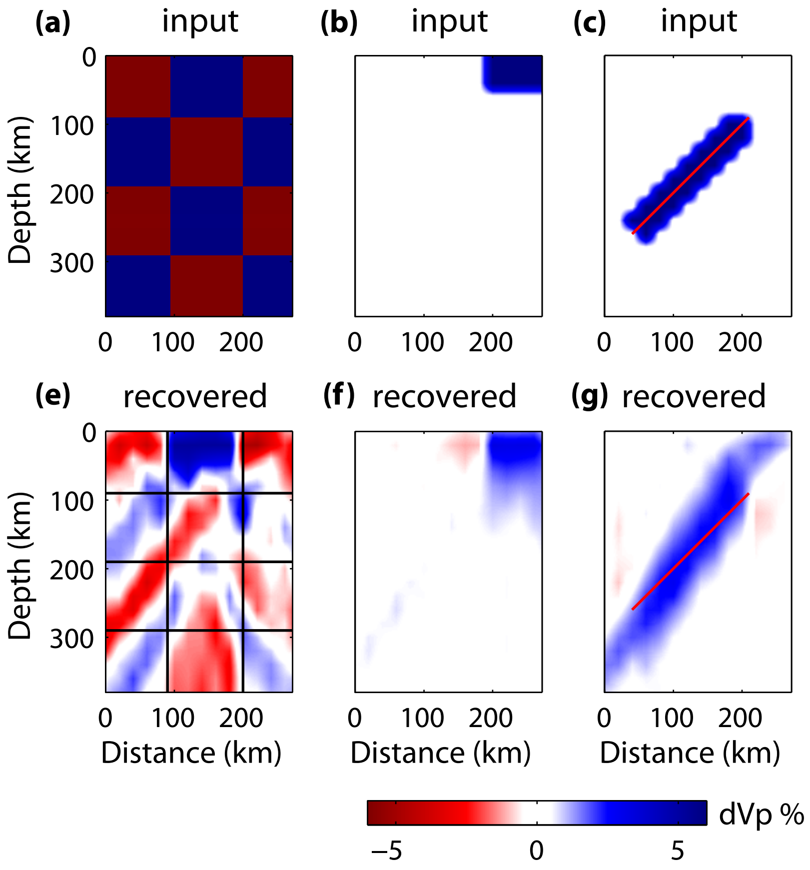

Figure 3.11. Resolution tests for the teleseismic P-wave velocity perturbation inversion. The top panels show the input models, and the lower panels show the recovered results. The x-axis is the distance from the coast along the VEOX array. The red lines in (g) and (h) are for reference, and they are the same as in (c) and (d) respectively.

3.6 Discussion

The 3D velocity structure correlates well with the attenuation structure. The velocity and attenuation results for the two slices best resolved are compared in figure 3.12 ($y = 0$ km, along the MASE array) and figure 3.13 ($y = 450$ km, near the VEOX array). As with other studies in subduction zones (e.g., *Tsumura et al.*, 2000; *Schurr et al.*, 2003; *Stachnik et al.*, 2004; *Rychert et al.*, 2008), our inversion results show that the slab is characterized by low attenuation and high velocity. The slab is also generally associated with low $V_\mathrm{p}/V_\mathrm{s}$. It is noteworthy that the slab seems to be even more evident in attenuation than in velocity, which was also observed by *Eberhart-Phillips et al.* (2008). The variation in the geometry of the Cocos slab is clearly imaged along the trench. The dip angle increases from about $0°$ in central Mexico near Mexico City to about $30°$ in southern Mexico near the Isthmus of Tehuantepec. Earthquakes are located within the high-velocity and low-attenuation slab. The cause of flat subduction in central Mexico is not well understood (*Skinner and Clayton*, 2011), and this study does not indicate a mechanism for the flattening.

High-attenuation and low-velocity anomalies are found in the crust. One such anomaly is in the crust beneath the TMVB near Mexico City (figure 3.12). This structure has also been shown in surface waves (*Iglesias et al.*, 2010) and imaged in a 2D attenuation study in this region (chapter 2). The relatively higher value of attenuation found in chapter 2 compared to in this study is due to the different inversion schemes. In particular, this study inverts for the results using an iterative approach starting with an initial model where unrealistic values are rejected, while chapter 2 uses a simple one-step damped least squares inversion without any constraints on the inverted parameters, which may result in more ex-

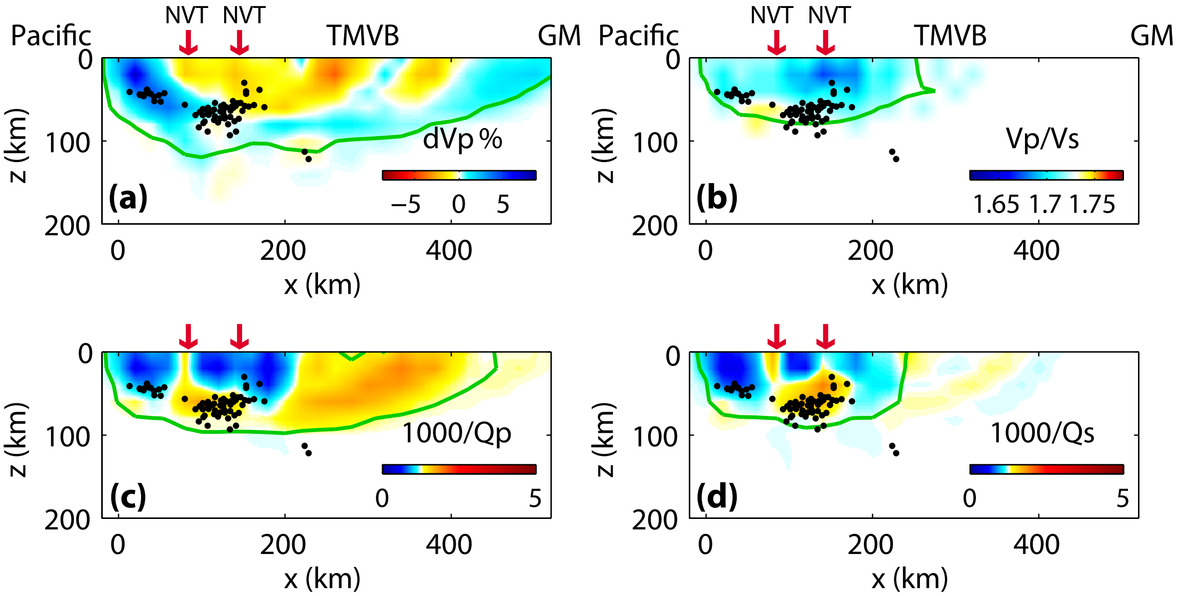

Figure 3.12. (a) P-wave velocity perturbation, (b) $V_\mathrm{p}/V_\mathrm{s}$, (c) P-wave attenuation and (d) S-wave attenuation results for the slice $y = 0$ km, which is perpendicular to the trench, and crosses the TMVB. Black dots are earthquakes within 100 km from this slice. Red arrows denote the locations of two nonvolcanic tremor (NVT) clusters from *Payero et al.* (2008). Green lines indicate the contour of the derivative weighted sum of 1000, and reasonably approximate the well-resolved region.

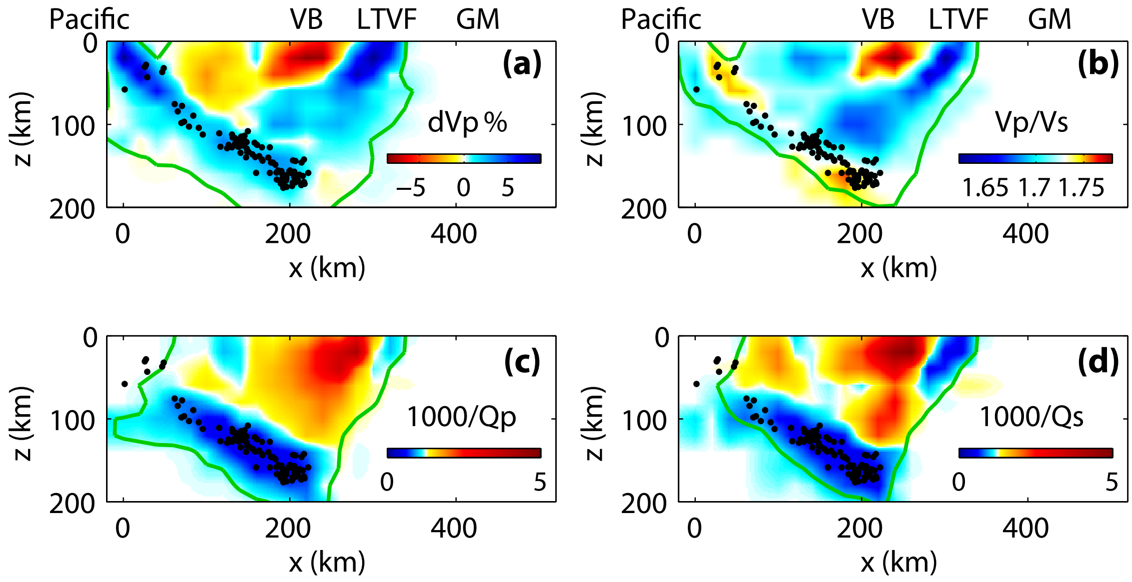

Figure 3.13. (a) P-wave velocity perturbation, (b) $V_\mathrm{p}/V_\mathrm{s}$, (c) P-wave attenuation and (d) S-wave attenuation results for the slice $y = 450$ km, which is perpendicular to the trench and near the Tehuantepec Ridge. Black dots are earthquakes within 100 km from this slice. Green lines indicate the contour of the derivative weighted sum of 1000, and reasonably approximate the well-resolved region.

treme values. The high-attenuation/low-velocity region correlates with the low-resistivity zone from an MT study along a nearby line (line AA' in figure 3.1) (*Jödicke et al.*, 2006). High heat flow is also observed in the TMVB (*Ziagos et al.*, 1985). The anomalies are probably caused by partial melts related to volcanism, or fluids released from the oceanic crust and sediments into the continental crust when the slab was underplating the continental crust beneath the TMVB during the flattening and rollback periods (*Pérez-Campos et al.*, 2008).

The most prominent high-attenuation/low-velocity anomaly lies in the crust beneath the Veracruz Basin near the Isthmus of Tehuantepec (figure 3.13). This anomaly also shows a high $V_\mathrm{p}/V_\mathrm{s}$ ratio. Our study of the teleseismic velocity shows this anomaly too (figure 3.10). Interestingly, MT studies along a line about 150 km to the west of the VEOX array (line BB' in figure 3.1) show that low resistivity is also found beneath the Veracruz Basin west of the LTVF (*Jödicke et al.*, 2006). The low-resistivity anomaly extends to the depth of about 40 km, which is about the same depth range where we see high attenuation, low-V_p and high $V_\mathrm{p}/V_\mathrm{s}$. The shallower part of this anomaly may be related to the Veracruz Basin, but the origin of the deeper part of this anomaly is not well understood. This anomaly may be related to some extinct volcanism in this complex tectonic region (*Jödicke et al.*, 2006).

Beneath the active LTVF, we observe high velocity, low $V_\mathrm{p}/V_\mathrm{s}$ and low attenuation (figures 3.10, 3.13). The high velocity beneath the LTVF has also been shown in a previous teleseismic P-wave velocity study in Mexico (*Gorbatov and Fukao*, 2005), but at a much coarser resolution. The properties of this anomaly suggest that there is no large-scale partial melting zone associated with this volcanic field. Part of the high velocity and low attenuation may also be due to the relatively shallow Moho ($\sim$30 km) in this area (*Kim et al.*, 2010; *Melgar and Pérez-Campos*, 2011; *Zamora-Camacho et al.*, 2010). The high velocity in the crust near the Pacific coast ($y = 0$ km, $y = 150$ km, $y = 300$ km and $y = 450$ km) and the crust near the Gulf of Mexico coast ($y = 300$ km and $y = 750$ km) may also be due to the fact that the Moho in that area is shallower than the reference Moho depth (*Castro*, 2009).

Based on synthetic tests, the imaged dipping high-velocity structure from the teleseismic study may have a somewhat steeper angle than the real structure, especially for smaller dip angles (figure 3.11 and appendix 3.8). Along the VEOX line, the seismicity and the opposite-dip anomaly from the receiver function studies both have relatively small dip angles of about 30° and 35°, respectively. Using an empirical correlation, the high-velocity structure dipping from the Pacific actually aligns with the relocated events, indicating the origin of the anomaly is the Cocos slab. With the correction, the high-velocity structure dipping from the Gulf of Mexico also has a dip angle similar to the discontinuity shown by the receiver function study (*Kim et al.*, 2011). *Kim et al.* (2011) proposed that the unexpected slab from the Gulf of Mexico is caused by subduction of oceanic lithosphere before the collision between the Yucatán Block and Mexico in the Miocene. Our study shows that the Cocos slab is truncated by the Yucatán slab at the depth of about 150 km. The break-off of the Cocos slab further to the south has also been proposed by *Rogers et al.* (2002). In the teleseismic P-wave tomographic image of *Rogers et al.* (2002), the remnant of the Cocos slab is seen at the depth of about 500 km in the Gulf of Mexico, resulting a slab gap about 350 km wide. The unusual slab geometry near the Isthmus of Tehuantepec is likely to have a major effect on the dynamics of subduction in this region, and may shed light on the origin of the complex tectonic features (*Kim et al.*, 2011).

Near the Isthmus of Tehuantepec, the mantle wedge shows moderate attenuation, relatively high V_p and low $V_\mathrm{p}/V_\mathrm{s}$ (figure 3.13), indicating a lack of partial melt. This suggests that the flow in the mantle wedge is constricted due to the geometry of the opposing Yucatán slab, and can explain the absence of a volcanic arc about 100 km above the Cocos slab. Low $V_\mathrm{p}/V_\mathrm{s}$ have also been observed in the flat subduction wedge of the Andes (*Wagner et al.*, 2005). At shallower depth above the Cocos slab, we observe relatively high attenuation, low V_p and moderate $V_\mathrm{p}/V_\mathrm{s}$. This may be related to the release of volatiles from the oceanic sediment and crust or only partially serpentinized forearc mantle. Low V_p and moderate $V_\mathrm{p}/V_\mathrm{s}$ in the forearc mantle were also observed in the shallow Hikurangi subduction zone in New Zealand (*Eberhart-Phillips and Chadwick*, 2002).

In the Guerrero segment, two clusters of nonvolcanic tremor (NVT) are observed above the flat slab (*Payero et al.*, 2008). The depths of NVT are distributed between 5 and 40 km. The high attenuation we image above the flat slab shows some correlation with the location of NVT, especially for the S-wave attenuation (figure 3.12). The $V_\mathrm{p}/V_\mathrm{s}$ ratio, on the other hand, does not apparently correlate with the location of NVT. Although some relatively high $V_\mathrm{p}/V_\mathrm{s}$ is found near the plate interface, it is not as high as what is found in Japan where NVT occurs ($V_\mathrm{p}/V_\mathrm{s} > 1.8$) (*Shelly et al.*, 2006; *Matsubara et al.*, 2009). This may indicate that the NVT in Guerrero is related to fluid release, but not necessarily highly overpressured free water.

3.7 Summary

We have obtained 3D velocity and attenuation structure in central and southern Mexico. The results image the low-attenuation and high-velocity Cocos slab with the dip angle increasing from being almost flat in the central Guerrero segment to about $30°$ in the southern Oaxaca segment. High-attenuation and low-velocity anomalies are found beneath the TMVB and Veracruz Basin. An unexpected high-velocity structure dipping into the mantle from the Gulf of Mexico near the Isthmus of Tehuantepec is imaged by the telseismic study. We interpret this unexpected dipping structure as the Yucatán slab caused by the collision between the Yucatán Block and Mexico in the Miocene. The Cocos slab is truncated by the Yucatán slab at the depth of about 150 km, and this configuration likely changes the convective flow in the mantle wedge.

3.8 Appendix: Synthetic Tests for Dipping Structures with Teleseismic Data

To understand the difference between the recovered dip angle and the input dip angle of the velocity anomaly with teleseismic data in figure 3.11, we have done some synthetic tests. For a given input model, we construct the synthetic data by ray tracing earthquakes through the input model to each station on the VEOX array. Two types of synthetic tests have been done. In the first one, we fix the dip angle of the velocity anomaly to be $45°$, and invert for the model using different earthquakes. Three different sets of teleseismic earthquakes are used. Each set consists of earthquakes of the same distance ($40°$, $60°$ or

80°) but different azimuths (0°, 90°, 180° and 270°). In the second one, we vary the dip angle of the velocity anomaly from 30° to 60° , and invert for the model using the same set of earthquakes. The distances of earthquakes vary from 30° to 90° with an increment of 10°, and for each distance, different azimuths (0°, 90°, 180° and 270°) are covered.

The synthetic tests show that for a given dipping structure, the inversion with earthquakes of shorter distance has smaller bias in the dip angle (figure 3.14a–c). For the inversion with earthquakes covering distances between 30° and 90°, the bias in the dip angle is smaller for more steeply dipping structure (figure 3.14d–f). The dip bias is introduced by the anisotropic shape of the point-spread function that is caused by the limited range of incidence angles.

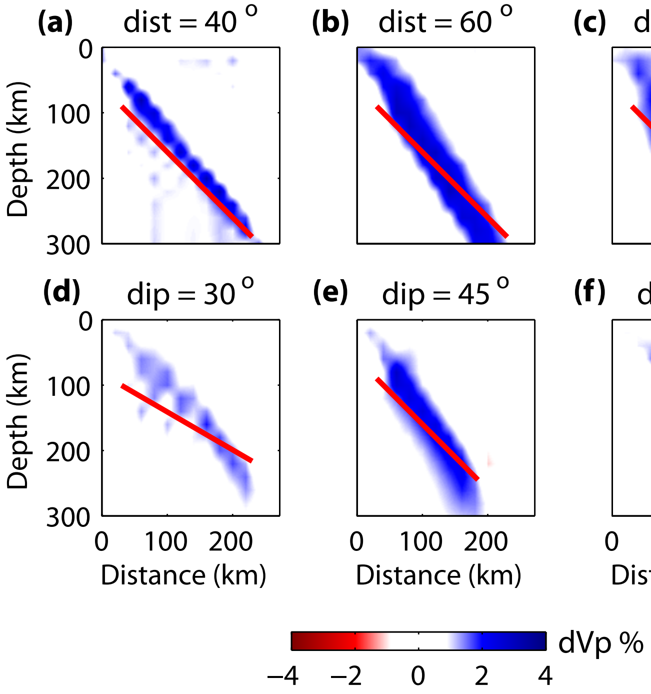

Figure 3.14. (a–c) Synthetic tests for a dipping structure of 45° using teleseismic earthquakes of different distances. (d–f) Synthetic tests for dipping structures of different degrees using teleseismic earthquakes with distances from 30° to 90°. Thickness of the anomaly is about 50 km and the position is indicated by the red line.

Part II: Physics of Small Repeating Earthquakes

Chapter 4

Scaling of Small Repeating Earthquakes Explained by Interaction of Seismic and Aseismic Slip in a Rate and State Fault Model

This chapter was originally published by Ting Chen and Nadia Lapusta (2009) in *Journal of Geophysical Research, 114*, B01311, doi:10.1029/2008JB005749.

4.1 Introduction

Repeating earthquakes are seismic events that repeatedly occur in the same location with similar seismic signals. Sequences of small repeating earthquakes have been found on a number of faults (*Ellsworth and Dietz*, 1990; *Vidale et al.*, 1994; *Nadeau and Johnson*, 1998; *Bürgmann et al.*, 2000; *Igarashi et al.*, 2003; *Peng and Ben-Zion*, 2005; *Chen et al.*, 2007). Since their recurrence times range from a fraction of a year to several years and their locations are known, small repeating earthquakes are an excellent observation target. This has been exploited in a number of studies, such as the San Andreas Fault Observatory at Depth (SAFOD) drilling project (*Hickman et al.*, 2004) (figure 4.1). Repeating earthquakes are used to study an increasingly richer array of problems, from fault creeping velocities and postseismic slip to earthquake interaction and stress drops (*Ellsworth and Dietz*, 1990; *Vidale et al.*, 1994; *Marone et al.*, 1995; *Nadeau and Johnson*, 1998; *Schaff et al.*, 1998; *Nadeau and McEvilly*, 1999; *Bürgmann et al.*, 2000; *Igarashi et al.*, 2003; *Nadeau et al.*, 2004; *Schaff and Beroza*, 2004; *Matsubara et al.*, 2005; *Peng and Ben-Zion*, 2005; *Allmann and Shearer*, 2007; *Chen et al.*, 2007; *Dreger et al.*, 2007). To assimilate and properly interpret the wealth of data on small repeating earthquakes, it is important to construct a realistic model of their occurrence.

One of the intriguing observations about small repeating earthquakes is the scaling of their seismic moment M_0 with the recurrence time T as

$$T \propto M_0^{0.17}. \tag{4.1}$$

This scaling has been first pointed out by *Nadeau and Johnson* (1998) for repeating earthquakes along the Parkfield segment of the San Andreas fault, and it has since been confirmed in other tectonic environments (*Chen et al.*, 2007). However, a simple conceptual model of these events as circular ruptures, with stress drop $\Delta\tau$ independent of the seismic moment M_0 and slip equal to $V_\mathrm{L}T$, where V_L is the long-term slip velocity (also called slip rate) accommodated by the fault segment, results in (*Nadeau and Johnson*, 1998; *Beeler et al.*, 2001)

$$T = \Delta\tau^{2/3} M_0^{1/3}/(1.81\mu V_\mathrm{L}) \propto M_0^{1/3}, \tag{4.2}$$

where μ is the shear modulus of the bulk. Note that this model assumes that all slip at the

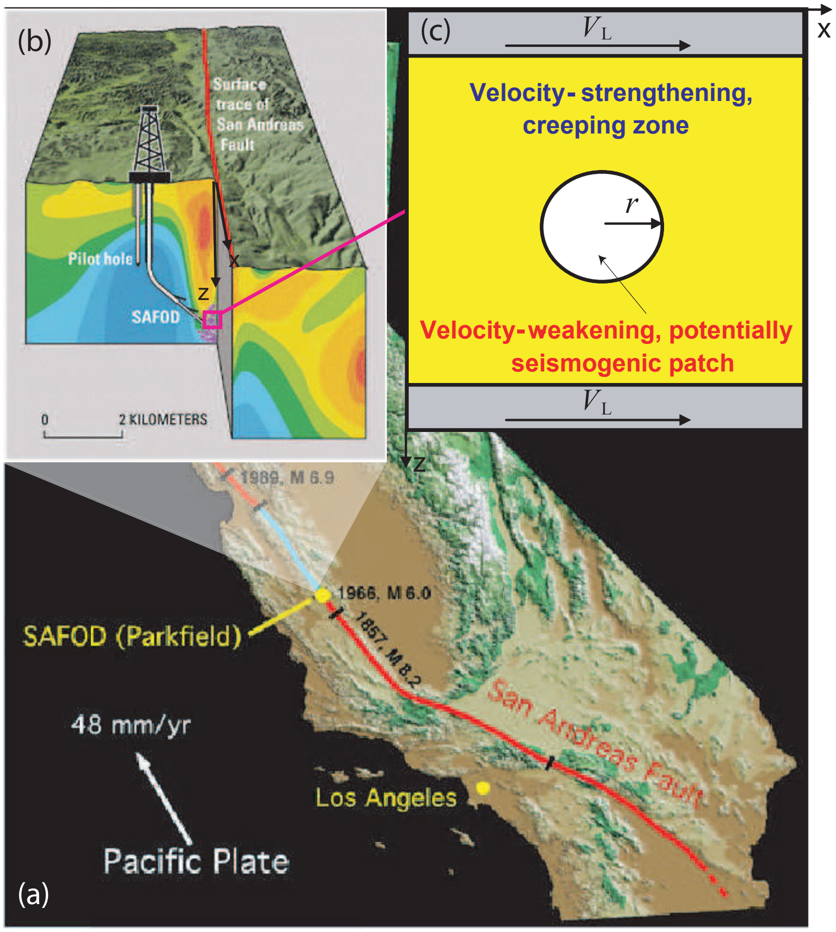

Figure 4.1. Schematics of the model. To simulate repeating earthquakes, such as (b) the targets of the SAFOD drilling project on (a) the Parkfield segment (shown in blue) of the San Andreas fault, we consider a segment of a vertical strike-slip fault embedded into an elastic medium and governed by rate and state friction laws. (c) On the fault, a small, potentially seismogenic, patch with steady-state velocity-weakening properties (shown in white) is surrounded by a creeping, velocity-strengthening segment (shown in yellow). Outside of the simulated fault segment, steady sliding is imposed with the long-term slip velocity V_L. The creeping (yellow) zone is chosen to be large enough so that the model behavior does not depend on its size. (SAFOD schematics courtesy of Dr. Stephen Hickman.)

location of repeating earthquakes is accumulated seismically. The observed and theoretical scalings have different exponents as well as different absolute values of recurrence times. If T is measured in second and M_0 is measured in dyne centimeter (*Nadeau and Johnson*, 1998; *Chen et al.*, 2007), the Parkfield observations are well approximated by $T = 7 \times 10^4 M_0^{0.17}$, while the theoretical model gives $T \approx 2.4 M_0^{1/3}$ for typical values $\Delta\tau = 3$ MPa, $\mu = 30$ GPa, and $V_{\mathrm{L}} = 23$ mm/a (*Nadeau and Johnson*, 1998). Thus the observed recurrence times are much larger than the theoretical ones for moment magnitudes typical for small repeating earthquakes. Several explanations for the discrepancy in scaling and recurrence times have been proposed (*Nadeau and Johnson*, 1998; *Beeler et al.*, 2001; *Anooshehpoor*, 2001; *Sammis and Rice*, 2001). In the work of *Nadeau and Johnson* (1998), it was interpreted as an indication of the dependence of stress drop on seismic moment, with higher stress drops for smaller events. However, to fit the observed recurrence times, stress drops for the smallest repeating earthquakes would have to be as high as 2500 MPa (*Nadeau and Johnson*, 1998). Not only is the physical basis for stress drops of such high values unclear (*Beeler et al.*, 2001), but also recent seismic estimates of stress drops for repeating earthquakes in Parkfield (*Imanishi et al.*, 2004; *Allmann and Shearer*, 2007) have pointed to values of the order of 1 to 10 MPa, the typical range for earthquakes in general (*Abercrombie*, 1995). The work of *Sammis and Rice* (2001) presented a model with the observed scaling $T \propto M_0^{1/6}$ in which repeating earthquakes occur on small seismogenic patches located at the boundary between much larger creeping and locked regions. The small patches are assumed to be much weaker than the larger locked region, so that the patches fail many times before the larger region is ready to rupture. The model achieves the correct scaling due to stress concentration at the boundary. The corresponding stress drops are relatively small, 0.5 to 0.08 MPa for the larger locked regions with radii of 100 m to 2 km. Such small stress drops would correspond to much smaller slips than would be necessary to accommodate the long-term slip of the fault segment, and it is postulated that most of the slip at the location of repeating earthquakes would be accumulated when the larger locked region fails. Hence the model of *Sammis and Rice* (2001) predicts that there are larger locked regions within the creeping section of the San Andreas fault that should fail in much larger earthquakes than the repeating events discussed here. However, currently there is no evidence for such events. The potential importance of aseismic slip at the location of repeating earthquakes was highlighted in the study by *Beeler et al.* (2001), which used a spring-slider (one-degree-of-freedom) model governed by a constitutive law that incorporated strain hardening in the interseismic period. In the model, part of the accumulated slip was aseismic, due to strain-hardening behavior, and the resulting scaling of the seismic moment with the recurrence time had a trend similar to the one observed. However, *Beeler et al.* (2001) pointed out that there was no experimental evidence for the strain-hardening law used in the model.

In this work, we demonstrate that the observed scaling is reproduced in a model of repeating earthquakes that treats them as frictional instabilities on a fault in an elastic medium and incorporates laboratory-derived rate and state friction laws (*Dieterich*, 1979, 1981; *Ruina*, 1983; *Marone*, 1998; *Dieterich*, 2007, and references therein). Rate and state friction laws have been successfully used to model a number of fault-slip phenomena as discussed in a recent review by *Dieterich* (2007). For the case of constant normal stress σ, a commonly adopted form of the law is

$$\tau = \sigma[f_0 + a\ln(V/V_0) + b\ln(V_0\theta/L)], \tag{4.3}$$

$$d\theta/dt = 1 - V\theta/L, \tag{4.4}$$

where V is slip velocity, θ is a state variable, L is the characteristic slip for state-variable evolution, V_0 and f_0 are the reference slip velocity and friction coefficient respectively, and a and b are rate and state parameters. We use a regularized version of the law at $V = 0$ (*Lapusta et al.*, 2000). The "aging" formulation (4.4) for the state-variable evolution incorporates strengthening (or healing) of the fault in stationary contact, a feature needed to explain laboratory observations (*Beeler et al.*, 1994). Recent experiments (*Bayart et al.*, 2006) suggested that the "slip" formulation (*Dieterich*, 1979, 1981; *Ruina*, 1983) may be a better description of the friction response for the range of slip velocities studied in the experiments. Perhaps a combined law, of the type proposed by *Kato and Tullis* (2001), would be the most appropriate one to use. Different state evolution laws cause differences in the process of earthquake nucleation (*Ampuero and Rubin*, 2008) and hence it would be important to examine the behavior of our model with other state-evolution laws. We discuss this issue further in section 4.6.

The parameter combination $a - b > 0$ corresponds to steady-state velocity-strengthening properties while $b - a > 0$ corresponds to steady-state velocity weakening. In the following, we refer to fault regions as being velocity strengthening or velocity weakening with the implicit understanding that the characterization applies to the steady-state behavior.

Velocity-strengthening fault zones tend to respond to slow loading with stable, aseismic slip, while velocity-weakening zones of sufficiently large sizes can produce inertially controlled seismic events (*Rice and Ruina*, 1983; *Dieterich*, 1992; *Rubin and Ampuero*, 2005). Sufficiently small regions on velocity-weakening faults can also slip aseismically, leading to aseismic nucleation processes. For $0.5 < a/b < 1$, the range of parameters that includes the representative laboratory values of a and b used in this work, the half-size of the slipping region capable of producing seismic slip under slow loading can be estimated as (*Rubin and Ampuero*, 2005)

$$h^*_{RA} = \hat{\mu} bL/(\pi\sigma(b-a)^2), \tag{4.5}$$

with $\hat{\mu} = \mu$ for antiplane sliding and $\hat{\mu} = \mu/(1-\nu)$ for inplane sliding, where ν is the Poisson's ratio. The 3D nucleation estimates obtained from the same considerations as the 2D estimates of *Rubin and Ampuero* (2005) would be larger by a factor of $\pi^2/4$ [*A. Rubin*, personal communication].

4.2 Model for Repeating Earthquakes

We consider a planar fault embedded in an elastic medium and numerically simulate the behavior of a finite fault region around the location of a repeating earthquake (figure 4.1). The elastodynamic properties of the medium are as follows: shear modulus $\mu = 30$ GPa, Poisson's ratio $\nu = 0.25$, the shear wave speed $c_s = 3$ km/s, and the P-wave speed $c_p = 5.2$ km/s. On the fault, a potentially seismogenic, circular patch of radius r is surrounded by a much larger creeping zone. The difference in behavior between the patch and the surrounding area is achieved by assigning velocity-weakening properties, $b - a > 0$, to the patch and velocity-strengthening properties, $a - b > 0$, to the surrounding fault zone. In all simulations, the size of the velocity-strengthening zone is kept at least four times larger than the patch radius. Outside the velocity-strengthening zone, steady sliding with the long-term slip velocity V_{L} is imposed, to model steady creep (i.e., slow slip) of the surrounding fault area. We solve for spontaneous slip history in this model using the 3D simulation methodology of *Lapusta and Liu* (2009), which fully resolves all aspects of seismic and aseismic behavior of the fault, including long aseismic periods of slip with velocities of the order of millimeters per year, accelerating and decelerating aseismic slip in the interseismic period, all inertial effects during simulated earthquakes with slip velocities of the order of one meter per second, and postseismic slip. The model of repeating earthquakes as shear ruptures on seismogenic patches embedded into a larger creeping fault region has been shown to be consistent with the observed postseismic response of repeating aftershocks on the San Andreas Fault (*Schaff et al.*, 1998). *Kato* (2004) used a similar (but quasi-dynamic) model to study interactions between two sequences of repeating earthquakes.

In all our simulations, we use effective normal stress $\sigma = 50$ MPa and the reference friction coefficient $f_0 = 0.6$ at $V_0 = 1$ μm/s. In simulations presented in section 4.3 and part of section 4.4, we adopt the following values of rate and state parameters representative of laboratory results: $L = 160$ μm, $a = 0.015$, and $b - a = 0.004$ for the velocity-weakening patch, and $a = 0.019$ and $a - b = 0.004$ for the surrounding velocity-strengthening zone. To investigate how the behavior varies with friction parameters, we have explored a range of values for the rate and state parameters a and b (section 4.4), making the velocity-weakening parameter $(b - a)$ on the patch two times larger and two times smaller and studying a different value of a. In each case, the properties of the velocity-strengthening zone are assigned by switching the values of a and b. Two values of long-term slip rate are used: $V_{\mathrm{L}} = 23$ mm/a (based on *Nadeau and Johnson*, 1998) and $V_{\mathrm{L}} = 4.5$ mm/a. The fault is discretized into rectangular cells that are $\sim$10-20 times smaller than $h^*_{RR} = \hat{\mu}\pi L/[4\sigma(b - a)]$ (*Rice and Ruina*, 1983). Such discretization is adequate for both nucleation processes and the cohesive zone at the rupture tip as discussed in *Lapusta and Liu* (2009). (The quasi-static value of the cohesive zone is related to h^*_{RR} through the factor of $(b - a)/b$.) The results of several conceptually important simulations were confirmed with finer resolutions.

4.3 Model Response for Different Patch Sizes

As predicted by studies of stability of frictional sliding (section 4.1), most of the velocity-strengthening part of the fault accumulates slip through stable sliding with the imposed long-term slip rate V_{L}. The behavior of the velocity-weakening patch depends on its radius, consistent with the findings of stability studies that a sufficiently large velocity-weakening region is required for unstable slip. For sufficiently small values of r, the velocity-weakening patch accumulates slip through perturbed but aseismic sliding, with slip velocities that never deviate too much from the long-term slip velocity V_{L}. Velocity-weakening patches of larger sizes produce repeating earthquakes. This is illustrated in figure 4.2, which shows the history of maximum slip velocity on the fault for four values of the patch radius r. For all values of r and for most of the simulated time, the maximum slip velocity is close to the imposed long-term velocity of $V_{\mathrm{L}} = 23$ mm/a (which translates into a value slightly smaller than 10^{-9} m/s), due to stable sliding of the velocity-strengthening zone away from the velocity-weakening patch. The presence of the patch results in periodic increases of maximum slip velocity. We take 1 cm/s as the value separating seismic and aseismic slip rates. For the properties used in this section ($L = 160\ \mu\mathrm{m}$, $a = 0.015$, $b - a = 0.004$, $\sigma = 50$ MPa), the radius of the smallest patch that results in seismic slip in our simulations is $r = 83$ m. Values of r smaller than 83 m result in aseismic slip velocity at all times, although the maximum slip velocity during accelerations of the patch increases as r approaches the critical size (figures 4.2a and 4.2b). Values of r larger than 83 m result in periodic excursions of slip velocity to values larger than 1 cm/s, indicating repeating earthquakes (figures 4.2c and 4.2d). The seismogenic patches can create additional complexity in slip patterns. For example, $r = 150$ m results in transient increases of slip velocity before repeating earthquakes (figure 4.2d), as discussed further in section 4.3.2. The estimate (4.5) gives $h^*_{RA} = 36$ m for antiplane sliding and $h^*_{RA} = 48$ m for inplane sliding, which is consistent, in view of the 3D factor $\pi^2/4$, with the critical patch radius $r = 83$ m of our simulations. Note that the model with $r = 94$ m has a maximum slip velocity of 0.07 m/s while the model with $r = 100$ m has a maximum slip velocity of 0.17 m/s. Hence changing the threshold separating aseismic and seismic slip velocities to 0.1 m/s would result in the critical patch size between 94 and 100 m.

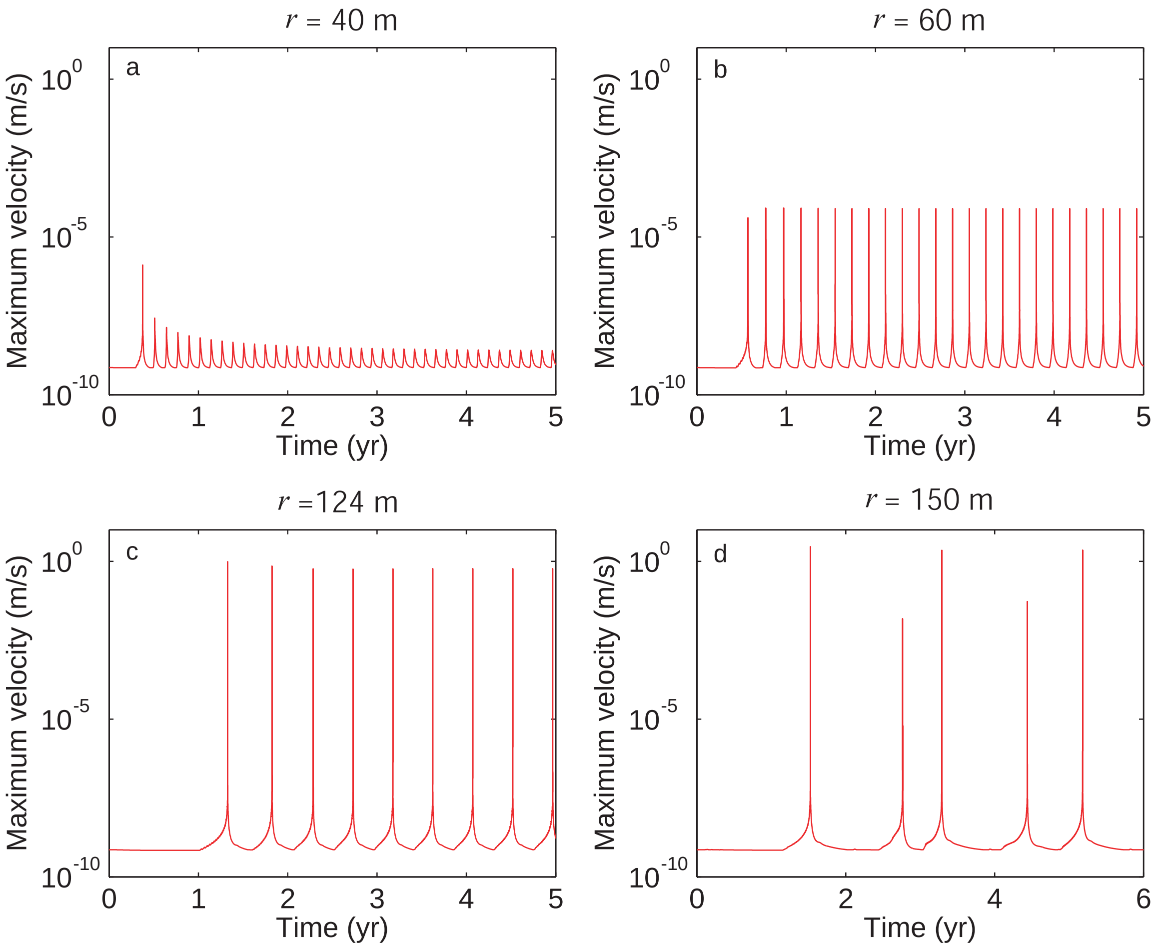

Figure 4.2. Maximum slip velocity over the fault as a function of simulated time, plotted for different radii of the velocity-weakening patch: (a) $r = 40$ m, (b) $r = 60$ m, (c) $r = 124$ m, (d) $r = 150$ m. Smaller values of r result in aseismic behavior of the patch, with slip velocities never approaching seismic values (panels a and b), while larger values of r result in sequences of repeating earthquakes (panels c and d). This behavior is consistent with stability properties of rate and state faults.

4.3.1 Response of Patches That are Just Large Enough to Produce Seismic Events

One seismic cycle from a simulation with $r = 124$ m is illustrated in figure 4.3. This patch size is only slightly larger than the critical patch size of 83 m. At some point in time during the interseismic period, most of the velocity-weakening patch is locked; figure 4.3a shows the distribution of slip velocity over a part of the fault close to the velocity-weakening patch at the time of 0.08 years after a seismic event (which occurs at the simulated time of 2.28 years). As the simulated time progresses, the locked area shrinks due to penetration of stable slip from the velocity-strengthening zone surrounding the patch (figure 4.3b). This is consistent with the stability properties of velocity-weakening regions in which slip over small zones can be stable. Eventually, slip accelerates (figure 4.3c) and fast (seismic) slip occurs (figure 4.3d) at the simulated time of 2.73 years. The interseismic period in this case is 0.45 years. Postseismic slip continues on the patch for a while (figures 4.3e and 4.3f), eventually affecting the velocity-strengthening zone surrounding the patch (figure 4.3g). Finally, the patch becomes locked again (figure 4.3h), and the earthquake cycle repeats. It is important to point out that, for this value of r, the extent of seismic slip, shown in red in figure 4.3, is a small fraction of the velocity-weakening patch. This means that sizes of repeating earthquakes inferred based on seismic data may be smaller than the underlying velocity-weakening patches that cause them.

In this model, a significant part of slip at the location of the velocity-weakening patch is accumulated aseismically. Continuing with the example of $r = 124$ m, let us consider the history of maximum slip velocity and moment accumulation on the patch (figure 4.4).

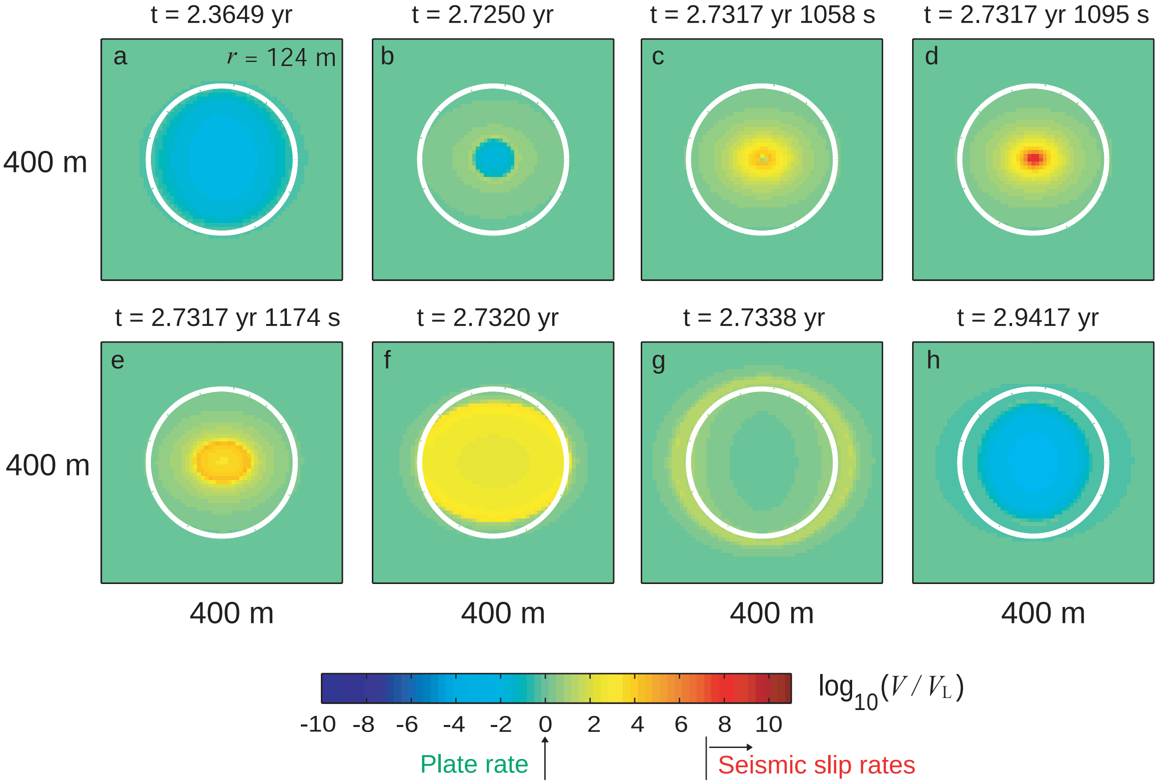

Figure 4.3. Snapshots of slip velocity distribution for one earthquake cycle and $r = 124$ m. Slip velocity is color coded on the logarithmic scale. The seismic range of slip velocities is indicated by red colors, and slip velocities close to the long-term slip velocity are indicated by green. The location of the patch is outlined by a white circle. The simulated fault region is 800 m × 800 m; only a part of it is shown in each snapshot. Much of slip on the patch is accumulated aseismically (orange, yellow, and green colors). Note that, in this simulation, the extent of seismic slip is smaller than the size of the patch. The simulations fully account for both slow aseismic slip and inertial effects during seismic events.

On the scale of years, the history of maximum slip velocity on the fault (figure 4.4a) points to the occurrence of repeating earthquakes, as already discussed. The cumulative moment release on the velocity-weakening patch (figure 4.4d) has the corresponding step-like nature, with most moment released near the time of the seismic events. However, even on this scale of years, we already see that a significant fraction of moment, about one third, is released during aseismic periods, when the maximum slip velocity is within an order of magnitude from the long-term slip velocity $V_{\mathrm{L}} = 23$ mm/a. This is due to penetration of slip from the creeping region into the locked patch, as shown in figure 4.3b. On the scale of tens of thousands of seconds or several hours (figures 4.4b and 4.4e), the seismic event is still too short to see in detail, but it is clear, from comparison of panels 4.4b and 4.4e, that the moment released with seismic slip velocities is much smaller than the moment released during postseismic slip with slip velocities of the order of 10^{-6} m/s. The histories of the maximum slip velocity and moment released during the seismic event itself are shown in figures 4.4c and 4.4f. The moment magnitude of the seismic event is $M_{\mathrm{w}} = 0.9$. In this simulation, the ratio of seismic and total moments on the patch is less than 0.01, indicating that more than 99% of slip on the patch is accumulated aseismically. Note that we find such a small contribution of seismic moment only for patch sizes that are just large enough to produce seismic slip. That makes intuitive sense, since slightly smaller patches would be completely aseismic.

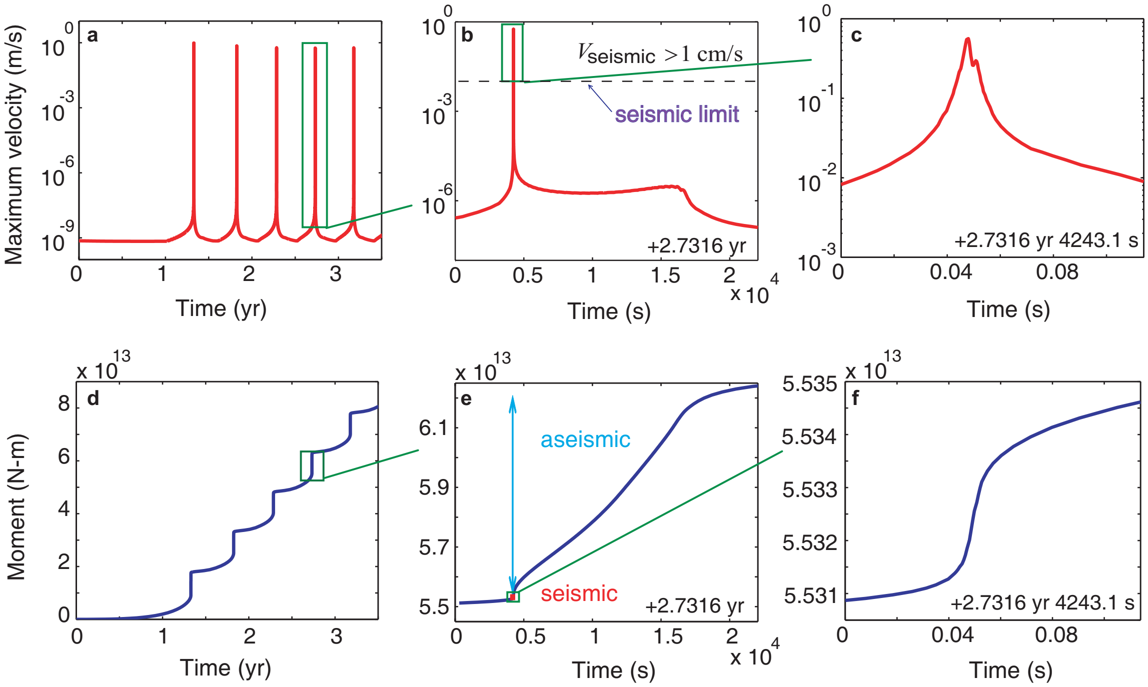

Figure 4.4. (a-c) Maximum slip velocity over the fault as a function of simulated time, plotted on different temporal scales, for $r = 124$ m. (d-f) Cumulative moment release on the velocity-weakening patch for the same time intervals. We see that seismic moment, defined as moment released with the maximum slip velocity larger than 1 cm/s, is only a small fraction of the total moment released on the patch, and there is significant pre- and postseismic slip.

4.3.2 Response of Larger Patches

As shown in section 4.3.1, the velocity-weakening patches that are just large enough to be seismogenic produce seismic slip only over a part of the patch and result in very small ratios of seismic to total slip on the patch, less than 0.01. For larger patches, seismic slip extends to the entire area of the patch. The change in the behavior occurs rather sharply at about $r = 130$ m. As an illustration, consider one seismic cycle from a simulation with $r = 150$ m shown in figure 4.5. At some point in time during the interseismic period, most of the velocity-weakening patch is locked (figure 4.5a), similarly to the case of $r = 124$ m. Figure 4.5a corresponds to the time of 0.07 years after a seismic event (which occurs at the simulated time of 5.18 years). As the simulated time progresses, the locked area shrinks due to penetration of stable slip from the velocity-strengthening zone surrounding the patch, until the entire patch slides aseismically (figure 4.5b). The middle of the patch experiences accelerated slip, with slip velocity that briefly reaches the seismic slip threshold of 0.01 m/s at a small portion of the patch (figure 4.5c), before slip velocities decrease (figure 4.5d) and most of the patch becomes locked again (figure 4.5e). The creep-in of the slow slip repeats, causing another acceleration of slip in the middle of the patch (figures 4.5f-h), which finally results in a patch-spanning seismic event (figure 4.5i and 4.5j) at the time of 6.81 years. The interseismic period in this case is 1.63 years. The event is followed by postseismic slip (figure 4.5k). In this case, the moment magnitude of seismic events is $M_{\mathrm{w}} = 2.9$ and the ratio of seismic to total moment on the patch is about 0.3.

Hence we find that, for $r = 150$ m, the entire patch is involved in seismic slip eventually. In that regard, the behavior is similar to that of even larger patches, as discussed in the

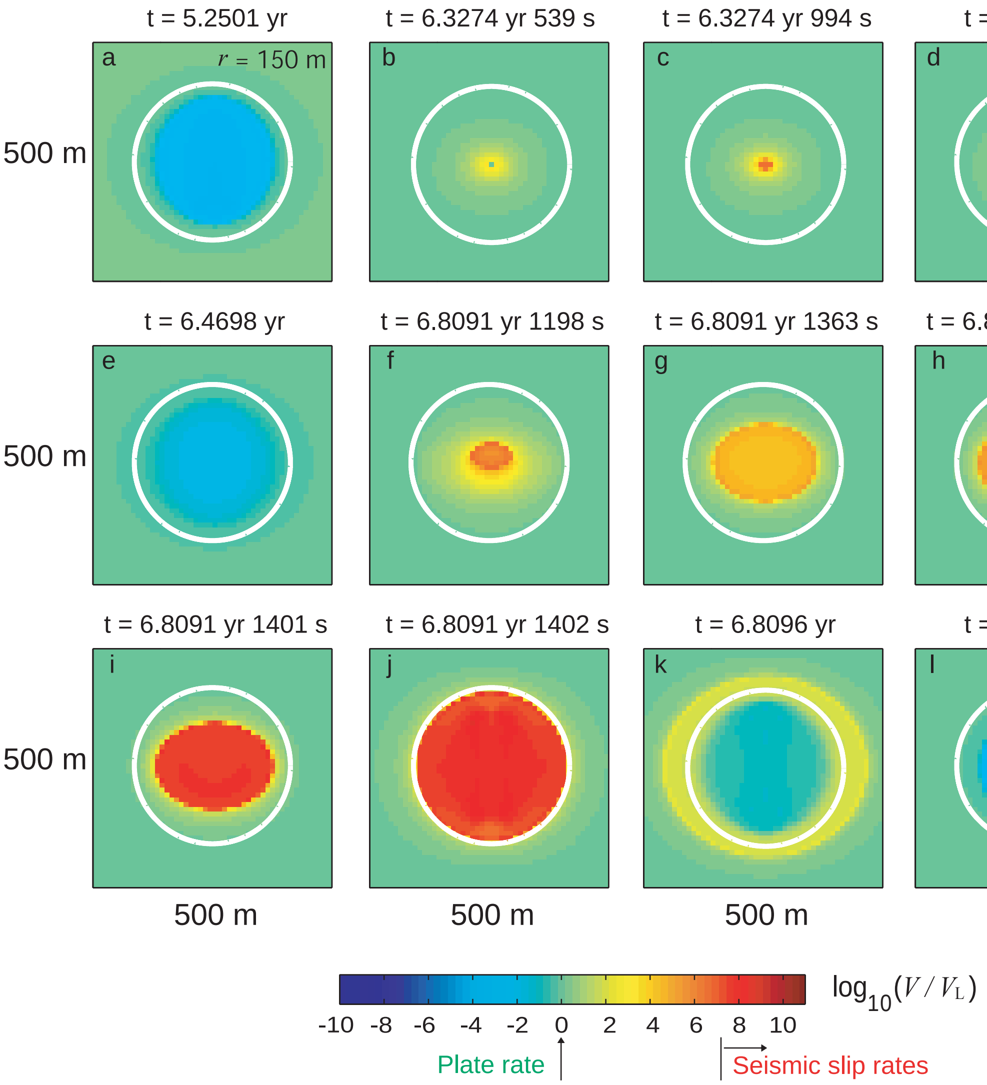

Figure 4.5. Snapshots of slip velocity distribution for one earthquake cycle and $r = 150$ m. Colors and markings have the same meaning as in figure 4.3. The simulated fault region is 1200 m $\times$ 1200 m; only a part of it is shown in each snapshot. As in the case of $r = 124$ m (figure 4.3), there is significant aseismic slip over the entire patch and seismic slip eventually initiates from the middle of the patch. However, unlike in the case of $r = 124$ m, seismic slip extends over the entire patch.

following. However, there are also similarities with the case of $r = 124$ m. First, the entire patch experiences aseismic slip before a dynamic event. Second, the behavior of slip is still nearly axisymmetric, modulated only by the difference between the antiplane (Mode III) and inplane (Mode II) sliding directions. In part, seismic slip still originates in the middle of the patch and expands towards the boundaries.

For larger patches, the middle part of the patch remains locked when a dynamic event starts. Figure 4.6 shows one seismic cycle from a simulation with $r = 350$ m. As the simulated time progresses, the locked area shrinks due to penetration of stable slip from the velocity-strengthening zone surrounding the patch (figures 4.6a and 4.6b), as in the previous cases. However, slip acceleration starts close to the boundary of the patch (figures 4.6c and 4.6d) and seismic slip initiates when a significant part of the patch is still locked (figure 4.6e). The seismic event then propagates unidirectionally through the patch (figures 4.6e-4.6h). This is different from the cases of smaller patches in figures 4.3 and 4.5, where seismic slip initiates from the middle of the patch. Postseismic slip follows the dynamic event, both on and off the patch (figures 4.6i-4.6k). In this case, the moment magnitude of seismic events is $M_\mathrm{w} = 3.7$, the interseismic time is 2.17 years, and the ratio of seismic to total moment on the patch is about 0.8. The behavior of the velocity-weakening patch qualitatively resembles that of the fault model in *Lapusta and Liu* (2009), where much larger fault dimensions and characteristic slips L are used to simulate large strike-slip earthquakes (large values of L were used in *Lapusta and Liu* (2009) for numerical tractability). Note that the half size of the actively slipping zone when seismic slip velocities are reached is about 130 m in the inplane (Mode II) direction and about 90 m in the antiplane (Mode III) direction (figure 4.6e), with the latter value being very close to the critical patch radius of 83 m.

The patterns of seismic and aseismic slip can exhibit additional complexity. The behavior shown in figures 4.5b-4.5d corresponds to the increase of maximum slip velocity in figure 4.2d between larger repeating earthquakes. Such increases in the interseismic period occur for some patch radii, as in our example with $r = 150$ m, but not others, and these transients are often completely aseismic. When they do develop slip velocities that we treat as seismic, their seismic moment is orders of magnitude smaller than that of the larger repeating events that occur in the same simulations. In such cases, we use the larger events to infer the seismic moment and recurrence interval. Note that even if we counted the occasional much smaller events as part of the repeating earthquake sequence and included them in the computation of the repeat time and average seismic moment for each repeating sequence, the resulting values would still be consistent, within the scatter, with the scaling discussed in the next section. Another type of complex response arises for patches that are large enough to retain a locked region before the dynamic event, such as our example with $r = 350$ m. After the aseismic slip penetrates into the patch, an aseismic transient propagates along the creeping rim of the patch. Figure 4.6b actually shows such a transient in action, with its two fronts (appearing in light-yellow color) propagating to the top on both sides of the locked patch. Such transients are discussed in more detail in *Lapusta and Liu* (2009).

Note that most (more than 90%) of the seismic slip (and seismic moment) in our simulations is confined to the velocity-weakening patch. For example, for $r = 350$ m, which

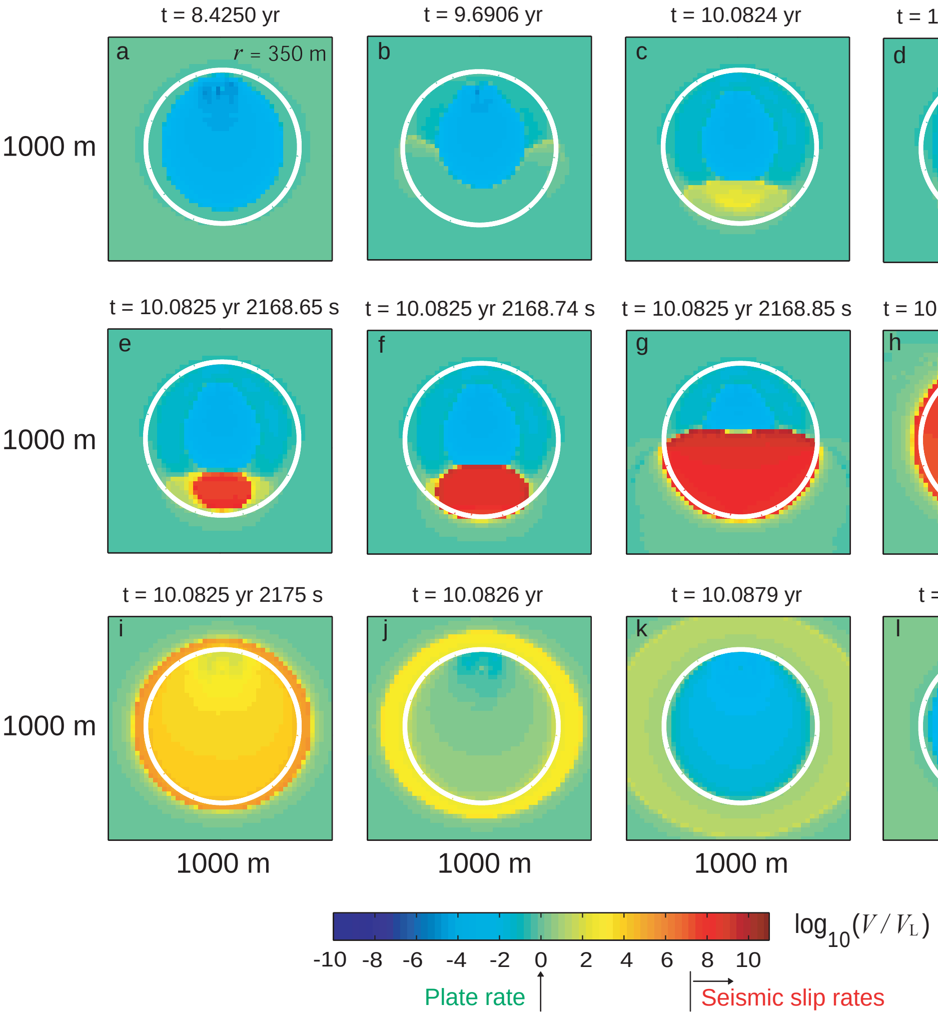

Figure 4.6. Snapshots of slip velocity distribution for one earthquake cycle and $r = 350$ m. Colors and markings have the same meaning as in figures 4.3 and 4.5. The simulated fault region is 2000 m × 2000 m; only a part of it is shown in each snapshot. Aseismic slip on the patch before the event is restricted to the annulus close to the edges of the patch. The middle part of the patch is locked when the seismic event begins. The seismic slip initiates at one end of the patch and propagates unidirectionally.

is the largest patch size we have simulated, 95% of seismic slip occurs on the patch. This is because we assume a sharp transition between the velocity-weakening patch and the velocity-strengthening surroundings, as would be appropriate for an inclusion of a velocity-weakening material in an otherwise velocity-strengthening fault, and the dynamic rupture arrests right after exiting the velocity-weakening patch. Other scenarios could be envisioned, such as a gradual change in rate and state properties, which might lead to more seismic slip outside the patch.

4.4 Simulated Scaling of Seismic Moment with Recurrence Time

To produce repeating earthquakes of different sizes, and hence to determine the scaling of seismic moment with the recurrence time in this model, we change the radius r of the velocity-weakening patch, keeping all other model parameters the same. The resulting scaling is plotted in figure 4.7a, for r between 88 and 350 m. The lines corresponding to the observed scaling (4.1) and the theoretical scaling (4.2) are shown for comparison. For the long-term slip velocity $V_{\mathrm{L}} = 23$ mm/a (*Nadeau and Johnson*, 1998), the model reproduces the right scaling exponent; the best fit (green line in figure 4.7a) to the simulated results (blue dots in figure 4.7a) gives $T \propto M_0^{0.19}$, very close to the observed $T \propto M_0^{0.17}$. However, this value of V_{L} results in smaller recurrence times than the observed ones. For $V_{\mathrm{L}} = 4.5$ mm/a (figure 4.7a, red dots), our model reproduces both the scaling and the absolute values of the observed recurrence times. The value $V_{\mathrm{L}} = 4.5$ mm/a is within the range of 4 to

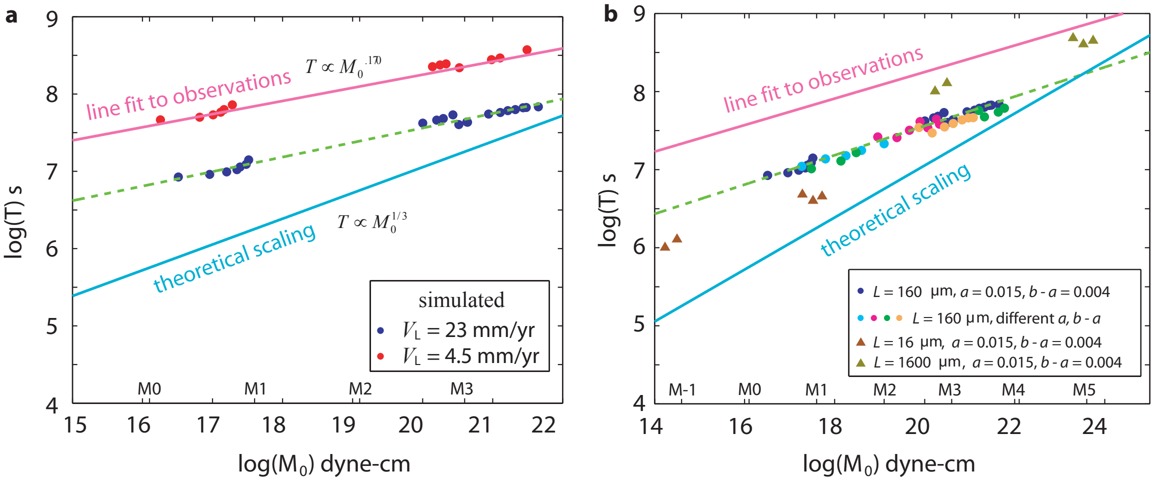

Figure 4.7. Scaling of seismic moment M_0 with recurrence time T for different patch radii r. (a) Simulation results for long-term slip velocities V_{L} of 23 mm/a and 4.5 mm/a are shown as blue and red dots, respectively. For each V_{L}, earthquakes of different sizes are obtained by varying the radius of the velocity-weakening patch; all other model parameters are the same. The line fit to observations (4.1) of *Nadeau and Johnson* (1998) and the scaling in the simple theoretical model (4.2) are indicated by the magenta and light blue lines, respectively. The best fit to simulations with $V_{\mathrm{L}} = 23$ mm/a is shown by the green dashed line. For both values of V_{L}, the observed scaling exponent is reproduced; the simulations with $V_{\mathrm{L}} = 4.5$ mm/a also fit the absolute values of the recurrence times. (b) Simulation results for $V_{\mathrm{L}} = 23$ mm/a, $L = 160$ μm, and several different combinations of rate and state parameters a and b all produce the same scaling, with events of all magnitudes between $M_{\mathrm{w}} = 0.3$ and $M_{\mathrm{w}} = 3.7$. $V_{\mathrm{L}} = 23$ mm/a was used for computational efficiency. Simulations for different values of L also reproduce the observed scaling exponent.

35 mm/a suggested for the portion of the San Andreas fault with repeating earthquakes (*Harris and Segall*, 1987).

The main difference between our simulations and the theoretical model leading to scaling (4.2) is the significant aseismic slip that occurs in our model on the velocity-weakening patch, as discussed in section 4.3 for several examples. The ratio of seismic moment M_0 to the total moment M_{total} released on the patch during one earthquake cycle, as a function of the total moment M_{total}, is shown in figure 4.8 for $V_{\mathrm{L}} = 23$ mm/a. The ratio varies from 0.001 for the case with the smallest simulated events ($r = 88$ m) to 0.8 for the case with

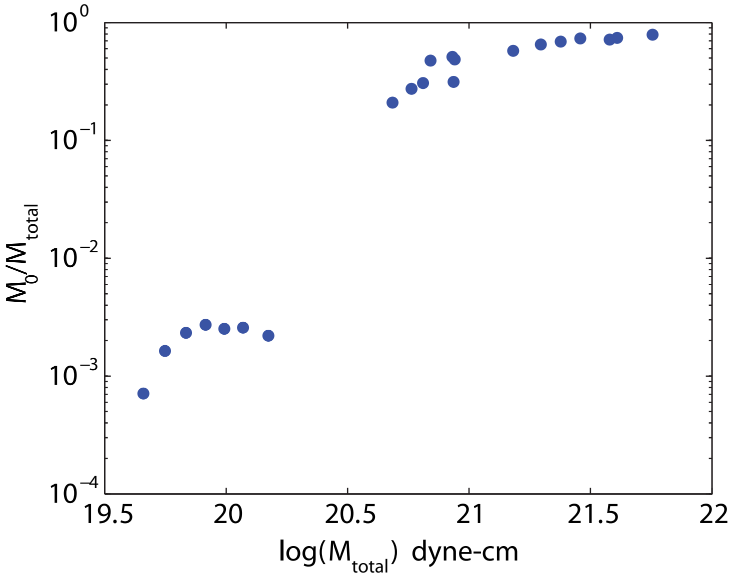

Figure 4.8. Ratio of seismic moment M_0 and total moment $M_{\rm total}$ released on the patch for one earthquake cycle as a function of total moment $M_{\rm total}$, for the simulations of figure 4.7 with $V_{\rm L} = 23$ mm/a. For all simulated cases, a significant portion of the total moment on the patch is released aseismically, from 0.999 to 0.2.

the largest simulated events ($r = 350$ m). Hence, even for the largest events in figures 4.7a and figure 4.8, a significant part, about 20%, of moment is released aseismically. Note that the results separate into two clusters (figures 4.7a, 4.8). The cluster with smaller seismic moments corresponds to simulations in which repeating earthquakes occupy only a portion of the patch size, occurring close to its center, as described in section 4.3.1. The cluster with larger seismic moments corresponds to simulations in which the repeating earthquakes occupy the entire patch, as described in section 4.3.2.

For a fixed set of friction properties, simulations with larger seismic moment, and hence with larger patches, generally correspond to larger proportions of seismic slip, with some scatter (figure 4.8). However, when friction properties vary from patch to patch, the correspondence between larger patches and larger ratio of seismic to total slip, in general, no longer holds even approximately. This is because the ratio of seismic to total moment at least in part depends on the relative size of the patch with respect to the critical patch size, and the critical patch size would, in general, be different for different sets of friction parameters. Hence a given patch can result in different ratios of seismic to total moment, depending on its friction properties.

The simulations reported so far have been done for a particular selection of rate and state parameters that are representative of laboratory results: $L = 160\ \mu\mathrm{m}$, $a = 0.015$ and $b - a = 0.004$ for the velocity-weakening patch, and $a = 0.019$ and $a - b = 0.004$ for the surrounding velocity-strengthening zone. To investigate how the behavior varies with friction parameters, we have explored a range of values for the rate and state parameters a and b, making the velocity-weakening parameter $(b - a)$ on the patch two times larger and two times smaller and studying a different value of a. Sets of a and $(b - a)$ on the velocity-weakening patch are: 0.015 and 0.004, 0.015 and 0.002, 0.015 and 0.008, 0.01 and 0.004, 0.01 and 0.002. In each case, the properties of the velocity-strengthening zone are assigned by switching the values of a and b. Remarkably, all of these simulations produce the same scaling of recurrence time with seismic moment, as shown in figure 4.7b, resulting in events of all sizes between moment magnitudes from 0.3 to 3.7 for the patch sizes we simulated. (Larger events can be obtained using larger patches.) Note that the long-term slip velocity of 23 mm/a was used for this exploration, because computations with that velocity require less computational resources; simulations with 4.5 mm/a should produce exactly the same qualitative result but with longer recurrence times, matching the simulated results with observations as in figure 4.7a.

For different values of the characteristic slip L, our model continues to reproduce the scaling exponent but the absolute values of seismic moment and recurrence time change as indicated in figure 4.7b. Note that a larger value of L results not only in larger recurrence times but also in larger velocity-weakening patches being able to slip aseismically, causing larger critical patch sizes and larger moments for the smallest earthquakes that can occur in the model. If L is increased from 160 to 1600 $\mu\mathrm{m}$, a value outside the range of L observed in the laboratory, the smallest seismic event that arises in the model has the moment magnitude 2.8, which is larger than the smallest repeating earthquakes observed in Parkfield. Hence increasing L in the model is not a productive way of increasing recurrence times.

The study of a range of rate and state parameters confirms the conclusion that the long-term slip velocity has to be smaller than 23 mm/a for the model, in its current form, to fit the absolute values of the recurrence times. However, it is possible that the model can be modified to match the recurrence times even for $V_{\mathrm{L}} = 23$ mm/a as discussed in section 4.6.

4.5 Simulated Source Parameters

The source dimensions of simulated repeating earthquakes of moment magnitudes 0.3 to 3.7 are in tens to hundreds of meters. We can find the (static) stress drop in the model by computing the difference in shear stresses before and after an event. For the simulation with $r = 124$ m (section 4.3.1, figure 4.3), the shear stress distribution before and after a dynamic event, and the resulting static stress drop, over a crosssection centered on the patch are shown in figure 4.9. The stress drop is highly variable over the source region, with the

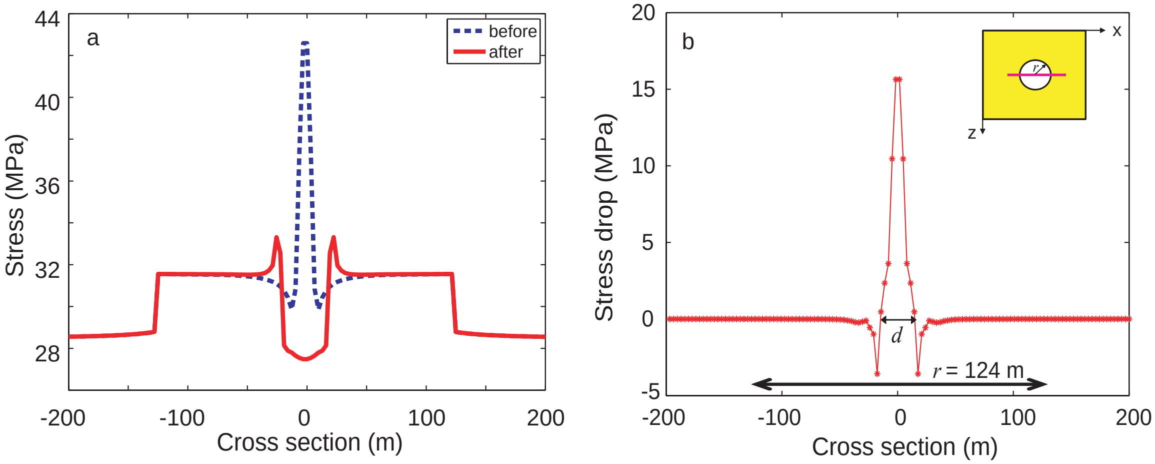

Figure 4.9. (a) Stress distribution along a crosssection of the model illustrated in the inset of (b), before (dashed line) and after (solid line) an event, for $r = 124$ m. (b) Static stress drop along the crosssection.

negative stress drop, i.e., stress increase, outside the area of seismic slip. The heterogeneous stress drop distribution is qualitatively consistent with a recent seismic study for a M_{w} 2.1 repeating sequence in Parkfield (*Dreger et al.*, 2007). For this and all other repeating earthquakes we simulated, the average stress drop over the area of positive stress drop is between 1 and 10 MPa (figure 4.10). The values of stress drops and seismic source dimensions in our model are within the range of typical seismic estimates for small earthquakes (*Abercrombie*, 1995), as shown in figure 4.11. The source parameters in our model are also consistent with inversions for the repeating earthquakes at Parkfield (*Imanishi et al.*, 2004; *Allmann and Shearer*, 2007).

4.6 Conclusions

We find that representative rate and state friction parameters combined with a mechanically realistic earthquake model reproduce well-documented properties of small repeating

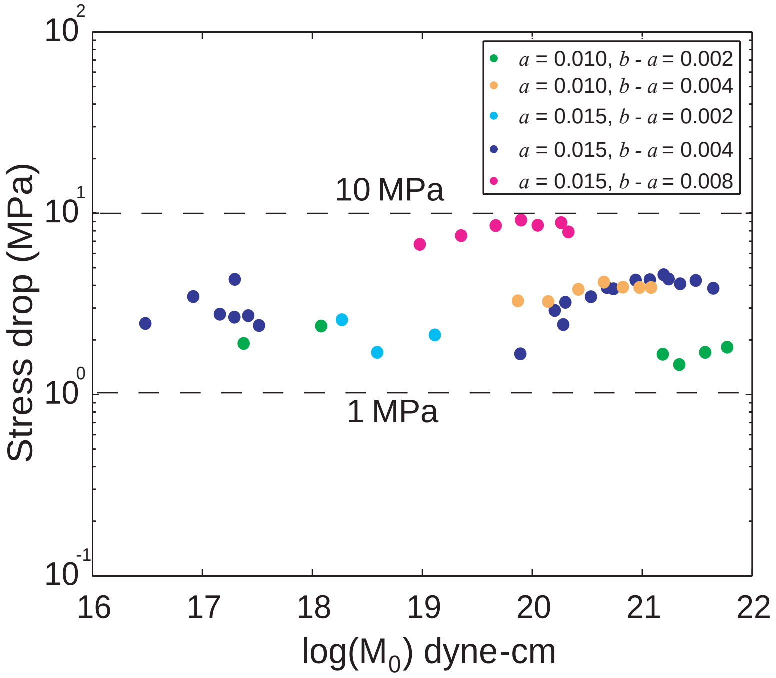

Figure 4.10. Stress drops averaged over the source (i.e., the area of positive stress drop) for all simulations with $L = 160$ µm. The stress drops are in the range 1–10 MPa of typical stress drops, consistently with recent inversions for small repeating earthquakes.

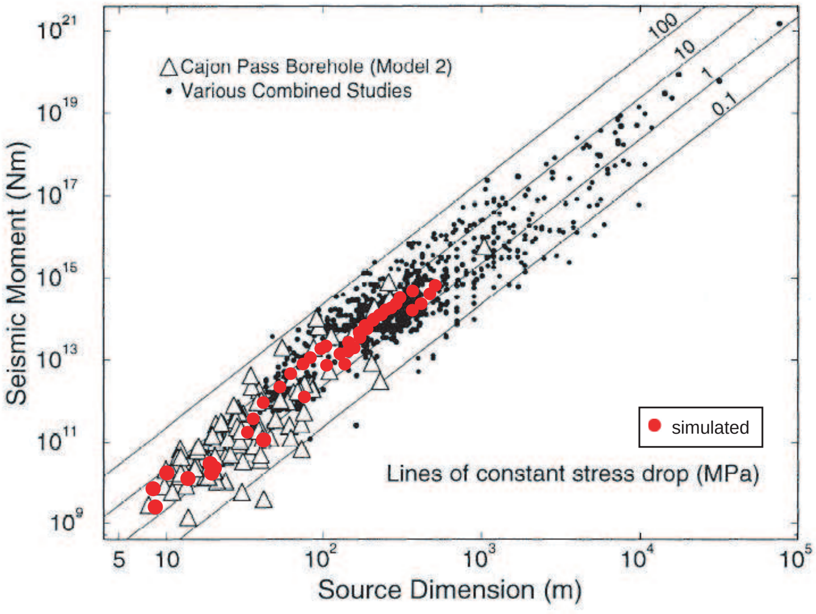

Figure 4.11. Values of seismic moment and source dimensions, calculated from our simulations with $L = 160$ µm, plotted on top of seismic estimates for small and medium earthquakes (*Abercrombie*, 1995). The source parameters in our simulations are consistent with the seismic observations.

earthquakes for reasonable values of the long-term slip velocity. The model incorporates all stages of slip development on faults and all inertial effects during seismic events. For the range of parameters studied, the simulations have produced repeating earthquakes with moment magnitudes from 0.3 to 3.7, and all of them follow the scaling (4.1) of the seismic moment with the recurrence time observed for small repeating earthquakes at Parkfield. At the same time, the simulated repeating earthquakes have source parameters that are similar to the ones inferred for repeating earthquakes at Parkfield and typical for small earthquakes in general. We find significant aseismic slip on the patch that also produces repeating earthquakes, ranging from more than 99% of total slip for the smallest repeating earthquakes that arise in our model (with moment magnitude 0.3) to 20% of total slip for the largest repeating earthquakes that we have simulated (moment magnitude 3.7). From stability properties of rate-and-state faults, it is clear that the smallest velocity-weakening patches capable of producing seismic slip would also have significant aseismic slip, since even smaller patches would be completely aseismic. That consideration, in fact, motivated the present study, which shows that significant aseismic slip persists over several earthquake magnitudes.

The success of the model in matching the observed scaling of repeating earthquakes while producing reasonable source parameters is, in fact, due to the occurrence of significant aseismic slip at the location of seismic events. Hence any factors that can affect the proportion of aseismic and seismic slip in the model need to be explored, such as state-variable evolution laws other than the aging formulation adopted in this study or additional weakening of frictional resistance during earthquakes due to shear heating. Note that the presence of the surrounding velocity-strengthening region is an important factor in inducing aseismic slip on the patch, since the slow slip from that region continuously penetrates into the patch due to stress concentrations at the boundary between slipping and locked areas. If that factor is a dominant one in inducing aseismic slip on the patch, then our model should produce qualitatively similar results with other rate and state formulations, especially if they retain properties of the "aging" law at near-plate slip velocities that govern the penetration of slow slip into the patch. Another important aspect to explore is the patch geometry. The streaklike nature of earthquake locations on creeping faults indicates that velocity-weakening fault materials may be present in stripes (W. Ellsworth, personal communication). Hence a model that obtains earthquakes of different magnitudes by considering rectangular patches of a fixed width and increasing aspect ratio would be an interesting alternative to the increasing circular patches considered in this work.

To match the absolute values of the observed recurrence times, our model requires a lower long-term slip rate, 4.5 mm/a, than the rate of 23 mm/a preferred in previous studies. The value $V_{\mathrm{L}} = 4.5$ mm/a is within the range of 4 to 35 mm/a suggested for the portion of the San Andreas fault with repeating earthquakes (*Harris and Segall*, 1987). Since repeating earthquakes occur in the transition region next to the partially locked segment that produces occasional Mw 6.0 Parkfield earthquakes, it is indeed possible that the local slip rate there is lower than the overall long-term rate of the creeping segment. Our model supports such lower slip rate. The discrepancy in the accumulated slip may be accounted for by penetration of seismic slip or afterslip. Another factor that would promote smaller creeping rates is additional shielding due to more local locked asperities that are larger than the observed repeating earthquakes, as proposed by *Sammis and Rice* (2001). Hence it is important to understand how our model would combine with the ideas of *Sammis and Rice* (2001). At the same time, it is possible that modifications in the considered friction law (a significantly different parameter regime, inclusion of inelastic dilatancy or strong dynamic weakening) might preserve the simulated scaling but lengthen the recurrence time, allowing our model to match the absolute values of the observed recurrence times with higher values of long-term slip rate closer to 23 mm/a.

The study underscores the importance of properly accounting for interaction of seismic and aseismic slip in earthquake models. Recent observations suggest that similar interaction occurs on larger spatial scales, with aseismic slip transients and seismic tremor discovered on several seismogenic faults (*Kao et al.*, 2005; *Shelly et al.*, 2006; *Schwartz and Rokosky*, 2007). Models conceptually similar to the one presented in this work but with more complex distributions of velocity-weakening and velocity-strengthening regions may be able to explain a wide range of seismic and aseismic slip patterns observed.

Chapter 5

On Behavior of Small Repeating Earthquakes in Rate and State Fault Models

5.1 Introduction

Repeating earthquakes occur in the same location, and presumably rupture the same patch of the fault in a similar way, to produce nearly identical seismic signals. The short recurrence times and known locations of small repeating earthquakes enable abundant and detailed seismic observations (e.g., *Vidale et al.*, 1994; *Nadeau and Johnson*, 1998; *Igarashi et al.*, 2003), and thus provide an excellent opportunity to study the earthquake source and fault properties. Studies of repeating earthquakes have been used to investigate an increasingly richer array of problems, including fault creeping velocities, postseismic slip, earthquake interaction, and stress drops (*Vidale et al.*, 1994; *Nadeau and Johnson*, 1998; *Schaff et al.*, 1998; *Peng et al.*, 2005; *Chen et al.*, 2007; *Dreger et al.*, 2007; *Chen et al.*, 2010).

One of the most interesting observations about small repeating earthquakes is the scaling between the recurrence time T and seismic moment M_0 as $T \propto M_0^{0.17}$ (*Nadeau and*

Johnson, 1998; *Chen et al.*, 2007). This observed scaling is different from that of a simple conceptual model with circular ruptures, constant stress drop, and seismic slip equal to plate velocity times recurrence time, which would result in a relationship of $T \propto M_0^{1/3}$. Various explanations for this discrepancy have been proposed: the magnitude dependence of stress drops (*Nadeau and Johnson*, 1998), location of small repeating earthquakes at the boundary between much larger creeping and locked regions (*Sammis and Rice*, 2001), and partial aseismic slip due to strain hardening friction (*Beeler et al.*, 2001).

In chapter 4, we conducted fully dynamic simulations of small repeating earthquakes in a model with a small circular patch governed by rate-and-state velocity-weakening friction surrounded by a much larger velocity-strengthening region. The model results in repeating earthquakes with typical stress drops and sizes comparable with observations, and reproduces the observed scaling between seismic moment and the recurrence time. We attribute the simulated scaling to the fact that the seismic to aseismic slip ratio increases with the seismic moment.

The model in chapter 4 has also been used to study the postseismic response of small repeating earthquakes to a nearby large event (*Chen et al.*, 2010). By varying the loading velocity to simulate the postseismic creep effect, the model successfully explains the observed temporal variation in seismic moment and recurrence time of small repeating earthquakes near Parkfield after the 2004 M6 Parkfield earthquake.

Why the model in chapter 4 is able to match the observed scaling between the recurrence time and seismic moment and what elements in their model are most important merit further study. Here we investigate the behavior of small repeating earthquakes on a rate and state fault under different scenarios, explore the importance of different model ingredients, and propose a theoretical model to understand the simulated results in terms of the scaling between the recurrence time and seismic moment.

5.2 Model for Small Repeating Earthquakes

Our model for small repeating earthquakes is based on the one in chapter 4 (figure 5.1). We simulate earthquakes on a fault governed by laboratory-derived rate and state friction laws (*Dieterich*, 1979, 1981; *Ruina*, 1983; *Marone*, 1998; *Dieterich*, 2007, and references therein). Rate and state friction laws have been successfully applied to modeling of various fault slip phenomena (*Dieterich*, 2007, and references therein). For constant in time normal stress σ, shear resistance τ obeying rate and state friction laws is written as:

$$\tau = \sigma[f_0 + a\ln(V/V_0) + b\ln(V_0\theta/L)], \tag{5.1}$$

$$\tau_{ss} = \sigma[f_0 + (a-b)\ln(V/V_0)], \tag{5.2}$$

where V is slip velocity, θ is a state variable, L is the characteristic slip distance, a and b are rate-and-state parameters, V_0 and f_0 are the reference slip velocity and friction coefficient respectively, and τ_{ss} is steady-state shear resistance. Different forms of the state evolution equation have been proposed based on laboratory experiments (e.g., *Ruina*, 1983; *Kato and Tullis*, 2001; *Dieterich*, 2007). Which formulation best represents laboratory experiments is a question of active studies (*Bayart et al.*, 2006). Here we investigate models with the following forms:

$$d\theta/dt = 1 - V\theta/L \quad \text{(the aging form)}, \tag{5.3}$$

$$d\theta/dt = -V\theta/L \ln(V\theta/L) \quad \text{(the slip form)}, \tag{5.4}$$

$$d\theta/dt = \exp(-V/V_c) - V\theta/L \ln(V\theta/L) \quad \text{(the composite form)}, \tag{5.5}$$

and

$$d\theta/dt = \begin{cases} 1 - V\theta/L, & \text{when } V\theta/L < 1, \\ -V\theta/L \ln(V\theta/L), & \text{when } V\theta/L \geq 1 \quad \text{(the combined form).} \end{cases} \tag{5.6}$$

The form (5.6) was proposed by Rubin (personal communication).

We refer to the fault regions with $a-b > 0$ as being velocity strengthening, and $a-b < 0$ as being velocity weakening. Velocity-strengthening fault regions tend to stably slip (creep) under loading, and velocity-weakening fault regions are able to produce seismic events when they are larger than the nucleation zone size $2h^*$ (*Rice and Ruina*, 1983; *Dieterich*, 1992; *Rice*, 1993; *Rubin and Ampuero*, 2005). Estimates for the nucleation half-length h^* with different dependence on b and $(b-a)$ have been proposed. We denote them as h^*_b, h^*_{b-a} and h^*_{RA} in reference to quantities introduced by *Dieterich* (1992), *Rice* (1993) and *Rubin and Ampuero* (2005) respectively:

$$h^*_b = \frac{\hat{\mu} L}{\sigma b}, \tag{5.7}$$

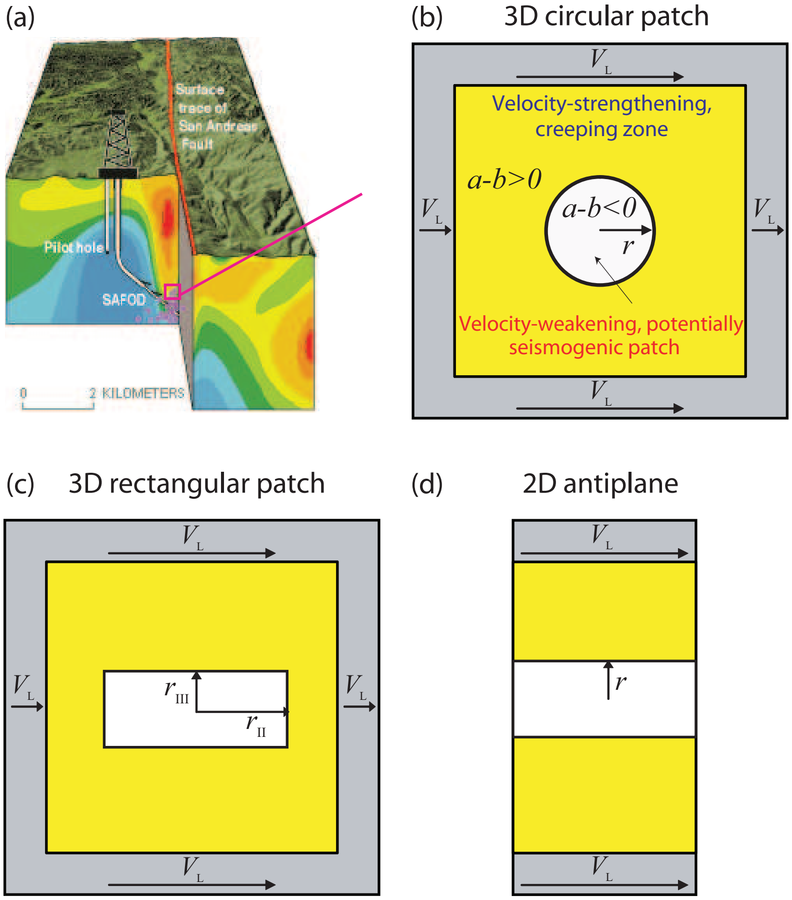

Figure 5.1. Schematics of the models. To simulate repeating earthquakes, such as (a) the target events of SAFOD drilling project (image courtesy of U. S. Geological Survey), we consider a small segment of the fault embedded into an elastic medium and governed by rate and state friction laws. On the fault, a velocity-weakening, potentially seismogenic, patch is surrounded by a creeping, velocity-strengthening zone. 3D models with a (b) circular patch, (c) rectangular patch, and (d) a 2D antiplane model are studied.

$$h^*_{b-a} = \frac{\hat{\mu} L}{\pi \sigma (b-a)}, \tag{5.8}$$

$$h^*_{\mathrm{RA}} = \frac{\hat{\mu} L b}{\pi \sigma (b-a)^2}, \tag{5.9}$$

where $\hat{\mu} = \mu$ for antiplane sliding and $\hat{\mu} = \mu/(1-\nu)$ for inplane sliding with ν being the Poisson's ratio. The 3D analog of h^*_{RA}, which is larger than that in equation (5.9) for 2D antiplane case by a factor of $\pi^2/4$ (Allen Rubin, personal communication), is in agreement with numerical simulations with the aging form of state-variable evolutions (chapter 4).

In our model, a planar fault is embedded in an elastic medium with the following properties: shear modulus $\mu = 30$ GPa, Poisson's ratio $\nu = 0.25$, shear wave speed $c_s = 3$ km/s. On the fault, a potentially seismogenic patch is surrounded by a larger creeping zone. The patch has velocity-weakening properties, $a - b < 0$, and the surrounding region has velocity-strengthening properties, $a - b > 0$. The similar model setup has also been used in other studies (e.g., *Kato*, 2012). The values of a and b of the velocity-strengthening region is set to be equal to the values of b and a of the velocity-weakening region, respectively; thus we only mention the values of a and b in the velocity-weakening region in the following. Long-term slip velocity V_{L} is imposed outside the velocity-strengthening zone to model steady creep of the surrounding fault area. The spontaneous slip history of the fault is solved using the methodology of *Lapusta and Liu* (2009), which can fully resolve all aspects of seismic and aseismic behavior. In our simulations, we use the following values from chapter 4: effective normal stress $\sigma = 50$ MPa, reference friction coefficient $f_0 = 0.6$, reference slip velocity $V_0 = 1$ µm/s, characteristic slip $L = 160$ µm, and loading velocity $V_{\mathrm{L}} = 23$ mm/a (*Nadeau and Johnson*, 1998). We define seismic slip as the slip accumulated with slip velocities larger than 0.1 m/s.

5.3 Response of Models with Different State Evolution Laws

In chapter 4, we used the aging form in the simulations of small repeating earthquakes. Here we study the effect of other state evolution forms (equations (5.4)-(5.6)) on the behavior of small repeating earthquakes.

Let us first consider the response of models with the slip form. We set $a = 0.015$ and $b = 0.023$, and obtain different magnitudes of repeating earthquakes by varying the velocity-weakening patch radius r. We choose $(b - a)$ of 0.008, which is larger than the typical value of 0.004 as used in chapter 4, because the nucleation half-length is smaller for larger $(b - a)$ and thus it is easier to study a larger range of r/h^*. In chapter 4, the simulated range of r/h^* is about 1 to 4 for $a = 0.015$, $b - a = 0.004$. Here we extend the range of r/h^* to about 1 to 11. The simulated earthquakes show a similar exponent of the scaling between the recurrence time and seismic moment to that with the aging form (figure 5.2). The absolute value of the simulated recurrence time is lower than the observations. As shown in chapter 4, we can match the absolute values of the observed recurrence time while maintaining the scaling exponent by using $V_L = 4.5$ mm/a instead of $V_L = 23$ mm/a. Here, we use 23 mm/a for numerical convenience (faster loading results in shorter interseismic time).

We also study different sets of parameters a and b. In general, the simulated overall scaling of recurrence time and seismic moment with different parameters a, b is similar to the simulated scaling with the aging form, which is flatter than the theoretical scaling

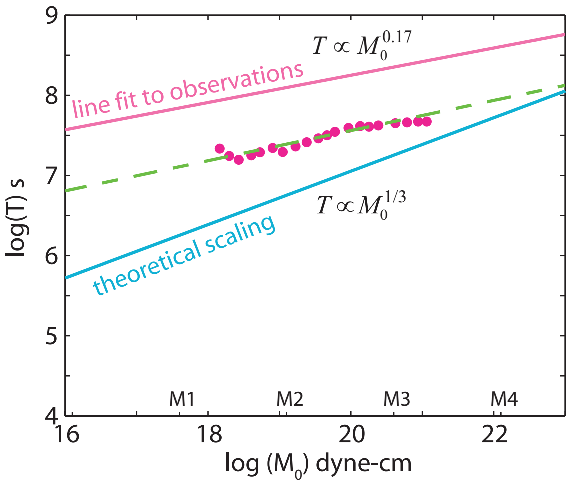

Figure 5.2. Simulated scaling of the recurrence time T with seismic moment M_0 for the slip form with different patch radii ($b = 0.023$, $b - a = 0.008$). The simulated scaling with the slip form in this study (dots) is similar to that with the aging form (green dashed line, from chapter 4). The simulated scaling exponent is similar to the observations (magenta line, from *Nadeau and Johnson* (1998)), and different from the prediction of a simple theoretical model with constant stress drop and no aseismic slip (blue line). The results for $V_{\mathrm{L}} = 23$ mm/a are plotted; as shown in chapter 4, our simulations can match observations for $V_{\mathrm{L}} = 4.5$ mm/a.

$T \propto M_0^{1/3}$ (figure 5.3b). The individual scalings for different sets of parameters a and b, however, seem to show some difference. In particular, simulation results with smaller $(b - a)$ of 0.002 and 0.004, especially with $(b - a)$ of 0.002, show steeper scaling than the observed one. This is likely due to the fact that for $(b - a)$ of 0.002 and 0.004, only relatively small patch sizes relative to the nucleation length are studied due to computational limitation. The simulated range of r/h^* for $(b-a)$ of 0.002, 0.004, 0.008, and 0.02 is about 1 to 3, 1 to 6, 1 to 11, and 1 to 17, respectively. As discussed in section 5.8, the scaling between the recurrence time and seismic moment is predicted (theoretically) to be steeper for relatively small ratios of the patch size to nucleation size. Note that, for the same $(b-a)$, the simulated recurrence time and seismic moment are almost the same. The absolute level of recurrence time increases with larger $(b - a)$. For the sets of parameters a, b we studied, the absolute levels of recurrence time for simulations with the slip form (figure 5.3b) show larger variations than that with the aging form (figure 5.3a).

We have also studied the combined form (figure 5.3c) and composite form (figure 5.3d). The simulated overall scaling for both the combined form and composite form are similar to that with the aging and slip form. The scaling for smaller $(b-a)$ is steeper than the observed one due to limited simulated range of r/h^*. The magnitudes of the simulated smallest events for different values of a and b with the combined form are about the same as those with the slip form, while the simulated events with the composite form are generally smaller than that with the slip form. This is because the nucleation length for the composite form is generally smaller than that for the slip form or combined form as discussed in section 5.7, and thus the patch sizes needed to produce seismic events are generally smaller, resulting in smaller seismic moments.

Note that for the aging form (figure 5.3a), the resulting T and M_0 cluster around a single line. For the other forms (figure 5.3b-d), the simulations for individual a and b combinations displace with respect to each other. For the slip, combined and composite forms, the simulated levels of T vs. M_0 seem to depend only on $(b-a)$.

Simulations with the aging form produce earthquakes that rupture only a small central portion of the velocity-weakening patch when the patch size is comparable to the nucleation size and $(b-a)$ is relatively small (0.002 and 0.004) (chapter 4). This type of event has been proposed to explain the increased seismic moment with decreased recurrence time observed for postseismic response of small repeating earthquakes to 2004 M6 Parkfiled earthquake (*Chen et al.*, 2010). Simulations with the slip form, combined form, or composite

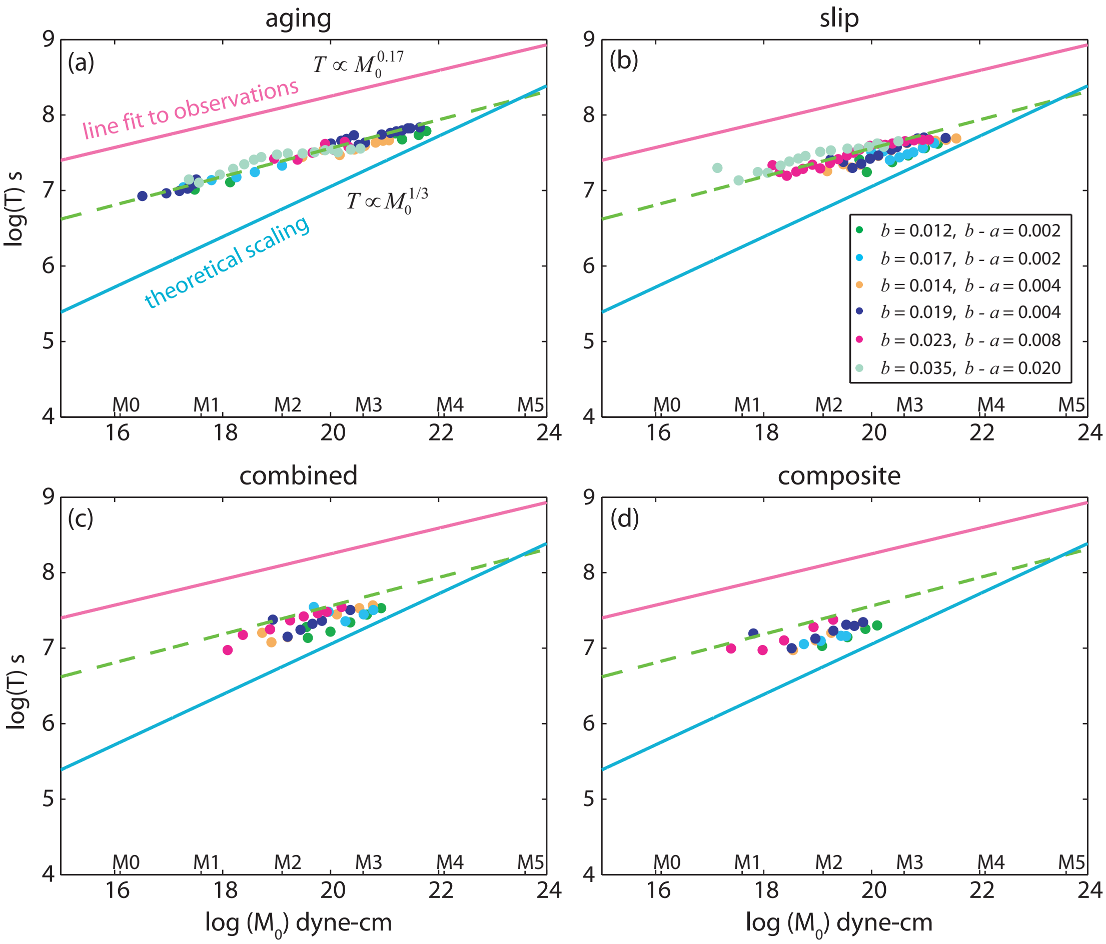

Figure 5.3. Simulated scaling of the recurrence time with seismic moment for different state evolution forms: (a) aging form (mostly adapted from chapter 4, except for the simulations with $a = 0.015$, $b = 0.035$), (b) slip form, (c) combined form, and (d) composite form. Different colors represent simulations with different a and b. The overall scaling exponents with the four different state evolution forms are all similar to the observations. Some individual scalings with certain a and b, for example, $b - a = 0.002$ and $b - a = 0.004$ for the slip form, combined form, and composite form, seem to have larger exponents. This is because for these a and b, only relatively small patch sizes are studied due to computational limitations. Please see the text for more discussion. The lines have the same meaning as in figure 5.2.

form, however, do not commonly produce events of this kind; the simulated patch behavior sharply switches from being totally aseismic to rupturing the whole velocity-weakening patch. Yet it is possible that events that rupture only a part of the patch can be obtained with the slip, combined, and composite forms, if the model includes heterogeneous patches or patches with a constitutive response that incorporates a stabilizing factor such as dilatancy (e.g., *Segall and Rice*, 1995).

5.4 Circular vs. Rectangular Patch

In chapter 4, the potentially seismogenic velocity-weakening region is assumed to be circular. Here we consider the effect of a rectangular geometry, using the other parameters from the model in chapter 4: the aging form of state evolution equation, $a = 0.015$ and $b = 0.019$ for the velocity-weakening region, and $a = 0.019$, $b = 0.015$ for the velocity-strengthening region. The resulting 3D estimate of the half nucleation size h^*_{RA} is about 90 m. In the rest of the section, we use h^* to denote the 3D estimate of h^*_{RA} for simplicity. The rectangular velocity-weakening region has dimensions of $2r_{\mathrm{II}}$ and $2r_{\mathrm{III}}$ in the mode II and mode III directions, respectively (figure 5.1c). We study cases with different patch half-widths r_{III} of 40, 50, 60, 70, 80, 100, and 130 m, corresponding to r_{III}/h^* of 0.4, 0.6, 0.7 0.8, 0.9, 1.1 and 1.4, respectively. For each r_{III}, we obtain different sizes of earthquakes by changing r_{II}.

The simulated scaling between the recurrence time and seismic moment with the rectangular patch (figure 5.4a) is similar to the results with a circular patch. We observe four types of slip patterns (figure 5.4b, 5.5-5.7): periodic aseismic; seismic pattern I in which seismic events rupture only a part of the velocity-weakening patch and result in small magnitudes (figure 5.5); seismic pattern II in which seismic events rupture the whole velocity-weakening patch and have much larger magnitudes (figure 5.6); and noncharacteristic in which different slip patterns occur in one sequence, and not in a repeating way (figure 5.7). As expected, events are more seismic when the patch size is larger. Seismic events of pattern I have also been observed with a circular patch (chapter 4). Note that if both r_{II} and r_{III} are large enough compared with the nucleation half-length, seismic ruptures tend to start at one side of the patch while the center of the patch is still locked (figure 5.6b). If r_{III} is a little smaller than the nucleation half-length, even though r_{II} is much larger than the nucleation half-length, aseismic slip creeps all the way into the center of the patch, and seismic ruptures start from the center (figure 5.6a). The noncharacteristic pattern could be nonperiodic seismic or nonperiodic aseismic depending on the patch dimensions.

Our studies show that the width and length of a velocity-weakening patch do compensate each other to some extent in terms of nucleation. The required size of r_{II} to produce seismic event is smaller for larger r_{III}. However, this is only valid for a certain range of r_{III}/h^*. For r_{III} small compared with the nucleation length ($r_{\mathrm{III}}/h^* \lessapprox 0.4$), no seismic events are observed. Seismic events that rupture the whole velocity-weakening patch are only obtained for r_{III} close to or larger than the nucleation length ($r_{\mathrm{III}}/h^* \gtrapprox 0.9$). Noncharacteristic slip patterns are observed when r_{III}/h^* is smaller than 1 and r_{II}/h^* is large enough. We also expect nonrepeating patterns when both r_{III}/h^* and r_{II}/h^* are large enough. This is because when one or both of the dimensions of the velocity-weakening patch get large compared with the nucleation length, more freedom exists for nucleation

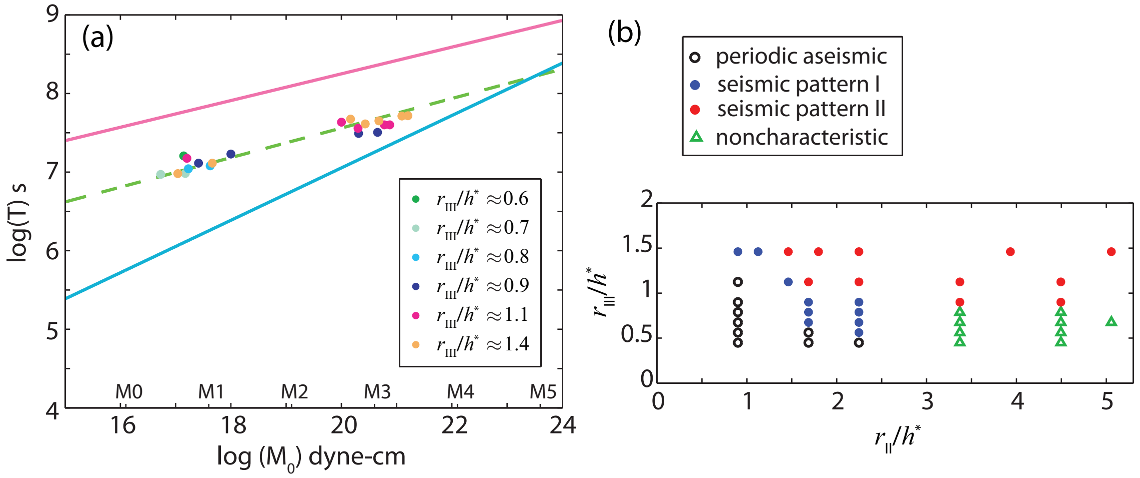

Figure 5.4. (a) Scaling of the recurrence time with seismic moment for simulations with a rectangular velocity-weakening patch. The aging form is used ($a = 0.015$, $b = 0.019$). h^* stands for the 3D analog of h^*_{RA}. Different colors represent simulations with different half widths r_{III} of the patch. For the same half width of the patch, the half length of the patch (r_{II}) is varied to produce different sizes of events. The resulting overall scaling is similar to that with a circular patch. The lines have the same meaning as in figure 5.2. (b) Different slip patterns for different sizes of the rectangular patch. Note that the rectangular patch with r_{III}/h^* smaller than 1 is still able to produce seismic events for a certain range of r_{II}/h^*.

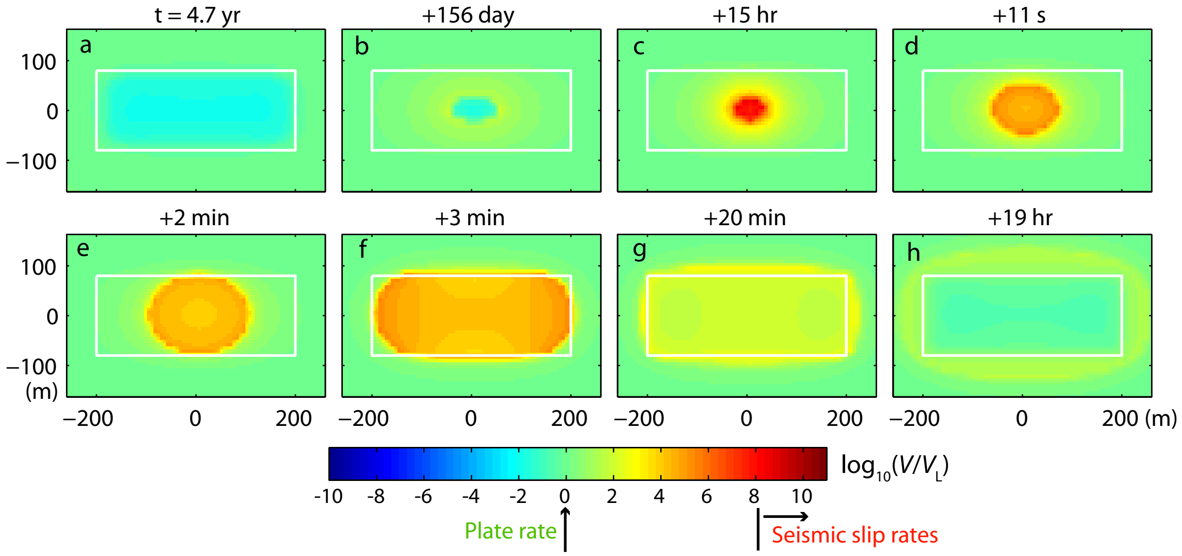

Figure 5.5. Example of an event of seismic pattern I with a rectangular patch ($r_{\mathrm{III}}/h^* = 0.9$, $r_{\mathrm{II}}/h^* = 2.2$). Panels show snapshots of slip velocity distribution for one cycle, with the time between each snapshot indicated on top of the panels. The seismic slip (shown as red) only ruptures part of the velocity-weakening patch. The patch is indicated by a white box.

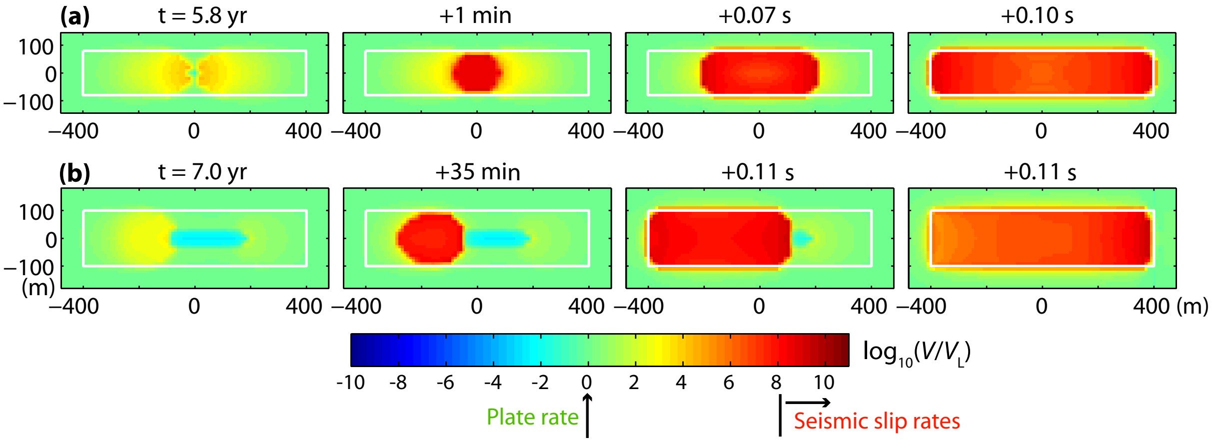

Figure 5.6. Example of an event of seismic pattern II with a rectangular patch. (a) $r_{\text{III}}/h^* = 0.9$, $r_{\text{II}}/h^* = 4.4$. (b) $r_{\text{III}}/h^* = 1.1$, $r_{\text{II}}/h^* = 4.4$. Snapshots of slip velocity distribution for one cycle with the time between each snapshot are shown. The seismic event ruptures the whole velocity-weakening patch.

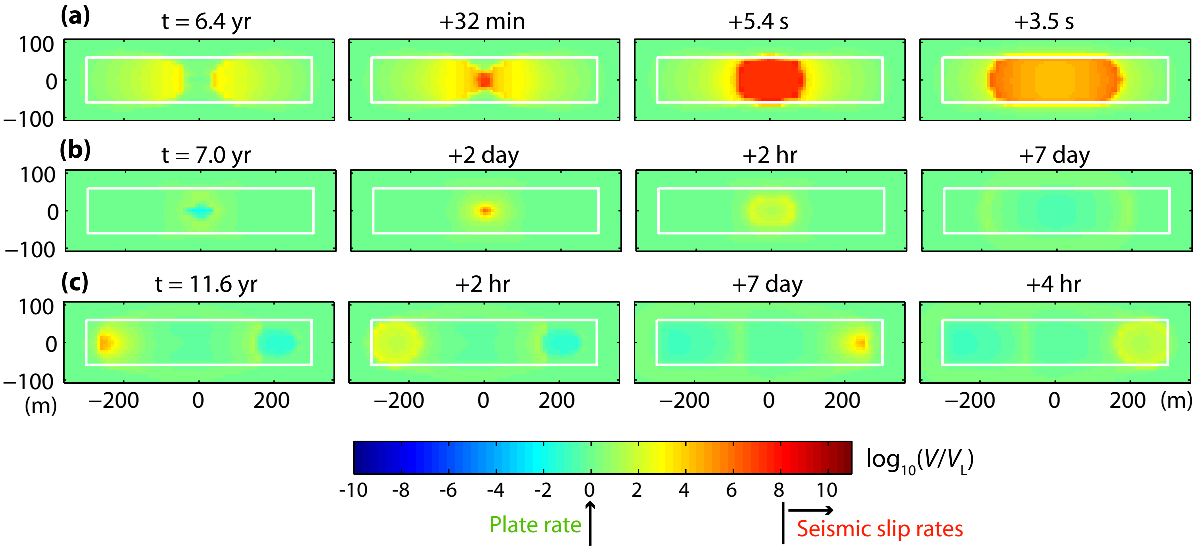

Figure 5.7. Example of noncharacteristic event sequences with a rectangular patch ($r_{\text{III}}/h^* = 0.7$, $r_{\text{II}}/h^* = 3.3$): (a) a seismic event; (b) aseismic-slip event symmetric with respect to the center of the patch; (c) aseismic-slip event that starts at one end.

processes, resulting in different slip patterns in one sequence.

Based on the simulations we have done, we expect that the results would stay qualitatively similar if the values of r_{II} and r_{III} were switched. For example, since $r_{\mathrm{II}}/h^* \approx 5$ and $r_{\mathrm{III}}/h^* \approx 0.7$ results in noncharacteristic events, we expect $r_{\mathrm{II}}/h^* \approx 0.7$ and $r_{\mathrm{III}}/h^* \approx 5$ to do the same. So all our conclusions should hold with r_{II} and r_{III} reversed.

5.5 Quasi-Dynamic vs. Fully Dynamic Simulations

Quasi-dynamic approach has been widely used in earthquake simulation studies (e.g., *Hori et al.*, 2004; *Kato*, 2004). Compared with the fully dynamic approach, quasi-dynamic approach ignores wave-mediated stress transfers, with computations becoming much simplified and less expensive. Here we compare fully dynamic simulations with quasi-dynamic simulations, with the same model as in chapter 4.

Results with quasi-dynamic simulations and fully dynamic simulations show similar scaling between the recurrence time and seismic moment (figure 5.8). However, differences do exist in terms of the recurrence time, seismic moment, effective rupture size, and maximum slip rate on the fault (figure 5.9). The 3D analog of the nucleation half-length h^*_{RA} in these simulations is about 90 m. The patch radii r of 106 and 124 m produce seismic pattern I slip that ruptures only a part of the patch, and r of 150, 200, and 300 m produce seismic pattern II slip that ruptures the whole velocity-weakening patch. The ratio of the maximum slip rate on the fault in fully dynamic and quasi-dynamic simulations increases with patch radius, and can be as high as 6 for $r = 300$ m. The effective rupture size, defined as the radius of the seismically ruptured area, is larger for fully dynamic

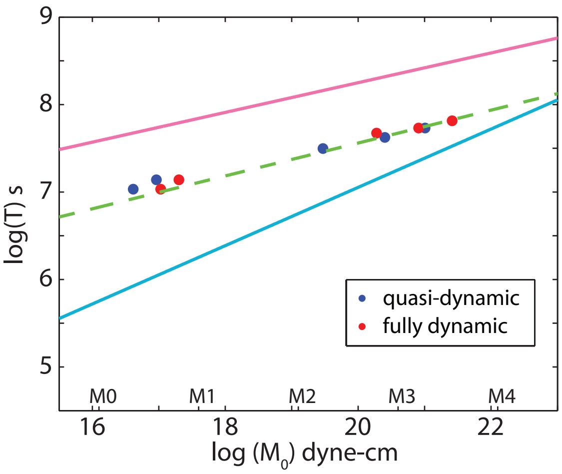

Figure 5.8. Recurrence time vs. seismic moment for quasi-dynamic and fully dynamic simulations (aging form with $a = 0.015$, $b = 0.019$). The two approaches show similar scalings. The lines have the same meaning as in figure 5.2.

simulations, especially for seismic pattern I events. Larger slip rates and effective rupture sizes for fully dynamic simulations result in larger seismic moments and longer recurrence times than those of quasi-dynamic simulations for seismic pattern II events. For seismic pattern I events, the seismic moment of fully dynamic simulations is also higher than that of quasi-dynamic simulations, but the recurrence times are about the same, because seismic slip only contributes a very small part of the total slip in these cases.

Note that the rupture pattern for the two simulation approaches can be quite different. In the example shown in figure 5.10, fully dynamic simulations produce creep events (with slip velocity that does not reach the seismic limit of 0.1 m/s) between large seismic event, while quasi-dynamic simulations do not show such creep events.

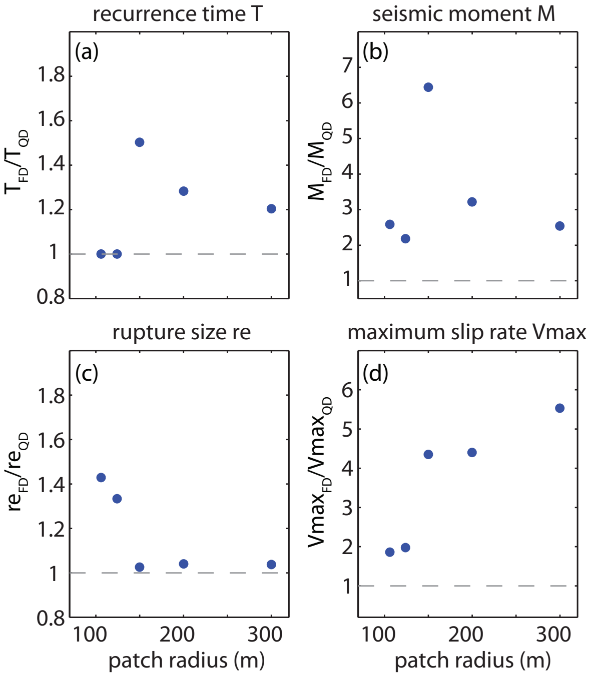

Figure 5.9. Ratios of results in fully dynamic (FD) simulations and quasi-dynamic (QD) simulations as functions of the patch radius, for (a) the recurrence time, (b) seismic moment, (c) effective rupture radius, and (d) maximum slip rate.

5.6 2D vs. 3D Simulations

2D simulations require much less computation than 3D simulations. So it is important to see if we can obtain the same scaling in 2D simulations as in 3D ones. We study an antiplane (mode III) 2D case. The velocity-weakening patch turns into an infinite strip with width $2r$ (figure 5.1d). The aging form of the state evolution equation is adopted, with the same parameters as in the 3D simulations of chapter 4.

Since the fault area is infinite in 2D, the computation of seismic moment is not straightforward. We use two approaches. One is computing the seismic moment per unit length of the fault. The other one is interpreting 2D simulation results in terms of a 3D problem as in *Lapusta and Rice* (2003). The first approach results in a different scaling between the recurrence time and seismic moment from that of observation (figure 5.11a). If we use

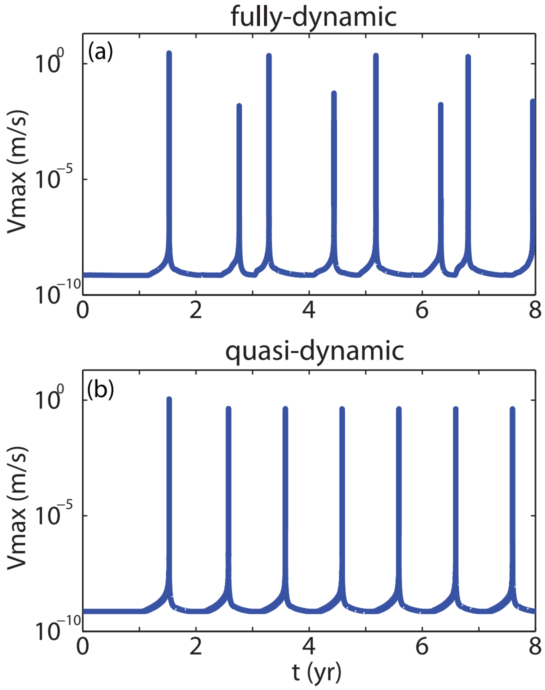

Figure 5.10. The maximum slip velocity on the fault as a function of time for (a) fully dynamic and (b) quasi-dynamic simulations. This example is for the aging form with $a = 0.015$, $b = 0.019$, and $r = 150$ m. Quasi-dynamic simulations result in lower maximum slip velocity than fully dynamic simulations. The slip patterns can also be different for these two simulation approaches. In this example, the fully dynamic simulation has creep events between seismic events, but these creep events do not occur in the quasi-dynamic simulation. As a result, the recurrence time of seismic events in the fully dynamic simulation is almost twice larger.

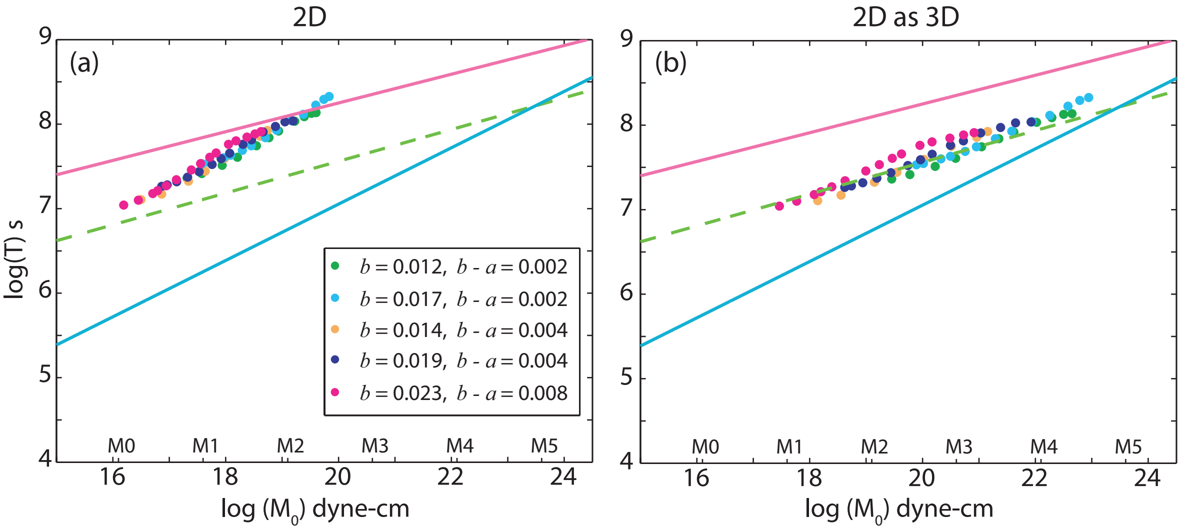

Figure 5.11. Simulations with a 2D antiplane model (with the aging form). (a) If seismic moment is computed per unit length of the fault in 2D, the scaling is quite different from that with the 3D model and from the observed one. (b) When the results of 2D simulations are interpreted in terms of a 3D problem, the scaling is similar to that of the 3D model. The lines have the same meaning as in figure 5.2.

the second approach, the scaling becomes similar to the one in the 3D simulation results (figure 5.11b).

Note that, unlike simulations with the 3D model, simulations with the 2D model do not produce seismic pattern I events that rupture only a part of the velocity-weakening patch, even though both 2D and 3D simulations use the aging form. This means that fault geometry affects the rupture pattern.

5.7 Simulated Nucleation Processes

In this work, we have conducted simulations in both 2D and 3D models, and studied different forms of the state evolution law. Here we compare nucleation properties obtained in different simulations. Only fully dynamic simulations with a circular patch are considered.

One of the important characteristics of the earthquake initiation is the nucleation size, i.e., the size of the zone slipping on the fault right before the seismic (wave-emitting) event. In our simulations, continuous slip in the velocity-strengthening region creates stress concentration inside the velocity-weakening patch, inducing aseismic slip there (e.g., figure 5.5-5.7). This band of aseismic slip initiates at the boundaries of the patch and widens with time, spreading over the entire patch for sufficiently small patch radii r. As shown in chapter 4, small enough patches remain completely aseismic. For each combination of model parameters, there is a critical patch size that starts producing seismic events (defined as slip with slip rate of 0.1 m/s or larger). It is natural to regard this critical patch size, which we denote by r_{nuc}, as a measure of the nucleation half-size (the entire size being the diameter of the patch $2r_{\mathrm{nuc}}$). In the following, we show that r_{nuc} is indeed relevant for describing the nucleation behavior of larger patches. The values of r_{nuc} in simulations with different forms of the state evolution law and different values of a and b are shown in figure 5.12. For the range of a and b studied, r_{nuc} for 2D simulations are smaller than those for 3D simulations with the same state evolution law. As expected based on prior studies (*Rubin and Ampuero*, 2005; *Ampuero and Rubin*, 2008), the aging form results in the largest values of r_{nuc}, followed by the slip and combined forms with similar r_{nuc}, and the composite form, which results in the smallest r_{nuc} among all 3D simulations. The values of r_{nuc} is generally smaller for larger values of $(b - a)$.

If r_{nuc} is indeed representative of the nucleation half-size in models with larger patches, then we would anticipate that, for patch radii $1 \leq r/r_{\mathrm{nuc}} \lessapprox 2$, the aseismic slip on the patch penetrates all the way to the center of the patch before seismic events nucleate, while for

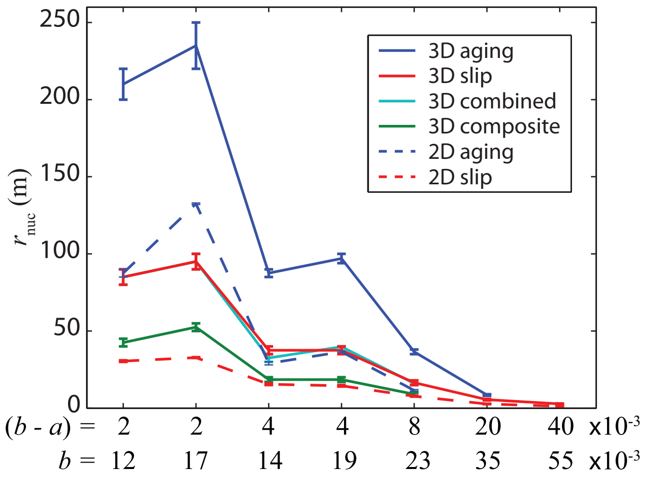

Figure 5.12. The smallest patch radius r_{nuc} that produces seismic events in the simulations with different sets of parameters a, b, and with different state evolution laws. Since the simulations are done with finite increments of patch radius, r_{nuc} is within the range indicated by the error bar, of which the lower end shows the largest simulated r that does not produce seismic events, and the upper end shows the smallest simulated r that does produce seismic events. Note that r_{nuc} is about the same for simulations with the slip form and combined form.

$r/r_{\text{nuc}} \gtrapprox 2$, the aseismic slip only penetrates a radial distance of $2r_{\text{nuc}}$, at which point a seismic event nucleates within this aseismically slipping band. This is exactly what we observe in our 3D simulations. Figure 5.13 illustrates two representative cases, with $r/r_{\text{nuc}} = 1.2$ (left column) and $r/r_{\text{nuc}} = 11$ (right column). In the case of $r/r_{\text{nuc}} = 1.2 < 2$, aseismic creep penetrates all the way into the center of the patch, and nucleation processes start from the center of the patch. For simulations with the aging form and $1 \leq r/r_{\text{nuc}} \lessapprox 2$, seismic ruptures usually also start from the center of the patch. For simulations with the slip form and $1 \leq r/r_{\text{nuc}} \lessapprox 2$, the nucleation zone keeps shrinking to one side and seismic ruptures usually start from the border of the patch (figure 5.13, left column). When $r/r_{\text{nuc}} = 11 > 2$, aseismic creep only penetrates a certain radial distance into the patch, which is comparable to $2r_{\text{nuc}}$, and earthquakes nucleate in this penetrated region (figure 5.13, right column). Let us denote this creep-penetrated radial distance by r_{creep}. Figure 5.14 gives the values of

$r_{\mathrm{creep}}/2r_{\mathrm{nuc}}$ for different patch sizes and a representative set of parameters a and b, for both 3D and 2D simulations with slip and aging forms of state evolution. As figure 5.14 shows, r_{creep} is indeed approximately constant for different patch sizes and approximately equal to $2r_{\mathrm{nuc}}$ for 3D simulations. Note that the ratio $r_{\mathrm{creep}}/2r_{\mathrm{nuc}}$ is a little larger for simulations with the slip form than for those with the aging form. Interestingly, 2D simulations have larger $r_{\mathrm{creep}}/2r_{\mathrm{nuc}}$, by about a factor of two, than 3D simulations with the same state evolution law.

For relatively small patch sizes, aseismic slip creeps all the way into the center of the patch, and hence the seismic slip d_0 at the center of the patch is only a portion of the total slip $V_{\mathrm{L}}T$. The ratio between the seismic slip and total slip at the center of the patch is observed to increase with the patch size in our simulations, all the way to 1, as expected (figure 5.15a). When the patch size is large enough, aseismic slip only creeps into the patch for a distance of r_{creep}, thus the seismic slip at the center of the patch is the same as the total slip. The transition of the ratio $d_0/V_{\mathrm{L}}T$ to 1 occurs when the patch radius is about equal to r_{creep}, or $2r_{\mathrm{nuc}}$ for 3D simulations. The dependence of $d_0/V_{\mathrm{L}}T$ on the patch radius is similar for 2D and 3D simulations with the aging and slip forms, with slight difference in the transition point, which is related to the difference in r_{creep}. The ratio between the seismic moment M_0 and total moment on the patch $\mu AV_{\mathrm{L}}T$, where A is the patch area, increases rapidly for patch radius smaller than r_{creep}, and more gradually for larger patch radius (figure 5.15b). A fraction of the total moment is released through aseismic slip even for relatively large patches, due to the aseismic slip in the creep-in zone around the patch boundary. Since M_0 for seismic events is calculated as the seismic moment on the

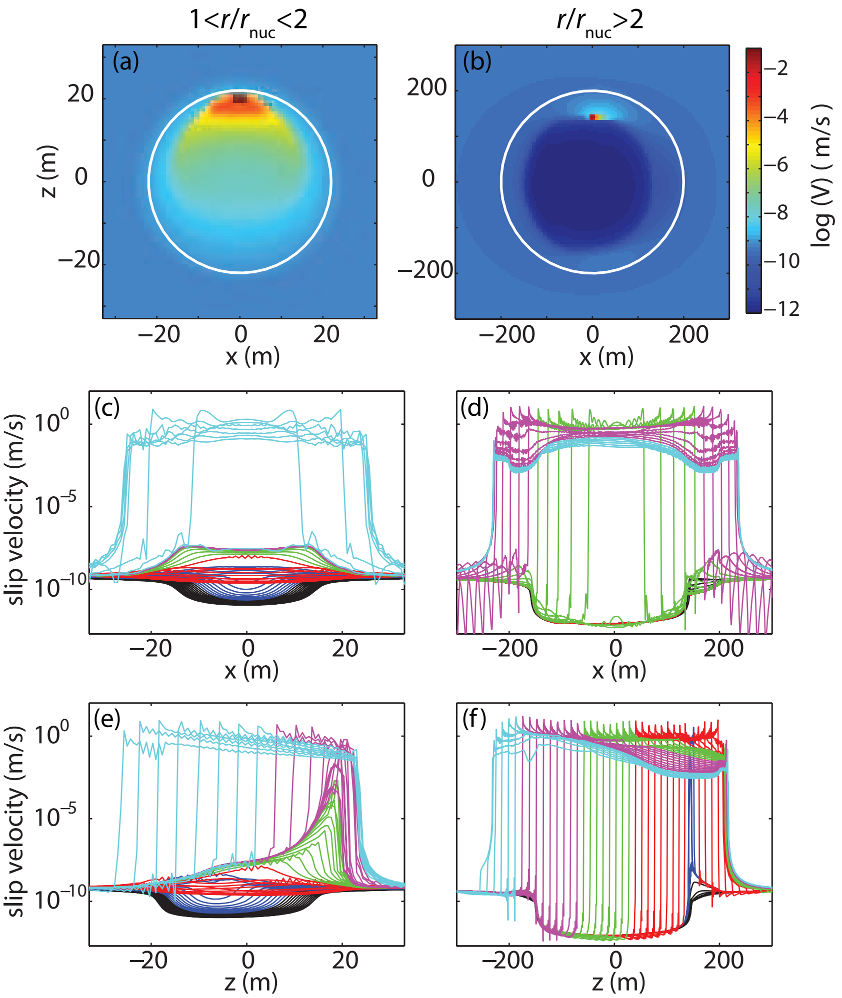

Figure 5.13. Representative nucleation processes for two r/r_{nuc} regimes: $r/r_{\mathrm{nuc}} = 1.2 < 2$ (left column) and $r/r_{\mathrm{nuc}} = 11 > 2$ (right column). The slip form of the state variable evolution is used. (a-b) Slip velocity distribution over part of the fault, when the maximum slip velocity reaches the seismic limit of 0.1 m/s. (c-f) The nucleation and rupture processes in terms of the evolution of slip velocity along the x- (c-d) and z- (e-f) axes are plotted every several time steps (note that the time steps are variable). The time progression in the slip velocity profiles is illustrated through varied colors, with black, blue, red, green, magenta, and cyan showing progressively later times.

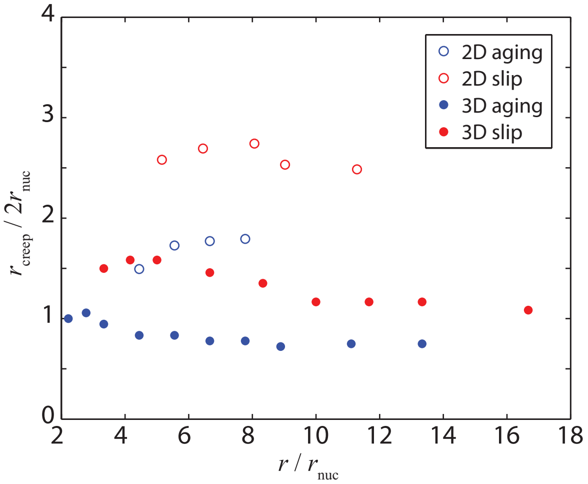

Figure 5.14. The ratio between the creep-in distance r_{creep} and the smallest patch dimension $2r_{\text{nuc}}$ that produces seismic events. r_{creep} is about the same as $2r_{\text{nuc}}$ for the simulated range of patch radii r in 3D simulations with the aging or slip form, as expected. The ratio $r_{\text{creep}}/2r_{\text{nuc}}$ is larger for simulations with the slip form than those with the aging form. 2D simulations generally have larger $r_{\text{creep}}/2r_{\text{nuc}}$ than 3D simulations.

entire fault (the patch and the surrounding area), and seismic ruptures can penetrate into the velocity-strengthening area outside the patch, the ratio $M_0/\mu A V_{\text{L}} T$ may be slightly larger than 1 for simulations with the larger patch radii. The dependence of the ratio $d_0/V_{\text{L}}T$ or $M_0/\mu A V_{\text{L}} T$ on the patch size does not seem to have a systematic dependence on parameters a, b we use in this study, so figure 5.15 shows the results for one representative set of parameters a and b.

Now that we have established that r_{nuc} is a relevant measure for estimating the extent of aseismic creep-in for larger patches, let us investigate which theoretical estimates match the simulated values of r_{nuc}. As introduced in section 5.2, three different estimations (5.7-5.9) of nucleation half-size have been proposed. Figure 5.16 shows the comparison between r_{nuc} and the proposed estimations of the nucleation half-length, for 2D simulations with the aging and slip form. The results for the simulations with the aging form are clearly better

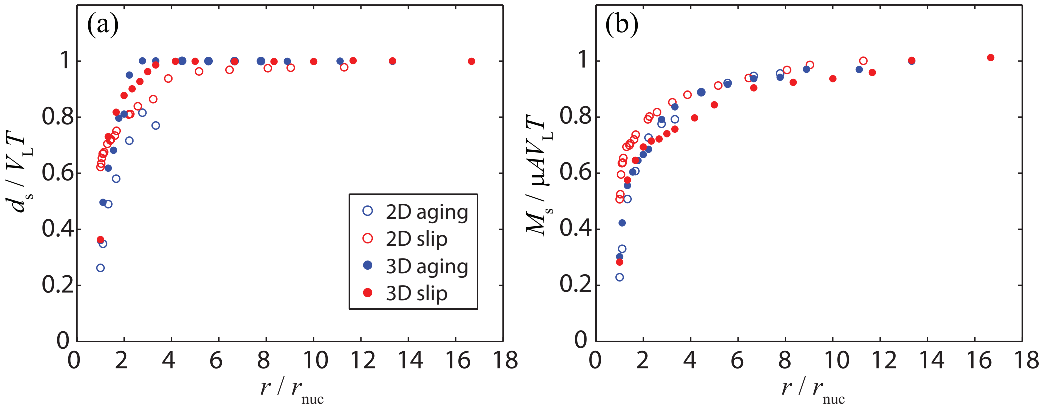

Figure 5.15. (a) The ratio between the seismic slip d_0 at the center of the patch and the total slip $V_{\mathrm{L}}T$ in one earthquake cycle, plotted vs. the patch radius. (b) The ratio between the seismic moment M_0 and the total moment $\mu AV_{\mathrm{L}}T$ of one earthquake cycle on the patch vs. the patch radius.

matched by h^*_{RA}. The results for the simulations with the slip form are better matched by h^*_{b-a} in terms of the dependence on parameters a and b; the values of r_{nuc} are about 2 times larger than h^*_{b-a}. The fit of r_{nuc} by the estimations of the nucleation half-length for all the simulations is summarized in table 5.7. For the sets of parameters a and b used in this study, r_{nuc} for the simulations with the aging form are best fitted by h^*_{RA}, and r_{nuc} for the simulations with the slip, combined, and composite forms are best fitted by h^*_{b-a}. The fit of r_{nuc} by the corresponding best estimation of the nucleation half-length is better for 2D simulations than 3D simulations with the same state evolution laws. Note that the values in table 1 do not depend on the constant prefactors of the nucleation size estimates.

5.8 Theoretical Model for Scaling

As shown in section 5.7, the simulated earthquakes can be divided into two regimes based on the ratio between the patch radius r and the nucleation half-length r_{nuc}. The numerically

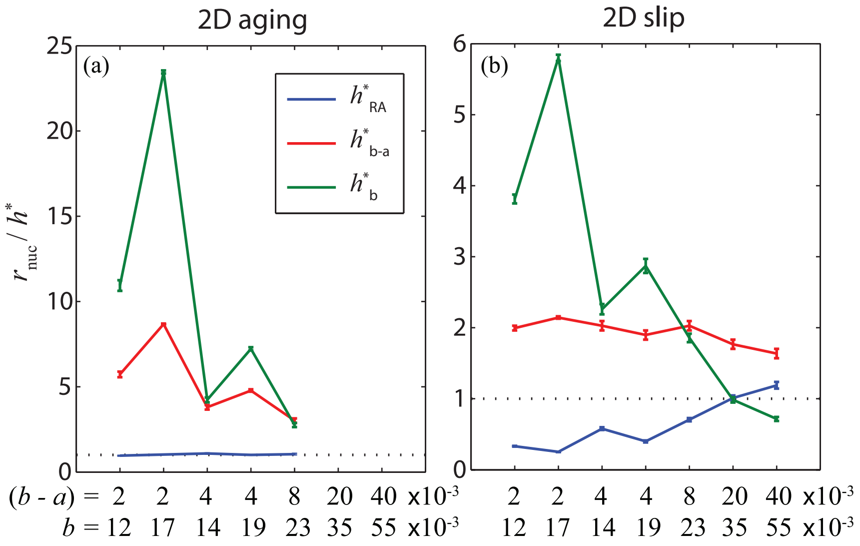

Figure 5.16. The ratio between the simulated nucleation half-size r_{nuc} and theoretical estimates of the nucleation half-size h^* for different sets of parameters a, b. Three different estimations of h^* are used, as discussed in the text. The dotted line illustrates how the perfect fit would look. (a) The simulated values of r_{nuc} for a 2D antiplane model with the aging form are better fitted by h^*_{RA}. (b) The simulated values of r_{nuc} for a 2D antiplane model with the slip form are better fitted by h^*_{b-a}, with the difference by a factor of about 2.

Table 5.1. Standard deviation of normalized r_{nuc}/h^* for different estimations of nucleation half-length h^* and simulations with different state evolution forms [1]

	$\text{std}[\frac{r_{\text{nuc}}/h^*_{\text{RA}}}{\text{mean}(r_{\text{nuc}}/h^*_{\text{RA}})}]$	$\text{std}[\frac{r_{\text{nuc}}/h^*_{b-a}}{\text{mean}(r_{\text{nuc}}/h^*_{b-a})}]$	$\text{std}[\frac{r_{\text{nuc}}/h^*_{b}}{\text{mean}(r_{\text{nuc}}/h^*_{b})}]$
2D aging	**0.05**	0.42	0.85
2D slip	0.55	**0.09**	0.67
3D aging	**0.22**	0.31	0.74
3D slip	0.46	**0.21**	0.79
3D combined	0.25	**0.17**	0.60
3D composite	0.30	**0.17**	0.62

[1] The smallest standard deviation for each model (a combination of 2D/3D and a state evolution form) is highlighted in bold.

determined nucleation half-length r_{nuc} can be approximated by the estimates discussed in section 5.2, and these estimates are denoted by h^* here for simplicity. In 3D simulations with a circular patch, for $1 \lessapprox r/h^* \lessapprox 2$, aseismic slip penetrates all the way into the center of the patch, and the earthquake nucleation starts from the center of the patch. For $r/h^* \gtrapprox 2$, aseismic slip penetrates into the patch for the radial distance of only about $2h^*$, and the earthquake nucleates in this penetrated annular region.

First, let us consider the regime of $1 \lessapprox r/h^* \lessapprox 2$. The stress levels before and after the earthquake can be approximated as the steady-state stresses with slip velocities equal to loading velocity V_{L} ($\sim 10^{-9}$ m/s) and dynamic slip velocity V_{dyn} (~ 1 m/s) respectively (figure 5.17a, c):

$$\begin{aligned} \Delta\tau &= \tau_i - \tau_f \approx \sigma[f_0 + (a-b)\ln(V_{\mathrm{L}}/V_0)] - \sigma[f_0 + (a-b)\ln(V_{\mathrm{dyn}}/V_0)] \\ &= \sigma(b-a)\ln(V_{\mathrm{dyn}}/V_{\mathrm{L}}) \approx (9\ln 10)(b-a)\sigma. \end{aligned} \tag{5.10}$$

The seismic slip on the patch has the elliptical shape expected from a circular crack model with a constant stress drop (figure 5.17b, d) (*Eshelby*, 1957; *Keilis-Borok*, 1959):

$$d(\rho) = \frac{24\Delta\tau}{7\pi\mu}\sqrt{r^2 - \rho^2}, \tag{5.11}$$

where ρ is the distance from the center of the patch. Depending on the stress drop on the patch and the frictional properties of the surrounding velocity-strengthening region, the seismic event can rupture an area larger than the velocity-weakening patch, and result in slip larger than that shown in equation (5.11). For the frictional parameters used in this

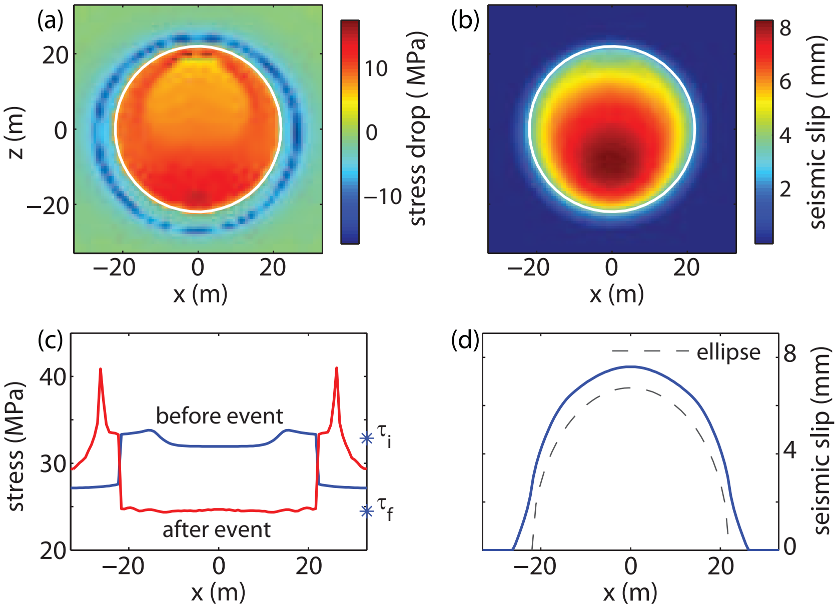

Figure 5.17. Example of stress drop and seismic slip for events with $1 \lessapprox r/h^* \lessapprox 2$ (with the slip form, $a = 0.015$, $b = 0.023$, $r/h^* \approx 1.2$): (a, b) maps of stress drop and seismic slip over the fault, (c, d) cross section along the x direction and through the center of the patch. Estimated stress levels before (τ_i) and after (τ_f) the earthquake from equation (5.10) are indicated as asterisks. Stress drop is approximately constant in this case, and the seismic slip has a shape similar to the elliptical function from equation (5.11) (dashed line in (d)).

paper, these effects are relatively small, thus we ignore them for simplicity. Based on the above considerations, we could estimate the seismic moment as (*Brune*, 1970):

$$M_0 = \frac{16}{7}\Delta\tau r^3. \tag{5.12}$$

If the center of the patch slips only seismically, we would expect that $T = d(0)/V_L$. Based on equation (5.11), this implies $T \propto r \propto M_0^{1/3}$. However, as shown in figure 5.15, the seismic slip is only part of the total slip on the center of the patch for $r/h^* \lessapprox 2$, and the ratio of seismic to total slip increases with r/h^*. Hence we expect a scaling between T and M_0 with an exponent smaller than 1/3, as the simulation results show.

For the case with $r/h^* \gtrapprox 2$, the recurrence time is determined by the nucleation time, which in turn is determined by the time for the creep to penetrate the distance of $2h^*$ into the patch. The stressing rate at the location of $2h^*$ inside the patch due to steady creep outside the patch can be expressed by (*Das and Kostrov*, 1986):

$$\dot{\tau} = C\frac{\mu V_\mathrm{L}}{\sqrt{r^2 - (r - 2h^*)^2}}, \tag{5.13}$$

where C is a model-dependent constant. By the time the earthquake starts, the stress on the annulus of $2h^*$ has reached $\Delta\tau$ (figure 5.18a,c), thus we can estimate the recurrence time as

$$T = \frac{\Delta\tau}{C\mu V_\mathrm{L}}\sqrt{r^2 - (r - 2h^*)^2}. \tag{5.14}$$

Our model differs from the model of *Das and Kostrov* (1986) in that the creep front changes, so we expect that the stressing rate is higher and the expression (5.13) needs to be adjusted. An exact solution is not straightforward to obtain, since the speed of the creeping front is unknown and potentially variable. We approximately account for the difference by adjusting the constant C in *Das and Kostrov* (1986). The constant C is determined by relating equation (5.14) to equation (5.11). For $r = 2h^*$, we expect that all slip at the center of the patch is seismic, and the recurrence times calculated based on equation (5.14) and equation (5.11) are the same. Thus we have

$$T = \frac{24\Delta\tau}{7\pi\mu V_L}\sqrt{r^2 - (r - 2h^*)^2} = \frac{48\Delta\tau}{7\pi\mu V_L}\sqrt{rh^* - h^{*2}}. \tag{5.15}$$

The seismic slip on the annulus of thickness $2h^*$ has an elliptical shape, and the seismic

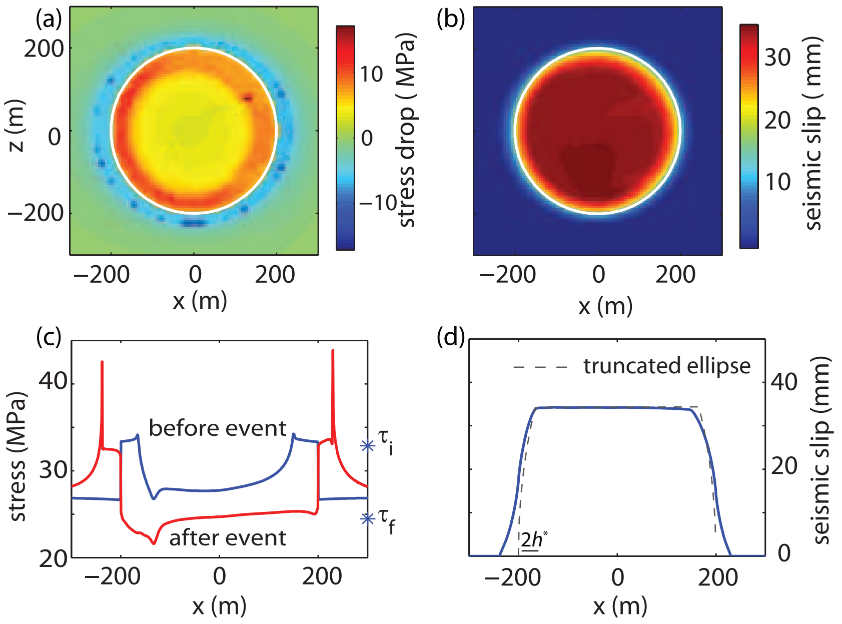

Figure 5.18. Similar to figure 5.17, but for events with $r/h^* \gtrapprox 2$ ($r/h^* \approx 11$). Stress drop is smaller in the center of the patch, and the seismic slip can be approximated with a truncated elliptical function.

slip on the central circular patch area is approximately constant and nearly equal to $V_{\mathrm{L}}T$ because almost all the slip on the central area is accumulated seismically (figure 5.18b, d). Thus we could estimate the seismic moment as:

$$M_0 = \frac{\mu\pi V_L T}{3}(2r^2 + (r-2h^*)^2) = \frac{16\Delta\tau}{7}\sqrt{rh^* - h^{*2}}(3r^2 - 4rh^* + 4h^{*2}). \tag{5.16}$$

The expected scaling of T vs. M_0 based on equations (5.15) and (5.16) is shown in figure 5.19. The scaling is steeper for smaller $r/(2h^*)$. For $r/(2h^*) \gg 1$,

$$T = \frac{48\Delta\tau}{7\pi\mu V_L}\sqrt{rh^*} \propto r^{1/2}, \tag{5.17}$$

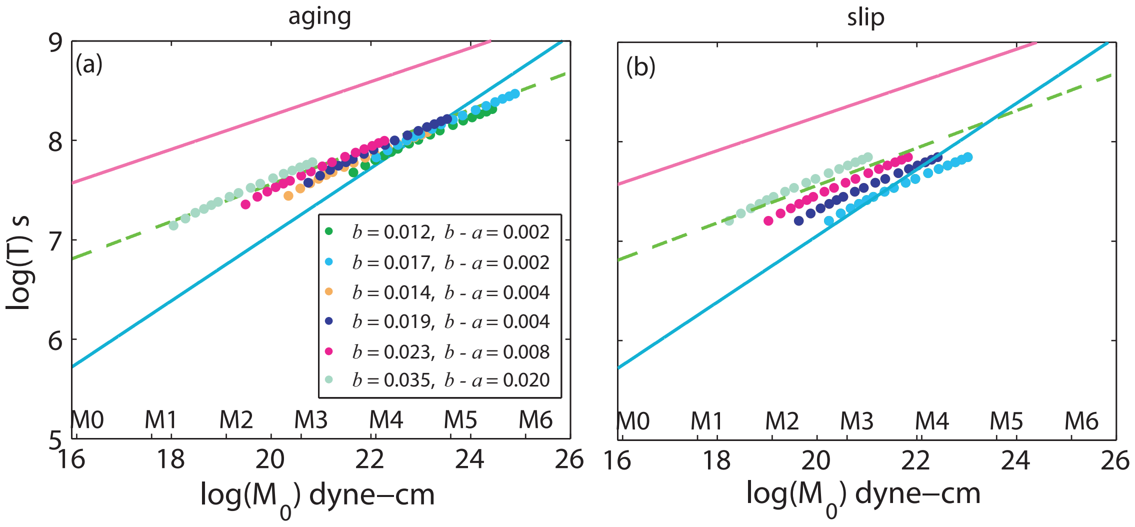

Figure 5.19. Estimated seismic moment and recurrence time for 3D simulations with the (a) aging form and (b) slip form based on equations (5.10), (5.15), and (5.16). For each set of a and b, patch radius r is varied so that r/h^* ranges from 2 to 20. $h^* = (\pi^2/4)h^*_{\mathrm{RA}}$ for the aging form and $h^* = 5h^*_{b-a}$ for the slip form based on the simulations. The estimated scaling is similar to simulated scaling (green dashed line). Note that the absolute level of T depends on b for the aging form and $(b-a)$ for the slip form. The lines have the same meaning as in figure 5.2.

and

$$M_0 = \frac{48\Delta\tau}{7} r^{5/2}\sqrt{h^*} \propto r^{5/2}. \tag{5.18}$$

Hence we have

$$T = (\frac{48}{7})^{4/5}\frac{\Delta\tau^{4/5}h^{*2/5}}{\pi\mu V_L}M_0^{1/5} \propto M_0^{0.2}, \tag{5.19}$$

close to the observations of $T \propto M_0^{0.17}$. The steeper scaling for smaller $r/(2h^*)$ explains why some simulated results seem to deviate from the observed scaling if only a limited range of r/h^* is studied (figure 5.3).

Since h^* has different dependence on a and b for the aging form and slip form (section

5.7), we expect different dependence of T and M_0 on a and b. Here we consider the limit of $r/(2h^*) \gg 1$. For the aging form, $h^* = (\pi^2/4)h^*_{\mathrm{RA}}$, and we have

$$T = 15\frac{(\sigma L b)^{2/5}}{V_{\mathrm{L}}\mu^{3/5}}M_0^{1/5}, \tag{5.20}$$

For the slip form, $h^* = 5h^*_{b-a}$, and we have

$$T = 20\frac{[\sigma L(b-a)]^{2/5}}{V_{\mathrm{L}}\mu^{3/5}}M_0^{1/5}, \tag{5.21}$$

Since the values of a and b used in our simulations have larger variations in $(b-a)$ than in b, we expect the simulated T with the slip form to show larger spread than that with the aging form, as figure 5.19 shows. This difference is observed in the simulated results (figure 5.3). The theoretically predicted dependence of T on L is validated by the simulation results from chapter 4.

5.9 Parameter combinations that allow to match the observed ranges of T and M_0

For model parameters used in this study, the exponent of the simulated scaling between T and M_0 is similar to the observation. However, the simulated absolute value of T for a given M_0 is about 5 times smaller than the observation (figure 5.3). One way to match the observed absolute values of T is to decrease V_{L} from 23 mm/a to 4.5 mm/a as done in chapter 4. Based on equation (5.19), other solutions may also exist, and here we explore the possibilities.

Note that, as we vary parameters in equation (5.19) to match the values of T, the magnitude of the smallest seismic event that can be produced in this model, which we denote M_{s}, may also change. For simulations that do not produce seismic events that rupture only a part of the patch (seismic pattern I), the seismic moment of the smallest event can be expressed as:

$$M_{\mathrm{s}} = \frac{16}{7}\Delta\tau h^{*3}. \tag{5.22}$$

For standard logarithmic rate and state formulations considered in this study, equation (5.22) can be written as:

$$M_{\mathrm{s}} = 23\frac{(\mu L b)^3}{\sigma^2(b-a)^5} \quad \text{(the aging form)} \tag{5.23}$$

or

$$M_{\mathrm{s}} = 191\frac{(\mu L)^3}{\sigma^2(b-a)^2} \quad \text{(the slip form).} \tag{5.24}$$

Because events as small as magnitude 0 to 1 are observed (*Nadeau and Johnson*, 1998), M_{s} should not be above that level as model parameters are adjusted to match T. For example, increasing only L to match T would not be an acceptable solution, since M_{s} is rapidly increasing with L.

Based on the developed theoretical model for scaling (equations 5.20–5.21) and the smallest moment expression (equations 5.23–5.24), one way to match observations is to decrease μ to about 2 GPa. Such low shear modulus, however, is not clearly supported by observations. Hence, in the following, we set $\mu = 30$ GPa and consider the combined variations of other parameters for models with the slip form of the state variable evolution; models with the aging form can be analyzed similarly.

First, let us consider the combinations of parameters L and $\sigma(b-a)$ that would allow the model to match observations for $V_L = 23$ mm/a. As shown in figure 5.20, the values of $\sigma(b-a)$ that match the observations are larger than 8 MPa. If $(b-a) \approx 0.01$, an upper bound of the values observed in the lab, this requires $\sigma \gtrapprox 800$ MPa, which is only realistic if large local variations in compressive stress exist, e.g., due to fault non-planarity (*Sagy et al.*, 2007; *Dunham et al.*, 2011), and repeating earthquakes occur on highly compressed patches. If $\sigma = 100$ MPa, then $(b-a) \gtrapprox 0.08$, about an order of magnitude larger than what is observed in the lab, and perhaps suggestive of enhanced dynamic weakening as discussed later.

Now, let us fix several values of $\sigma(b-a)$ and consider how much smaller than 23 mm/a V_{L} needs to be for the standard logarithmic rate- and state-model to reproduce the observed level of T. If $\sigma(b-a) = 0.2$ MPa, a typical value in this study and chapter 4, then V_{L} needs to be as small as 2 mm/a (figure 5.21). Note that this is for the slip form; simulations with the aging form reproduce observations for a higher value of $V_{\mathrm{L}} = 4.5$ mm/a. If $\sigma(b-a) =$ 2 MPa, on the high side of potential rate-and-state values, then V_{L} can be up to about 9 mm/a (figure 5.22), potentially reasonable for the transitional region between creeping and locked segments where most of the repeating earthquakes are observed at Parkfield. So

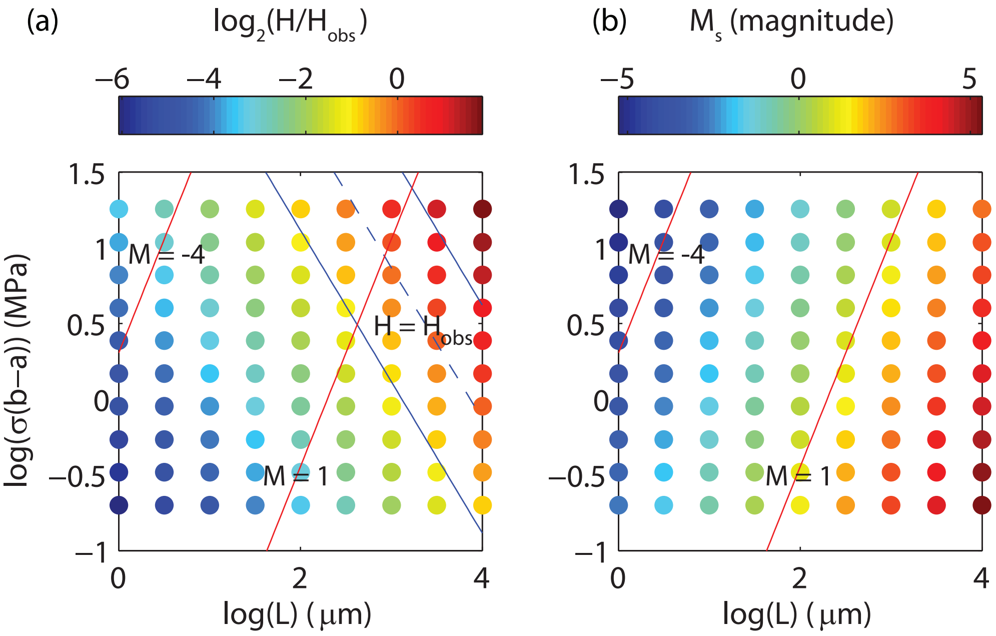

Figure 5.20. The recurrence time level and seismic moment based on theoretical prediction (equations 5.21, 5.24), with $\mu = 30$ GPa and $V_{\mathrm{L}} = 23$ mm/a, to explore the ranges of $\sigma(b-a)$ and L that may match the observations. (a) The absolute level of T, plotted as $H = T/M_0^{1/5}$, normalized by the value that matches the observation (H_{obs}). Contour of $H = H_{\mathrm{obs}}$ is indicated by the dashed line, with parallel solid lines indicating $H = 2H_{\mathrm{obs}}$ and $H = 0.5H_{\mathrm{obs}}$. (b) The smallest events that can be produced in our model (M_{s} in magnitude). Contours of $\mathrm{M} = -4$ and $\mathrm{M} = 1$ are plotted.

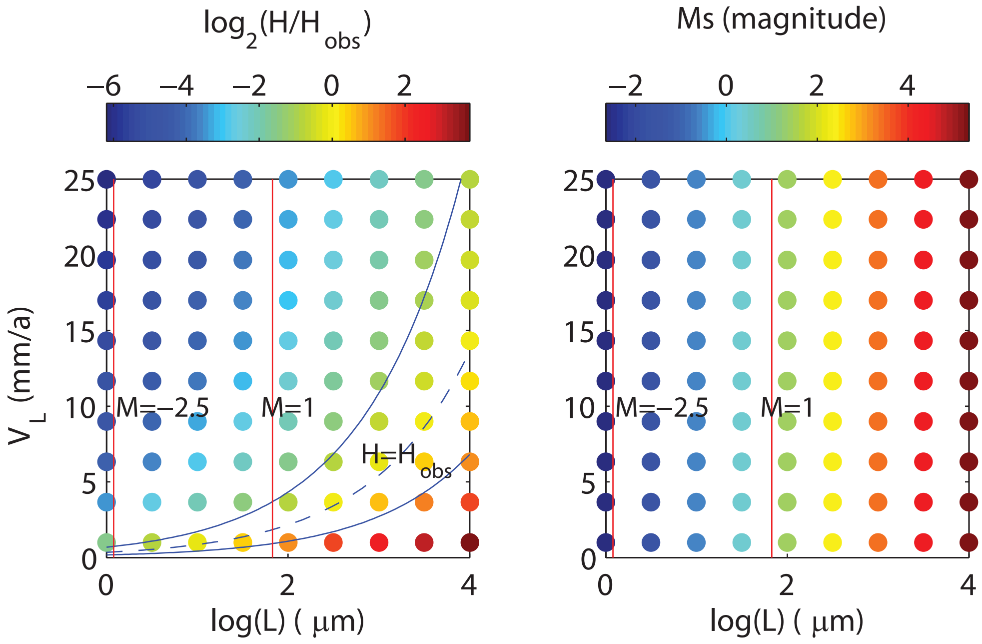

Figure 5.21. The recurrence time level and seismic moment based on theoretical prediction (equations 5.21, 5.24), with $\mu = 30$ GPa and $\sigma(b-a) = 0.2$ MPa, to explore the ranges of V_{L} and L that may match the observations. (a) The absolute level of T, plotted as $H = T/M_0^{1/5}$, normalized by the value that matches the observation (H_{obs}). Contour of $H = H_{\mathrm{obs}}$ is indicated by the dashed line, with parallel solid lines indicating $H = 2H_{\mathrm{obs}}$ and $H = 0.5H_{\mathrm{obs}}$. (b) The smallest events that can be produced in our model (M_{s} in magnitude). Contours of $\mathrm{M} = -2.5$ and $\mathrm{M} = 1$ are plotted.

with the standard logarithmic rate and state friction laws and typically considered $\sigma(b-a)$, V_{L} needs to be much smaller than 23 mm/a to match observations.

Based on equations (5.19) and (5.22), another possibility is to increase the stress drop, $\Delta\tau$, about 7 times while keeping h^* the same. This could be achieved by incorporating enhanced dynamic weakening, which lowers τ_f in equation (5.10) significantly. High stress drops (average stress drop over the areas of positive slip of 10–20 MPa and local stress drops as high as 60–90 MPa) have been inferred from seismic observations for small repeating earthquakes at Parkfield (*Dreger et al.*, 2007). Hence a model with enhanced dynamic weakening at seismic slip rates should simultaneously match both the exponent and

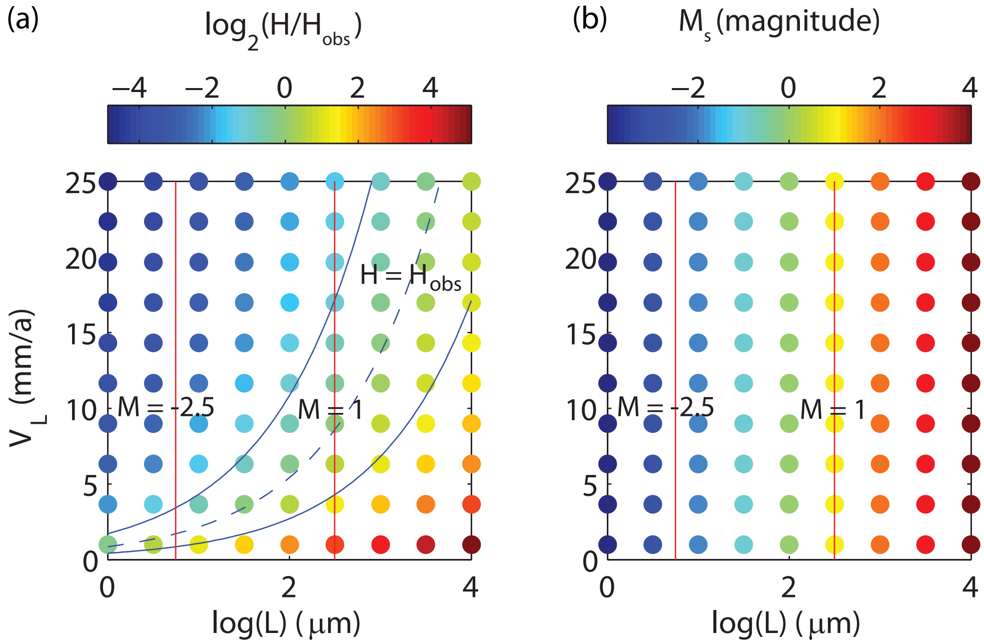

Figure 5.22. Similar to figure 5.21, but with $\sigma(b-a) = 2$ MPa.

absolute level of the observed scaling between T and M_0, as well as the observed relatively high stress drops, with the creeping rate close to 23 mm/a.

5.10 Discussion

In this work, we have proposed a theoretical model for the scaling between the recurrence time and seismic moment. It is interesting to look at what implications this model may have. In our proposed theoretical model, the stress drop is approximately constant for $1 \lessapprox r/h^* \lessapprox 2$. For $r/h^* \gtrapprox 2$, the nucleation happens as soon as the annulus of $2h^*$ reaches the stress level of $\Delta\tau$. One consequence is that for the larger patch sizes, the center of the patch is less stressed, and thus the average stress drop over the patch decreases. The behavior of stress drops in these two regimes is consistent with the findings of *Kato* (2012), who considers a slightly different problem. Note that our theoretical consideration predicts that the average stress drop would be small for large r/h^*, the model is not valid for too large r/h^*. This is because for large enough r/h^*, the stress state closer to the middle of the patch becomes too low for the rupture to propagate, smaller events at the boundary of the patch start to occur, and the periodicity of the produced seismic events sequence goes away. This implies that the observed repeating sequences have the values of r/h^* within a certain range. For example, in our simulations with the slip form and $b - a = 0.02$, we have r/h^* from 1 to 17. The corresponding seismic moments span a range of about two magnitudes, while the average stress drops only differ for a factor smaller than 2. Such small variations would not be easy to determine seismologically, especially given the likely variation in friction properties of the earthquake-producing patches and hence the corresponding scatter in stress drop values. Note that since h^* depends on parameters such as a, b, L, and σ, larger r/h^* does not necessarily mean larger r and larger magnitude of events. We expect scattering of stress drops with magnitudes due to the variations of a, b, L, or σ.

We note that in our theoretical consideration, for $r/(2h^*) \gg 1$, the average seismic slip d on the patch can be expressed as:

$$d \propto V_L T \propto (\mu_i - \mu_f)\sqrt{\frac{\sigma L r}{\mu}}, \tag{5.25}$$

where μ_i and μ_f are the effective friction coefficients before and after the earthquake, i.e., $\mu_i = \tau_i/\sigma$, $\mu_f = \tau_f/\sigma$. The square root dependence of d on $\sigma L r/\mu$ agrees with the study that considers the balance between the fracture energy and energy release rate in a similar model (*Kato*, 2012). The consideration in *Kato* (2012) leads to slightly different dependence of d on the frictional coefficients, with

$$d \propto \sqrt{\mu_p - \mu_f}\sqrt{\frac{\sigma L r}{\mu}}, \tag{5.26}$$

where μ_p is the peak (yield) friction coefficient. To differentiate between these two models, we have conducted two simulations with the same parameters except that one has enhanced dynamic weakening and hence lower μ_f. We use the thermal pore pressurization mechanism to achieve enhanced dynamic weakening while keeping the slip weakening distance about the same, following *Noda and Lapusta* (2010). We find that, compared with the results with the standard logarithmic rate and state formulations, for the case with enhanced dynamic weakening, the effective $(\mu_i - \mu_f)$ is about 3 times larger, $\sqrt{\mu_p - \mu_f}$ is about 1.3 times larger, and the average seismic slip is about 3 times larger. Thus the model based on the nucleation time consideration (equation 5.25) quantitatively explains the results better than the model based on the balance between the fracture energy and energy release rate (equation 5.26). Note that the main focus of *Kato* (2012) is not about the dependence of d on the frictional coefficients, but the scaling between d and σD_c, where D_c is the slip weakening distance and proportional to L. So the main discussion in *Kato* (2012) is not affected by this difference.

Based on our theoretical consideration, there are two ways to explain the observed scaling between the recurrence time and seismic moment depending on the patch size. When the patch size is comparable with the nucleation length, the stress drop is about constant for events with different magnitudes, but more aseismic slip is observed for smaller magnitude events, and thus longer recurrence time, bringing the scaling flatter than $T \propto$

$M_0^{1/3}$. The models investigated in chapter 4 are mostly within this regime. In this work, we study larger patch sizes compared with the nucleation length, and find that the resulting scaling is also flatter than $T \propto M_0^{1/3}$. The scaling can be explained by the model in which the recurrence time is determined by the time it takes aseismic creep to penetrate the distance of $2h^*$ into the patch. Our theoretical consideration predicts that the simulated scaling would be close to $T \propto M_0^{0.2}$. The theoretical model we propose only considers the seismic events that rupture the whole velocity-weakening patch. The seismic events that rupture only a part of the patch are observed with the aging form, especially for smaller $(b-a)$. Interestingly, these two types of events together also follow the $T \propto M_0^{0.17}$ scaling (figure 5.3a, 5.4a). The underlying reason for this has not yet been determined.

The theoretical consideration we propose is useful to understand and predict some observations and numerical simulation results. Considering repeating earthquake sequences on different faults, it is reasonable to assume that they have similar values of shear modulus μ, typical stress drops, and the range of the ratio between the patch sizes and nucleation sizes. Equation (5.19) thus predicts that the scalings between the recurrence time and seismic moment for repeating earthquake sequences on different faults are similar, with only a factor difference of loading velocity V_{L}. The same dependence of the scaling of T vs. M_0 on V_{L} as predicted by our model has been shown by observations (*Chen et al.*, 2007).

The loading velocity of 23 mm/a is used following *Nadeau and Johnson* (1998), and to make direct comparison with the study in chapter 4. As discussed in chapter 4, and also the theoretical consideration developed in this work (equations 5.19 and 5.22), small variations in V_{L} will not change the exponent of the scaling between T and M_0 or the smallest magnitude of the events that can be produced, but only move the absolute values of T up and down. Note that orders-of-magnitude change in V_{L} may change the seismic moment (*Chen et al.*, 2010). A loading velocity of 4.5 mm/a matches both the exponent of the scaling between T and M_0, and the absolute values of T (chapter 4). This value of V_{L} is consistent with the GPS inversion results in the region of small repeating earthquakes at Parkfield (S. Barbot, personal communication). Other ways to change the values of T without changing the T vs. M_0 scaling exponent include changing the values of stress drop, μ, L, σ, b or $b - a$. However, the smallest earthquake that the model can produce may also change if we vary stress drop, μ, L, σ, b or $b - a$. We prefer the increase of stress drop to increase the absolute values of T, because it will only moderately increase the magnitude of the smallest events, and the value of the stress drop needed to match the absolute values of T is plausible if we include enhanced strong dynamic weakening. On the other hand, we should note that the smallest magnitude estimate based on equation (5.22) is only for the seismic pattern II events that rupture the whole patch. As showed in chapter 4 and this study, the seismic pattern I events that rupture only a part of the patch are observed under certain conditions, and they have much smaller magnitudes. If we could produce seismic pattern I events for a wider range of conditions, for example, by including other mechanisms such as dilatancy, the constraint on the smallest magnitude of the events can be relaxed.

5.11 Conclusions

We have investigated the behavior of small repeating earthquakes under different scenarios, including different state evolution forms, rectangular vs. circular patch, quasi-dynamic vs. fully dynamic simulations, 2D vs. 3D simulations, and found that, with proper interpretation, the overall scaling of the recurrence time and seismic moment seem to be similar. Differences in other characteristics of the repeating sequences do exist. For example, we find that the simulated nucleation half-length for simulations with the aging form is better approximated by h^*_{RA}, while that with the slip form is better approximated by h^*_{b-a}, consistent with differences between models with the two forms found in previous studies (*Ampuero and Rubin*, 2008). This different dependence of the nucleation half-length on parameters a and b results in (relatively minor) differences in scaling of T and M_0 for simulations with the aging and slip form.

We propose a theoretical consideration to explain why the simulated scaling matches the observations. The simulated events can be divided into two regimes based on the ratio of the patch radius to the full nucleation size. For patch radii comparable to the full nucleation size, the simulated scaling matches the observation mainly because the ratio of aseismic slip to total slip on the patch increases with smaller patch size. For patch radii larger than the full nucleation size, the simulated scaling matches the observation because the recurrence time is determined by the time for the creep to penetrate the distance of the full nucleation size into the patch. The existence of this second regime explains the relatively broad range of magnitudes for the events that follow the observed scaling.

The obtained theoretical insight has been used to find the combinations of fault properties that allow the model to fit the observed scaling and range of the seismic moment and recurrence time. For the standard logarithmic rate and state friction laws and typically considered values of $\sigma(b-a)$ (such as 0.2 MPa), V_L needs to be several times smaller than 23 mm/a to match the observations. If V_L is indeed close to 23 mm/a in the area of repeating earthquakes, then the required $\sigma(b-a)$ is more than an order of magnitude larger, pointing to either much larger local compression or enhanced dynamic weakening.

Bibliography

Abercrombie, R. E. (1995), Earthquake source scaling relationships from -1 to 5 M_L using seismograms recorded at 2.5-km depth, *J. Geophys. Res.*, *100*(B12), 24,015–24,036.

Alberto, C. A. O. (2010), Caracterización de la geometría de la zona benioff con una red densa de banda ancha en el istmo de Tehuantepec, Ph.D. thesis, National Autonomous University of Mexico.

Allmann, B. P., and P. M. Shearer (2007), Spatial and temporal stress drop variations in small earthquakes near Parkfield, California, *J. Geophys. Res.*, *112*, B04305, doi: 10.1029/2006JB004395.

Ampuero, J.-P., and A. M. Rubin (2008), Earthquake nucleation on rate and state faults - aging and slip laws, *J. Geophys. Res.*, *113*, B01302, doi:10.1029/2007JB005082.

Anderson, J. G., and S. E. Hough (1984), A model for the shape of the Fourier amplitude spectrum of acceleration at high frequencies, *Bull. Seismol. Soc. Am.*, *74*(5), 1969–1993.

Anooshehpoor, A. (2001), Quasi-static slip-rate shielding by locked and creeping zones as an explanation for small repeating earthquakes at Parkfield, *Bull. Seismol. Soc. Am.*, *91*, 401–403, doi:10.1785/0120000105.

Aster, R., B. Borchers, and C. Thurber (2005), *Parameter Estimation and Inverse Problems*, Elsevier Academic Press, Burlington.

Bayart, E., A. M. Rubin, and C. Marone (2006), Evolution of fault friction following large velocity jumps, *Eos Trans. AGU*, *87*(52), fall Meet. Suppl., Abstract S31A-0180.

Beeler, N. M., T. E. Tullis, and J. D. Weeks (1994), The roles of time and displacement in the evolution effect in rock friction, *Geophys. Res. Lett.*, *21*(18), 1987–1990.

Beeler, N. M., D. L. Lockner, and S. H. Hickman (2001), A simple stick-slip and creep-slip model for repeating earthquakes and its implication for microearthquakes at Parkfield, *Bull. Seismol. Soc. Am.*, *91*(6), 1797–1804, doi:10.1785/0120000096.

Blatter, D. L., and I. S. E. Carmichael (1998), Hornblende peridotite xenoliths from central Mexico reveal the highly oxidized nature of subarc upper mantle, *Geology*, *26*(11), 1035.

Brune, J. N. (1970), Tectonic stress and the spectra of seismic shear waves from earthquakes, *J. Geophys. Res.*, *75*(26), 4997–5009.

Bürgmann, R., D. Schmidt, R. M. Nadeau, M. d'Alessio, E. Fielding, D. Manaker, T. V. McEvilly, and M. H. Murray (2000), Earthquake potential along the northern Hayward Fault, California, *Science*, *289*, 1178–1182, doi:10.1126/science.289.5482.1178.

Campillo, M., S. K. Singh, N. Shapiro, J. Pacheco, and R. B. Herrmann (1996), Crustal structure south of the Mexican volcanic belt, based on group velocity dispersion, *Geofisica Internacional Mexico*, *35*, 361–370.

Carmichael, I. (2002), The andesite aqueduct: Perspectives on the evolution of intermediate magmatism in west-central (105–99°W) Mexico, *Contributions to Mineralogy and Petrology*, *143*, 641–663, doi:10.1007/s00410-002-0370-9.

Castro, R. R., J. G. Anderson, and S. K. Singh (1990), Site response, attenuation and source spectra of S waves along the Guerrero, Mexico, subduction zone, *Bull. Seismol. Soc. Am.*, *80*(6A), 1481.

Castro, V. H. E. (2009), Modelos de velocidad cortical en Mexico, utilizando funciones de receptor en las estaciones de la red nacional de banda ancha, Ph.D. thesis, Universidad Nacional Autonoma de Mexico.

Chen, K. H., R. M. Nadeau, and R.-J. Rau (2007), Towards a universal rule on the recurrence interval scaling of repeating earthquakes? *Geophys. Res. Lett.*, *34*, L16308, doi:10.1029/2007GL030554.

Chen, K. H., R. Bürgmann, R. M. Nadeau, T. Chen, and N. Lapusta (2010), Postseismic variations in seismic moment and recurrence interval of repeating earthquakes, *Earth Planet. Sci. Lett.*, *299*(1-2), 118–125, doi:10.1016/j.epsl.2010.08.027.

Das, S., and B. V. Kostrov (1986), Fracture of a single asperity on a finite fault: A model for weak earthquakes? in *Earthquake Source Mechanics*, edited by S. Das, J. Boatwright, and C. H. Scholz, pp. 91–96, American Geophysical Union, Washington.

DeMets, C., R. G. Gordon, D. F. Argus, and S. Stein (1994), Effect of recent revisions to the geomagnetic reversal time scale on estimates of current plate motions, *Geophys. Res. Lett.*, *21*, 2191–2194, doi:10.1029/94GL02118.

Dieterich, J. H. (1979), Modeling of rock friction 1. Experimental results and constitutive equations, *J. Geophys. Res.*, *84*(B5), 2161–2168.

Dieterich, J. H. (1981), Constitutive properties of faults with simulated gouge, in *Mechanical Behavior of Crustal Rocks*, *Geophys. Monogr. Ser.*, vol. 24, edited by J. Handin and N. L. Carter, pp. 103–120, AGU, Washington, D. C.

Dieterich, J. H. (1992), Earthquake nucleation on faults with rate-and state-dependent strength, *Tectonophysics*, *211*(1-4), 115–134.

Dieterich, J. H. (2007), Applications of rate-and-state-dependent friction to models of fault slip and earthquake occurrence, in *Treatise on Geophysics*, vol. 4, edited by H. Kanamori, pp. 107–129, Elsevier, Amsterdam.

Dreger, D., R. M. Nadeau, and A. Chung (2007), Repeating earthquake finite source models: Strong asperities revealed on the San Andreas fault, *Geophys. Res. Lett.*, *34*, L23302, doi:10.1029/2007GL031353.

Dunham, E. M., D. Belanger, L. Cong, and J. E. Kozdon (2011), Earthquake ruptures with strongly rate-weakening friction and off-fault plasticity, part 2: Nonplanar faults, *Bull. Seismol. Soc. Am.*, *101*, 2308–2322, doi:10.1785/0120100076.

Eberhart-Phillips, D. (1986), Three-dimensional velocity structure in northern California Coast Ranges from inversion of local earthquake arrival times, *Bull. Seismol. Soc. Am.*, *76*(4), 1025–1052.

Eberhart-Phillips, D. (1993), Local earthquake tomography: Earthquake source regions, in

Seismic Tomography: Theory and Practice, edited by H. M. Iyer and K. Hirahara, pp. 613–643, CRC Press, Boca Raton, Fla.

Eberhart-Phillips, D., and M. Chadwick (2002), Three-dimensional attenuation model of the shallow Hikurangi subduction zone in the Raukumara Peninsula, New Zealand, *J. Geophys. Res.*, *107*(B2), 2033, doi:10.1029/2000JB000046.

Eberhart-Phillips, D., M. Reyners, M. Chadwick, and J. Chiu (2005), Crustal heterogeneity and subduction processes: 3-D Vp, Vp/Vs and Q in the southern North Island, New Zealand, *Geophys. J. Int.*, *162*(1), 270–288.

Eberhart-Phillips, D., M. Reyners, M. Chadwick, and G. Stuart (2008), Three-dimensional attenuation structure of the Hikurangi subduction zone in the central North Island, New Zealand, *Geophys. J. Int.*, *174*, 418–434, doi:10.1111/j.1365-246X.2008.03816.x.

Ellsworth, W. L., and L. D. Dietz (1990), Repeating earthquakes: Characteristics and implications, in *Proceedings of Workshop 46, the 7th U.S.-Japan Seminar on Earthquake prediction*, 90-98, pp. 226–245, U.S. Geol. Surv. Open File Rept.

Eshelby, J. D. (1957), The determination of the elastic field of an ellipsoidal inclusion, and related problems, *Proceedings of the Royal Society of London. Series A. Mathematical and Physical Sciences*, *241*(1226), 376.

Ferrari, L. (2004), Slab detachment control on mafic volcanic pulse and mantle heterogeneity in central Mexico, *Geology*, *32*(1), 77–80, doi:10.1130/G19887.1.

Ferrari, L., M. López-Martínez, G. Aguirre-Díaz, and G. Carrasco-Núñez (1999), Spacetime patterns of Cenozoic arc volcanism in central Mexico: From the Sierra Madre Occidental to the Mexican Volcanic Belt, *Geology*, *27*(4), 303–306.

Ferrari, L., T. Tagami, M. Eguchi, M. Orozco-Esquivel, C. Petrone, J. Jacobo-Albarran, and M. López-Martínez (2005), Geology, geochronology and tectonic setting of late cenozoic volcanism along the southwestern Gulf of Mexico: The Eastern Alkaline Province revisited, *Journal of Volcanology and Geothermal Research*, *146*(4), 284–306.

Garcia, D., S. K. Singh, M. Herraiz, J. F. Pacheco, and M. Ordaz (2004), Inslab earthquakes of central Mexico: Q, source spectra, and stress drop, *Bull. Seismol. Soc. Am.*, *94*(3), 789–802.

Gomberg, J. S., and T. G. Masters (1988), Waveform modelling using locked-mode synthetic and differential seismograms: Application to determination of the structure of Mexico, *Geophys. J. Int.*, *94*, 193–218, doi:10.1111/j.1365-246X.1988.tb05896.x.

Gomberg, J. S., K. F. Priestley, T. G. Masters, and J. N. Brune (1988), The structure of the crust and upper mantle of northern Mexico, *Geophys. J. Int.*, *94*(1), 1–20.

Gómez-Tuena, M. T. O.-E., A., and L. Ferrari (2007), Igneous petrogenesis of the Trans-Mexican Volcanic Belt, in *Geology of Mexico*, edited by S. A. Alaniz-Álvarez and A. F. Nieto-Samaniego, 442, pp. 129–181, Geological Society of America.

Gorbatov, A., and Y. Fukao (2005), Tomographic search for missing link between the ancient Farallon subduction and the present Cocos subduction, *Geophys. J. Int.*, *160*, 849–854, doi:10.1111/j.1365-246X.2005.02507.x.

Harris, R. A., and P. Segall (1987), Detection of a locked zone at depth on the Parkfield, California, segment of the San Andreas fault, *J. Geophys. Res.*, *92*(B8), 7945–7962.

Haskov, J., and L. Ottemöller (1999), SEISAN earthquake analysis software, *Seismol. Res. Lett.*, *70*, 532–534.

Hauksson, E. (2000), Crustal structure and seismicity distribution adjacent to the Pacific and North America plate boundary in southern California, *J. Geophys. Res.*, *105*(B6), 13,875–13,904.

Hebert, L. B., P. Antoshechkina, P. Asimow, and M. Gurnis (2009), Emergence of a low-viscosity channel in subduction zones through the coupling of mantle flow and thermodynamics, *Earth Planet. Sci. Lett.*, *278*, 243–256, doi:10.1016/j.epsl.2008.12.013.

Hickman, S., M. Zoback, and W. Ellsworth (2004), Introduction to special section: Preparing for the San Andreas Fault Observatory at Depth, *Geophys. Res. Lett.*, *31*, L12S01, doi:10.1029/2004GL020688.

Hori, T., N. Kato, K. Hirahara, T. Baba, and Y. Kaneda (2004), A numerical simulation of earthquake cycles along the Nankai Trough in southwest Japan: Lateral variation in frictional property due to the slab geometry controls the nucleation position, *Earth Planet. Sci. Lett.*, *228*, 215–226, doi:10.1016/j.epsl.2004.09.033.

Husker, A., and P. M. Davis (2009), Tomography and thermal state of the Cocos plate subduction beneath Mexico City, *J. Geophys. Res.*, *114*, B04306, doi: 10.1029/2008JB006039.

Igarashi, T., T. Matsuzawa, and A. Hasegawa (2003), Repeating earthquakes and interplate aseismic slip in the northeastern Japan subduction zone, *J. Geophys. Res.*, *108*(B5), 2249, doi:10.1029/2002JB001920.

Iglesias, A., R. W. Clayton, X. Pérez-Campos, S. K. Singh, J. F. Pacheco, D. García, and C. Valdés-González (2010), S wave velocity structure below central Mexico using high-resolution surface wave tomography, *J. Geophys. Res.*, *115*(B6), B06307.

Imanishi, K., W. L. Ellsworth, and S. G. Prejean (2004), Earthquake source parameters determined by the SAFOD pilot hole seismic array, *Geophys. Res. Lett.*, *31*, L12S09, doi:10.1029/2004GL019420.

Jackson, I., M. S. Paterson, and J. D. Fitz Gerald (1992), Seismic wave dispersion and attenuation in åheim dunite: An experimental study, *Geophys. J. Int.*, *108*, 517–534, doi:10.1111/j.1365-246X.1992.tb04633.x.

Jödicke, H., A. Jording, L. Ferrari, J. Arzate, K. Mezger, and L. Rüpke (2006), Fluid release from the subducted Cocos plate and partial melting of the crust deduced from magnetotelluric studies in southern Mexico: Implications for the generation of volcanism and subduction dynamics, *J. Geophys. Res.*, *111*, B08102, doi:10.1029/2005JB003739.

Kao, H., S.-J. Shan, H. Dragert, G. Rogers, J. F. Cassidy, and K. Ramachandran (2005), A wide depth distribution of seismic tremors along the northern Cascadia margin, *Nature*, *436*, 841–844, doi:10.1038/nature03903.

Karato, S.-I. (2003), Mapping water content in upper mantle, in *Inside the Subduction Fac-*

tory, *Geophys. Monogr. Ser.*, vol. 138, edited by J. Eiler, pp. 135–152, AGU, Washington, D. C.

Kato, N. (2004), Interaction of slip on asperities: Numerical simulation of seismic cycles on a two-dimensional planar fault with nonuniform frictional property, *J. Geophys. Res.*, *109*, B12306, doi:10.1029/2004JB003001.

Kato, N. (2012), Dependence of earthquake stress drop on critical slip-weakening distance, *J. Geophys. Res.*, *117*, B01301, doi:10.1029/2011JB008359.

Kato, N., and T. E. Tullis (2001), A composite rate- and state-dependent law for rock friction, *Geophys. Res. Lett.*, *28*(6), 1103–1106.

Keilis-Borok, V. (1959), On estimation of the displacement in an earthquake source and of source dimensions, *Annali di geofisica*, *12*, 205–214.

Kennett, B. L. N., and E. R. Engdahl (1991), Traveltimes for global earthquake location and phase identification, *Geophys. J. Int.*, *105*, 429–465, doi:10.1111/j.1365-246X.1991.tb06724.x.

Kim, Y., R. W. Clayton, and J. M. Jackson (2010), Geometry and seismic properties of the subducting Cocos plate in central Mexico, *J. Geophys. Res.*, *115*, B06310, doi:10.1029/2009JB006942.

Kim, Y. H., R. W. Clayton, and F. Keppie (2011), Evidence of a collision between the Yucatán Block and Mexico in the Miocene, *Geophys. J. Int.*, *187*, 989–1000.

Kincaid, C., and I. S. Sacks (1997), Thermal and dynamical evolution of the upper mantle in subduction zones, *J. Geophys. Res.*, *102*, 12,295–12,315, doi:10.1029/96JB03553.

Lapusta, N., and Y. Liu (2009), Three-dimensional boundary integral modeling of spontaneous earthquake sequences and aseismic slip, *J. Geophys. Res.*, *114*, B09303, doi: 10.1029/2008JB005934.

Lapusta, N., and J. R. Rice (2003), Nucleation and early seismic propagation of small and large events in a crustal earthquake model, *J. Geophys. Res.*, *108*(B4), 2205, doi: 10.1029/2001JB000793.

Lapusta, N., J. R. Rice, Y. Ben-Zion, and G. Zheng (2000), Elastodynamic analysis for slow tectonic loading with spontaneous rupture episodes on faults with rate- and state-dependent friction, *J. Geophys. Res.*, *105*(B10), 23,765–23,789.

Lawrence, J. F., and M. E. Wysession (2006), Seismic evidence for subduction-transported water in the lower mantle, in *Earth's Deep Water Cycle*, edited by S. Jacobsen and S. van der Lee, AGU Monograph.

Liu, Y., and N. Lapusta (2008), Transition of mode II cracks from sub-Rayleigh to intersonic speeds in the presence of favorable heterogeneity, *J. Mech. Phys. Solids*, *56*, 25–50, doi:10.1016/j.jmps.2007.06.005.

Macías, J. L. (2007), Geology and eruptive history of some active volcanoes of Mexico, in *Geology of Mexico*, *Tretatise of Geophysics*, vol. 337, edited by S. A. Alaniz-Álvarez and A. F. Nieto-Samaniego, pp. 183–232, Geological Society of America.

Manea, M., V. C. Manea, and V. Kostoglodov (2003), Sediment fill in the Middle America Trench inferred from the gravity anomalies, *Geofis. Int.*, *42(4)*, 603–612.

Manea, V., M. Manea, V. Kostoglodov, and G. Sewell (2005), Thermo-mechanical model of the mantle wedge in Central Mexican subduction zone and a blob tracing approach for the magma transport, *Phys. Earth Planet. In.*, *149*, 165–186.

Marone, C. (1998), Laboratory-derived friction laws and their application to seismic faulting, *Annu. Rev. Earth Planet. Sci.*, *26*, 643–696, doi:10.1146/annurev.earth.26.1.643.

Marone, C., J. E. Vidale, and W. L. Ellsworth (1995), Fault healing inferred from time dependent variations in source properties of repeating earthquakes, *Geophys. Res. Lett.*, *22*(22), 3095–3098.

Matsubara, M., Y. Yagi, and K. Obara (2005), Plate boundary slip associated with the 2003 off-Tokachi earthquake based on small repeating earthquake data, *Geophys. Res. Lett.*, *32*, L08316, doi:10.1029/2004GL022310.

Matsubara, M., K. Obara, and K. Kasahara (2008), Three-dimensional P- and S-wave velocity structures beneath the Japan Islands obtained by high-density seismic stations by seismic tomography, *Tectonophysics*, *454*, 86–103, doi:10.1016/j.tecto.2008.04.016.

Matsubara, M., K. Obara, and K. Kasahara (2009), High-Vp/Vs zone accompanying non-volcanic tremors and slow-slip events beneath southwestern Japan, *Tectonophysics*, *472*(1-4), 6–17.

Mavko, G. M. (1980), Velocity and attenuation in partially molten rocks, *J. Geophys. Res.*, *85*, 5173–5189, doi:10.1029/JB085iB10p05173.

Melgar, D., and X. Pérez-Campos (2011), Imaging the Moho and subducted oceanic crust at the Isthmus of Tehuantepec, Mexico, from receiver functions, *Pure Appl. Geophys.*, *168*, 1449–1460.

Meyer, R. P., J. S. Steinhart, and G. P. Woollard (1961), Central plateau, Mexico, in *Explosion Studies of Continental Structure*, edited by J. S. Steihart and R. P. Meyer, 622, pp. 199–225, Carnegie Institution of Washington Publication.

Nadeau, R. M., and L. R. Johnson (1998), Seismological studies at Parkfield VI: Moment release rates and estimates of source parameters for small repeating earthquakes, *Bull. Seismol. Soc. Am.*, *88*(3), 790–814.

Nadeau, R. M., and T. V. McEvilly (1999), Fault slip rates at depth from recurrence intervals of repeating microearthquakes, *Science*, *285*, 718–721, doi: 10.1126/science.285.5428.718.

Nadeau, R. M., A. Michelini, R. A. Uhrhammer, D. Dolenc, and T. V. McEvilly (2004), Detailed kinematics, structure and recurrence of micro-seismicity in the SAFOD target region, *Geophys. Res. Lett.*, *31*, L12S08, doi:10.1029/2003GL019409.

Nelson, S. A., E. Gonzalez-Caver, and T. K. Kyser (1995), Constraints on the origin of alkaline and calc-alkaline magmas from the Tuxtla Volcanic Field, Veracruz, Mexico, *Contributions to Mineralogy and Petrology*, *122*(1), 191–211.

Noda, H., and N. Lapusta (2010), Three-dimensional earthquake sequence simulations with evolving temperature and pore pressure due to shear heating: Effect of heterogeneous hydraulic diffusivity, *J. Geophys. Res.*, *115*, B12314, doi:10.1029/2010JB007780.

Ordaz, M., and S. K. Singh (1992), Source spectra and spectral attenuation of seismic waves from Mexican earthquakes, and evidence of amplification in the hill zone of Mexico City, *Bull. Seismol. Soc. Am.*, *82*(1), 24–43.

Ottemöller, L., N. M. Shapiro, S. Krishna Singh, and J. F. Pacheco (2002), Lateral variation of Lg wave propagation in southern Mexico, *J. Geophys. Res.*, *107*, 2008, doi: 10.1029/2001JB000206.

Pardo, M., and G. Suárez (1995), Shape of the subducted Rivera and Cocos plates in southern Mexico: Seismic and tectonic implications, *J. Geophys. Res.*, *100*(B7), 12,357–12,373, doi:10.1029/95JB00919.

Park, J., C. R. Lindberg, and F. L. Vernon, III (1987), Multitaper spectral analysis of high-frequency seismograms, *J. Geophys. Res.*, *92*, 12,675–12,684, doi: 10.1029/JB092iB12p12675.

Payero, J. S., V. Kostoglodov, N. Shapiro, T. Mikumo, A. Iglesias, X. Pérez-Campos, and R. W. Clayton (2008), Nonvolcanic tremor observed in the Mexican subduction zone, *Geophys. Res. Lett.*, *35*, L07305, doi:10.1029/2007GL032877.

Peacock, S. M. (2003), Thermal structure and metamorphic evolution of subduction slabs, in *Inside the Subduction Factory*, *Geophys. Monogr. Ser.*, vol. 138, edited by J. Eiler, pp. 7–22, AGU, Washington, D. C.

Peng, Z., and Y. Ben-Zion (2005), Spatiotemporal variations of crustal anisotropy from similar events in aftershocks of the 1999 M7.4 İzmit and M7.1 Düzce, Turkey, earthquake sequences, *Geophys. J. Int.*, *160*, 1027–1043, doi:10.1111/j.1365-246X.2005.02569.x.

Peng, Z., J. E. Vidale, C. Marone, and A. Rubin (2005), Systematic variations in recurrence interval and moment of repeating aftershocks, *Geophys. Res. Lett.*, *32*, L15301, doi: 10.1029/2005GL022626.

Pérez-Campos, X., et al. (2008), Horizontal subduction and truncation of the Cocos Plate beneath central Mexico, *Geophys. Res. Lett.*, *35*, L18303, doi:10.1029/2008GL035127.

Rice, J. R. (1993), Spatio-temporal complexity of slip on a fault, *J. Geophys. Res.*, *98*, 9885–9907.

Rice, J. R., and A. L. Ruina (1983), Stability of steady frictional slipping, *Journal of applied mechanics*, *50*, 343.

Rietbrock, A. (2001), P wave attenuation structure in the fault area of the 1995 Kobe earthquake, *J. Geophys. Res.*, *106*(B3), 4141–4154.

Rogers, R. D., H. Kárason, and R. D. van der Hilst (2002), Epeirogenic uplift above a detached slab in northern Central America, *Geology*, *30*(11), 1031–1034.

Roth, E. G., D. A. Wiens, L. M. Dorman, J. Hildebran, and S. C. Webb (1999), Seismic attenuation tomography of the Tonga-Fiji region using phase pair methods, *J. Geophys. Res.*, *104*(B3), 4795–4809.

Rubin, A. M., and J.-P. Ampuero (2005), Earthquake nucleation on (aging) rate and state faults, *J. Geophys. Res.*, *110*, B11312, doi:10.1029/2005JB003686.

Ruina, A. (1983), Slip instability and state variable friction laws, *J. Geophys. Res.*, *88*(B12), 10,359–10,370.

Rychert, C. A., K. M. Fischer, G. A. Abers, T. Plank, E. Syracuse, J. M. Protti, V. Gonzalez, and W. Strauch (2008), Strong along-arc variations in attenuation in the mantle wedge beneath Costa Rica and Nicaragua, *Geochem. Geophys. Geosyst.*, *9*(10), Q10S10, doi:10.1029/2008GC002040.

Sagy, A., E. E. Brodsky, and G. J. Axen (2007), Evolution of fault-surface roughness with slip, *Geology*, *35*, 283, doi:10.1130/G23235A.1.

Sammis, C. G., and J. R. Rice (2001), Repeating earthquakes as low-stress-drop events at a border between locked and creeping fault patches, *Bull. Seismol. Soc. Am.*, *91*(3), 532–537, doi:10.1785/0120000075.

Schaff, D. P., and G. C. Beroza (2004), Coseismic and postseismic velocity changes measured by repeating earthquakes, *J. Geophys. Res.*, *109*, B10302, doi:10.1029/2004JB003011.

Schaff, D. P., G. C. Beroza, and B. E. Shaw (1998), Postseismic response of repeating aftershocks, *Geophys. Res. Lett.*, *25*(24), 4549–4552, doi:10.1029/1998GL900192.

Schurr, B., G. Asch, A. Rietbrock, R. Trumbull, and C. Haberland (2003), Complex patterns of fluid and melt transport in the central Andean subduction zone revealed by attenuation tomography, *Earth Planet. Sci. Lett.*, *215*, 105–119, doi:10.1016/S0012-821X(03)00441-2.

Schurr, B., A. Rietbrock, G. Asch, R. Kind, and O. Oncken (2006), Evidence for lithospheric detachment in the central Andes from local earthquake tomography, *Tectonophysics*, *415*(1-4), 203–223.

Schwartz, S. Y., and J. M. Rokosky (2007), Slow slip events and seismic tremor at circum-Pacific subduction zones, *Rev. Geophys.*, *45*, RG3004, doi:10.1029/2006RG000208.

Segall, P., and J. R. Rice (1995), Dilatancy, compaction, and slip instability of a fluid-infiltrated fault, *J. Geophys. Res.*, *100*(B11), 22,155–22,171.

Shapiro, N. M., M. Campillo, A. Paul, S. K. Singh, D. Jongmans, and F. J. Sánchez-Sesma (1997), Surface-wave propagation across the Mexican Volcanic Belt and the origin of the long-period seismic-wave amplification in the Valley of Mexico, *Geophys. J. Int.*, *128*, 151–166, doi:10.1111/j.1365-246X.1997.tb04076.x.

Shelly, D. R., G. C. Beroza, S. Ide, and S. Nakamula (2006), Low-frequency earthquakes in Shikoku, Japan, and their relationship to episodic tremor and slip, *Nature*, *442*(7099), 188–191.

Singh, S. K., J. F. Pacheco, D. Garcia, and A. Iglesias (2006), An estimate of shear-wave Q of the mantle wedge in Mexico, *Bull. Seismol. Soc. Am.*, *96*(1), 176–187.

Singh, S. K., A. Iglesias, D. Garcia, J. F. Pacheco, and M. Ordaz (2007), Q of Lg waves in the central Mexican Volcanic Belt, *Bull. Seismol. Soc. Am.*, *97*(4), 1259–1266.

Skinner, S. M., and R. W. Clayton (2011), An evaluation of proposed mechanisms of slab flattening in central Mexico, *Pure Appl. Geophys.*, *168*(8-9), 1461–1474.

Stachnik, J. C., G. A. Abers, and D. H. Christensen (2004), Seismic attenuation and mantle wedge temperatures in the Alaska subduction zone, *J. Geophys. Res.*, *109*, B10304, doi: 10.1029/2004JB003018.

Syracuse, E. M., G. A. Abers, K. Fischer, L. MacKenzie, C. Rychert, M. Protti, V. González, and W. Strauch (2008), Seismic tomography and earthquake locations in the Nicaraguan and Costa Rican upper mantle, *Geochem. Geophys. Geosyst.*, *9*(7), Q07S08, doi:10.1029/2008GC001963.

Thurber, C., and D. Eberhart-Phillips (1999), Local earthquake tomography with flexible gridding, *Computers & Geosciences*, *25*(7), 809–818.

Thurber, C. H. (1993), Local earthquake tomography: Velocities and Vp/Vs theory, in *Seismic Tomography: Theory and Practice*, edited by H. M. Iyer and K. Hirahara, pp. 563–583, CRC Press, Boca Raton, Fla.

Tsumura, N., S. Matsumoto, S. Horiuchi, and A. Hasegawa (2000), Three-dimensional attenuation structure beneath the northeastern Japan arc estimated from spectra of small earthquakes, *Tectonophysics*, *319*, 241–260, doi:10.1016/S0040-1951(99)00297-8.

Um, J., and C. Thurber (1987), A fast algorithm for two-point seismic ray tracing, *Bull. Seismol. Soc. Am.*, *77*(3), 972–986.

Valdes, C. M., W. D. Mooney, S. K. Singh, R. P. Meyer, C. Lomnitz, J. H. Luetgert, C. E.

Helsley, B. T. R. Lewis, and M. Mena (1986), Crustal structure of Oaxaca, Mexico, from seismic refraction measurements, *Bull. Seismol. Soc. Am.*, *76*(2), 547–563.

Verma, S. P. (2006), Extension-related origin of magmas from a garnet-bearing source in the Los Tuxtlas volcanic field, Mexico, *International Journal of Earth Sciences*, *95*(5), 871–901.

Vidale, J. E., W. L. Ellsworth, A. Cole, and C. Marone (1994), Variations in rupture process with recurrence interval in a repeated small earthquake, *Nature*, *368*, 624–626.

Wada, I., and K. Wang (2009), Common depth of slab-mantle decoupling: Reconciling diversity and uniformity of subduction zones, *Geochem. Geophys. Geosyst.*, *10*(10), Q10009.

Wagner, L. S., S. Beck, and G. Zandt (2005), Upper mantle structure in the south central Chilean subduction zone (30° to 36°S), *J. Geophys. Res.*, *110*(B9), B01308, doi: 10.1029/2004JB003238.

Yamamoto, J., L. Quintanar, R. B. Herrmann, and C. Fuentes (1997), Lateral variations of Lg coda Q in southern Mexico, *Pure Appl. Geophys.*, *149*(3), 575–599.

Zamora-Camacho, A., V. H. Espindola, J. F. Pacheco, J. M. Espindola, and M. L. Godinez (2010), Crustal thickness at the Tuxtla volcanic field (Veracruz, Mexico) from receiver functions, *Phys. Earth Planet. In.*, *182*, 1–9, doi:10.1016/j.pepi.2010.05.009.

Ziagos, J. P., D. D. Blackwell, and F. Mooser (1985), Heat flow in southern Mexico and the thermal effects of subduction, *J. Geophys. Res.*, *90*(B7), 5410–5420.